

INVESTIGATIONS ON VANADYL  
PHTHALOCYANINE AND ZINC OXIDE  
BASED HYBRID PHOTODIODES

Thesis

Submitted in partial fulfilment of the requirements for the degree of  
DOCTOR OF PHILOSOPHY

by

MANEPALLI R KIRAN



DEPARTMENT OF PHYSICS  
NATIONAL INSTITUTE OF TECHNOLOGY KARNATAKA,  
SURATHKAL, MANGALORE-575025  
JULY, 2018

## DECLARATION

*by the Ph.D. Research Scholar*

I hereby *declare* that Research Thesis entitled “Investigations on Vanadyl phthalocyanine and Zinc oxide Based Hybrid Photodiodes”, which is being submitted to the National Institute of Technology Karnataka, Surathkal in partial fulfilment of the requirements for the award of the Degree of Doctor of Philosophy in Physics is *bonafied report of the research work carried out by me*. The material contained in this Research Thesis has not been submitted to any University or Institution for the award of any degree.

MANEPALLI R KIRAN

Reg. 121193PH12F01

Department of Physics

Place: NITK, Surathkal

Date:

## CERTIFICATE

This is to *certify* that the Research Thesis entitled “Investigations on Vanadyl phthalocyanine and Zinc oxide Based Hybrid Photodiodes”, submitted by Manepalli R Kiran (Register Number: 121193PH12F01) as the record of the research work carried out by him, *is accepted as the Research Thesis submission* in partial fulfilment of the requirements for the award of degree of Doctor of Philosophy

Prof. M. N. Satyanarayan  
Research Guide

Prof. G. Umesh  
Research Co-Guide

Chairman- DRPC  
Date:

*Dedication*

*To my parents Subbarao & Dhanalakshmi*

*To my sister Chandrika Madhuri*

*To my wife Sriyyothi*

## **ACKNOWLEDGEMENTS**

Firstly, I would like to express my sincere thanks, appreciation and gratitude to my research supervisors Prof. M. N. Satyanarayan and Prof. G. Umesh. I am thankful for their continuous support, guidance, valuable expertise and inexhaustible patience during all the stages of my Ph.D., which have enabled me to complete my research and write up this thesis. I am grateful to Department of Physics, NITK Surathkal for provided me the Institute fellowship and contingency grant. I would also like to thank my Research Progress Assessment Committee members, Prof. S. M. Kulkarni and Dr. Ajith K. M. for their insightful comments and valuable suggestions. I extend my thanks to The Head, Faculty and Non-Teaching staff of the Department of Physics for their timely support.

I would like to acknowledge, Prof. A. Subrahmanyam, IITM Chennai, Dr. Udaya Bhat. K, NITK, Dr. Udaya Kumar. D, NITK for extending research facilities. I thank Prof. Subhasis Ghosh, JNU Delhi and Prof. Thomas Anthopoulos, KAUST, Thuwal and Dr. Kishore Sridharan, NITK, for sharing their expertise at various times. I also thank the editors and reviewers of my publications for their valuable assessment.

I am also deeply grateful for the companionship of my fellow researchers in the Institute. I would like to thank my seniors Dr. Vikas Shelar, Dr. Garudachar and Dr. Shashidara for their friendly advice at the beginning stage of my Ph.D. Many Thanks goes to Dr. Hidayath Ulla, Dr. Raghavendra Prasad J, Dr. Suresh Dara and Dr. B. Naveen Kumar Reddy for their selfless help in many extents. I also thank Mr. Krishnamanohara and Mr. Raghavendra M. A. N. S and Mr. M. Vijay and Mr. I. Ramesh Reddy for their help in simulation studies. My special thanks goes to my friend Mr. Chandra Sekhar. K, NIE Mysore, for his continuous help in AFM and SEM measurements.

Finally, I would like to acknowledge consistent support and encouragement from my parents, my sister and my loving wife, without their patience this work would not have possible.

---

## ABSTRACT

Organic-inorganic hybrid photodiodes have been of recent interest for optoelectronic applications. The motivation behind these investigations is to utilize the advantages of both organic and inorganic materials to achieve high-performance long lifetime devices. This thesis describes the fabrication and characterization of organic-inorganic hybrid diodes made using vanadyl phthalocyanine (VOPc; a p-type semiconductor) and zinc oxide (ZnO; a widely used n-type semiconductor). The optoelectronic properties of these materials were investigated in detail to understand the underlying operating mechanism for charge carrier generation and transport to enable fabrication of high-efficiency photodiodes. First, VOPc based single carrier hole-only devices fabricated by physical vapor deposition were characterized using current density-voltage (J-V) and Impedance spectroscopy (IS) measurements. The morphology dependence of VOPc films showed that the films deposited at lower rates (0.1 Å/s) exhibit improved electrical properties as they possess higher hole mobility ( $1.5 \times 10^{-7} \text{ cm}^2/\text{V-s}$ ) compared to films deposited at higher rates (5 Å/s). The dominant charge conduction mechanism in these films has been identified to follow the correlated barrier hopping (CBH) model. Following these studies, the sol-gel spin coated ZnO nanoparticulate thin films were investigated using J-V and IS measurements. The morphology dependent electrical properties showed that the ZnO films annealed at 350°C exhibit higher electron mobility ( $1.9 \times 10^{-5} \text{ cm}^2/\text{V-s}$ ) compared to the films annealed at lower temperatures. Finally, the hybrid photodiodes were fabricated using these two materials and characterized for optoelectronic properties. The devices involving ZnO films annealed at 350°C showed the maximum responsivity ( $R_{\text{ph}}$  in A/W) and the value was found to be 0.47 A/W, 0.13 A/W in forward and reverse bias conditions, respectively. Further, hybrid diodes fabricated using solution processed ZnO nanorods (ZNR) and VOPc showed higher responsivity compared to all other devices fabricated by us. A high responsivity of 16.28 A/W (forward bias) and 11.5 A/W (reverse bias) was achieved for ZNR films grown using precursor solution at 120°C. These values are several hundred times higher than the values obtained for devices made using ZnO nanoparticles thus indicating the superiority of ZNR based photodiodes.

Keywords: OPD, Vanadyl phthalocyanine, charge transport, mobility, photocurrent.

---

---

## CONTENTS

	Page No
<b>Chapter 1: Introduction</b>	01
1.1 Basics of Organic Semiconductors	01
1.2 Electronic Structure of Organic Molecular Semiconductors	03
1.3 Differences between Organic and Inorganic Semiconductors	04
1.4 Types of Organic Semiconductors	05
1.5 Organic Photodiode Design and Operation	06
1.6 Photocurrent generation Process Details	08
1.6.1 Light Absorption (Exciton Formation)	09
1.6.2 Exciton Migration	11
1.6.3 Exciton Dissociation	12
1.6.4 Charge Migration/Collection	14
1.7 Literature Review	15
1.7.1 Planar Phthalocyanines	16
1.7.2 Non-planar Phthalocyanines	19
1.7.3 Two layered Phthalocyanine Devices	21
1.8 Scope and Objective of the Thesis	24
1.8.1 Scope of the Thesis	24
1.8.2 Objectives of the Thesis	25
1.9 Organization of the Thesis	25
<b>Chapter 2: Materials and Experimental Techniques</b>	27
2.1 Materials Used in This Work	27
2.1.1 Transparent Electrode	27
2.1.2 Hole Injection Material	28
2.1.3 Hole Transport Material	28
2.1.4 Electron Transport Material	29
2.1.5 Metal Electrode	29

---

2.2	Materials Characterization	29
	2.2.1 X-Ray Diffraction (XRD)	29
	2.2.2 Atomic Force Microscopy (AFM)	30
	2.2.3 Scanning Electron Microscopy (SEM)	31
	2.2.4 UV- Vis Absorption and Transmission Spectra	32
2.3	Device Structures	33
	2.3.1 Hole Only Devices	34
	2.3.2 Electron Only Devices	34
	2.3.3 Organic-Inorganic p-n Junction	34
2.4	Device Fabrication	35
	2.4.1 Cleaning of the Patterned ITO Coated Glass Substrates	35
	2.4.2 Fabrication Procedure	36
	2.4.3 Fabrication of Hole Only Devices	36
	2.4.4 Fabrication of Electron Only Devices	37
	2.4.5 Fabrication of Hybrid P-N Junctions	38
2.5	Electrical Characterization	38
	2.5.1 Current Density– Voltage ( $J$ - $V$ ) Characteristics	39
	2.5.2 Capacitance –Voltage (C-V) Characteristics	40
	2.5.3 Impedance Spectroscopy (IS)	42
	2.5.4 Characterization of Devices under illumination	44
2.6	Conclusion	45
	<b>Chapter 3: Charge Transport Investigations in Hole Only Devices made using Vanadyl-Phthalocyanine Thin Films</b>	47
3.1	Introduction	47
3.2	Fabrication and Characterization of the Devices	48
	3.2.1 Fabrication of Hole Only Devices	48
	3.2.2 Structural and Morphological Properties	48
	3.2.3 J-V Characteristics	50
	3.2.4 Device Stability	54

---

3.2.5	C-V Characteristics	55
3.2.6	IS Measurements	56
3.2.7	Estimation of Charge Mobility Using Impedance Technique	61
3.2.8	Ac Conductivity	63
3.3	Conclusion	66
<b>Chapter 4:Electrical Charge Transport in Electron Only Devices made using Zinc Oxide (ZnO) Thin Films</b>		67
4.1	Introduction	67
4.2	Fabrication and Characterization of the Devices	68
4.2.1	Preparation Of ZnO Thin Films and Fabrication of Electron -Only Devices	68
4.2.2	Structural and Morphological Properties	69
4.2.3	Optical Transmission Spectra	70
4.2.4	J-V Characteristics	71
4.2.5	C-V Characteristics	75
4.2.6	IS Measurements	76
4.3	Conclusion	80
<b>Chapter 5:Optoelectronic Properties Of VOPc/ZnO Hybrid diodes</b>		81
5.1	Introduction	81
5.2	Fabrication and Characterization of the Devices	83
5.2.1	Fabrication of Hybrid p-n Junction Diode	83
5.2.2.	J-V Characteristics	83
5.2.3.	IS Measurements	86
5.3	Conclusion	88
<b>Chapter 6:Optoelectronic Properties of Hybrid Diodes Based on VOPc and ZnO Nanorod Thin Films</b>		89
6.1	Introduction	89
6.2	Fabrication and Characterization of the Devices	90

---

6.2.1	Preparation of ZNR Thin Films	90
6.2.2	Fabrication of Hybrid Photodiode	91
6.2.3	Structural and Morphological Properties.	91
6.2.4	Optical Transmission Spectra	93
6.2.5	J-V Characteristics	94
6.2.6.	IS Measurements	96
6.3	Conclusion	98
<b>Chapter 7:Summary and Conclusions</b>		101
7.1	Summary	101
7.2	Conclusions	103
7.3	Scope for Future Work	104
<b>Appendix</b>		107
<b>References</b>		109
<b>List of Publications</b>		135
<b>Brief Profile</b>		137

---

---

## LIST OF FIGURES

	<b>Page No.</b>	
<b>Figure 1.1</b>	Formation of energy levels (HOMO and LUMO) and the band gap of organic semiconductors	02
<b>Figure 1.2</b>	(a) Basic electronic structure of hydrogen atom, (b) Electronic structure of the polyatomic molecule (c) The simplified representation of the electronic structure of the organic solid and (d) Density of States profiles of the HOMO and LUMO” of organic molecules [Ishii et al. 1999], $E_F$ and $E_g$ represents the Fermi energy level and the energy band gap, respectively	03
<b>Figure 1.3</b>	Typical organic semiconductor materials; (a) small molecules and (b) polymer sub-molecular units (POSSs)	06
<b>Figure 1.4</b>	Schematic of OLED and OPD device structures indicating their separate functionality	07
<b>Figure 1.5</b>	Organic photodiode architectures (a) planar heterojunction, (b) bulk heterojunction and (c) Tandem multi-junction configurations	08
<b>Figure 1.6</b>	Schematic of a bilayer OPD illustrating the sequence of steps involved in the photocurrent generation process: <b>1</b> -light absorption, <b>2</b> -exciton migration, <b>3</b> -charge separation and <b>4</b> -charge migration	09
<b>Figure 1.7</b>	Schematic representations of (a) Frenkel, (b) Wannier-Mott and (c) charge transfer excitons	10
<b>Figure 1.8</b>	(a) Schematic illustration of the CT state formation and (b) Schematic of CT state separation process	13
<b>Figure 1.9</b>	Structure of metal phthalocyanine	15
<b>Figure 2.1</b>	HOMO and LUMO energy levels of all the semiconducting materials used for the fabrication of various devices for the works reported in this thesis.	28
<b>Figure 2.2</b>	Rigaku 600 MiniFlex diffractometer	30
<b>Figure 2.3</b>	Park Xe70 Atomic Force Microscopy	31

<b>Figure 2.4</b>	Zeiss Sigma Scanning Electron microscopy (FESEM)	32
<b>Figure 2.5</b>	Ocean Optics SD2000 Spectrophotometer	33
<b>Figure 2.6</b>	(a) Schematic device structure of the hole only devices and (b) electron-only devices	34
<b>Figure 2.7</b>	Typical device structure of the organic-inorganic hybrid p-n junction	35
<b>Figure 2.8</b>	VTE system equipped with turbo-molecular pump used for the fabrication of hole- only devices and inorganic-organic p-n junction devices.	37
<b>Figure 2.9</b>	Milman SPN 2000 Spin coating unit	38
<b>Figure 2.10</b>	Typical J-V characteristics of the electronic devices illustrating different regimes of conduction	39
<b>Figure 2.11</b>	(a) Typical Capacitance-voltage characteristics and (b) Mott-Schottky plots for a single layer device.	41
<b>Figure 2.12</b>	Plot of Im[Z] versus Re [Z], also known as Cole-Cole plot, and (b) the corresponding equivalent circuit to model the Cole-Cole plot.	43
<b>Figure 2.13</b>	(a) Impedance measurements setup (Agilent 4980A) and (b) schematic of the setup for the IS measurements.	44
<b>Figure 2.14</b>	Emission spectrum of the metal halide lamp (dark green) and the absorption spectra of the ZNR (red dots) and VOPc (blue dots) films.	44
<b>Figure 3.1</b>	(a) molecular structure of VOPc; the yellow, blue, brown, pink coloured spheres represents vanadium (V), Nitrogen (N), carbon (c), Hydrogen (H) atoms, respectively and (b) X-ray diffraction pattern of the VOPc thin films at different deposition rates	49
<b>Figure 3.2</b>	Surface morphology of VOPc films recorded at a scale of $2\mu\text{m}\times 2\mu\text{m}$ for the deposition rate of (a) $0.1\text{\AA}/\text{s}$ ; (b) $1\text{\AA}/\text{s}$ ; and (c) $5\text{\AA}/\text{s}$	50
<b>Figure 3.3</b>	(a) Schematic representation of the VOPc hole only	51

---

	device; <b>(b)</b> Energy level diagram; <b>(c)</b> Forward bias J-V characteristics of all the samples deposited at different deposition rates; <b>(d-f)</b> double logarithmic plots for the devices at 0.1 Å/s, 1 Å/s and 5 Å/s.	
<b>Figure 3.4</b>	Stability study of VOPc under ambient conditions	54
<b>Figure 3.5</b>	C-V characteristics of devices at different deposition rate	55
<b>Figure 3.6</b>	<b>(a-b)</b> Re [Z(f)]- $f$ measurements for the devices at 0.1 Å/s and 5 Å/s; <b>(c-d)</b> phase-frequency measurements for devices at 0.1 Å/s and 5 Å/s	57
<b>Figure 3.7</b>	<b>(a)</b> Cole-Cole plot for device deposited at 0.1 Å/s, <b>(b)</b> Cole-Cole plot for device deposited at 5 Å/s, <b>(c)</b> Imaginary impedance-frequency characteristics of device deposited at 0.1 Å/s, <b>(d)</b> Imaginary impedance-frequency characteristics of device deposited at 5 Å/s and <b>(e)</b> the equivalent circuit used for simulation	58
<b>Figure 3.8</b>	<b>(a)</b> Variation of resistance with applied bias in bulk and at the interface and <b>(b)</b> log-log plot of resistance variation with applied bias.	60
<b>Figure 3.9</b>	Simulation of frequency dependent Im Z for the different degree of dispersion Here, $\epsilon_r = 3.6$ for VOPc films, $\tau_{dc} = 1 \times 10^{-4} s$ , device area $A = 0.016 \text{ cm}^2$ and thickness $d = 100 \text{ nm}$	61
<b>Figure 3.10</b>	Field dependent hole mobility of VOPc film with different deposition rates	63
<b>Figure 3.11</b>	<b>(a)</b> Conductivity versus frequency plot at a given bias and <b>(b)</b> estimated hopping parameters by assuming CBH model	64
<b>Figure 4.1</b>	Schematic of the electron-only device	68
<b>Figure 4.2</b>	X-ray diffraction patterns of ZnO nanoparticulate thin films on a glass substrate at different annealing temperatures.	69
<b>Figure 4.3</b>	SEM images on 100 nm scale, of ZnO films on glass	70

---

	annealed at different temperatures	
<b>Figure 4.4</b>	<b>(a)</b> Optical transmittance spectra of ZnO at different annealing temperatures and <b>(b)</b> Tauc's plots to estimate the band gap of ZnO at different annealing temperatures	71
<b>Figure 4.5</b>	<b>(a)</b> Energy level representation of the electron only devices with ITO/ZnO/Al configuration. Here, $q\phi_I$ , $q\phi_{Al}$ and $q\chi_z$ represent the work functions of ITO, Al and the electron affinity of ZnO, respectively. $IP_{ZnO}$ is the ionization potential of ZnO; <b>(b)</b> J-V characteristics of the single layer devices at different annealing temperatures; <b>(c)</b> $\ln(I)$ -V characteristics of the single layer devices.	72
<b>Figure 4.6</b>	Mott-Schottky plots (C-V characteristics) for the electron only device made at different ZnO annealing temperatures	76
<b>Figure 4.7</b>	<b>(a)</b> Cole-Cole plots for ZnO annealed at 350°C as a function of bias voltage, <b>(b)</b> equivalent circuit to fit impedance plots <b>(c)</b> resistance-voltage measurements for devices at different annealing temperatures and <b>(d)</b> plots of parallel resistance voltage plots in logarithmic values to verify SCLC mechanism	77
<b>Figure 4.8</b>	<b>(a)</b> $Re [Z]-f$ characteristics of the ZnO annealed at 350°C, <b>(b)</b> $Im [Z]-f$ characteristics of the ZnO annealed at 350°C and <b>(c)</b> Poole-Frenkel mobilities for samples annealed at different temperatures and <b>(d)</b> computer simulations to find the numerical constant	79
<b>Figure 5.1</b>	Schematic of ZnO/VOPc hybrid diode	83
<b>Figure 5.2</b>	<b>(a)</b> Energy level representation of the VOPc/ZnO diode in the configuration: ITO/ZnO/VOPc/MoO <sub>3</sub> /Al; <b>(b)</b> J-V characteristics of a VOPc/ZnO p-n junction in dark conditions; <b>(c)</b> J-V characteristics of a VOPc/ZnO p-n junction in dark and illuminated conditions and <b>(d)</b> illustration of photocurrent generation mechanism in	84

---

	VOPc/ZnO p-n diode. The plots in different colours correspond to different annealing temperatures of the ZnO film indicated in the inset.	
<b>Figure 5.3</b>	<b>(a)</b> Cole-Cole plots for VOPc/ZnO interface (annealed at 350°C) p-n junction in dark and illuminated conditions for a given bias and <b>(b)</b> $\text{Re}[z] - f$ plots of a VOPc/ZnO (annealed at 350°C) p-n junction diode	87
<b>Figure 6.1</b>	<b>(a)</b> X-ray diffraction pattern of ZNR thin films grown at different temperatures; <b>(b)</b> SEM image of ZNR film grown at 60°C, <b>(c)</b> at 90°C and <b>(d)</b> at 120°C for about one hour (scale is 100nm); insets show the columnar structures that confirm the vertical growth perpendicular to the plane of ITO substrate	92
<b>Figure 6.2</b>	Optical transmittance spectra of ZNR films at different growth temperatures and the inset shows Tauc's plots to estimate band gap of ZNR films at the different growth temperature	93
<b>Figure 6.3</b>	<b>(a)</b> Schematic of the proposed hybrid p-n junction, <b>(b)</b> the energy level diagram of the proposed device structure, <b>(c)</b> J-V characteristics of devices under dark condition <b>(d-f)</b> J-V characteristics of the hybrid junctions under dark and illumination conditions at a given ZNR growth temperature	94
<b>Figure 6.4</b>	<b>(a)</b> J-V characteristics of the hybrid diode under dark for ZNR films grown at 120°C and <b>(b)</b> J-V characteristics of the hybrid diode in both dark and under illumination conditions. The plots in different colours represent the data for different bias voltages as indicated in the graphs.	97
<b>Figure 6.5</b>	Cole-Cole plots for the devices in both dark and illuminated conditions <b>(a)</b> at 0V, <b>(b)</b> at +5V and <b>(c)</b> -5V	97
<b>Figure A1</b>	<b>(a)</b> Conductivity-frequency characteristics of VOPc devices deposited at 0.1Å/s as a function of temperature	107

---

## LIST OF TABLES

	Page No.
<b>Table 2.1</b> Organic and inorganic material used in this thesis	28
<b>Table 3.1</b> Estimated parameters for from J-V characteristics	51
<b>Table 3.2</b> $\tau_{dc}$ to $\tau_r$ ration as obtained using ImZ method	60
<b>Table 4.1</b> Estimated parameters for the ZnO films annealed at different deposition rates	71
<b>Table 5.1</b> Estimated p-n junction parameters from J-V characteristics	84
<b>Table 6.1</b> Estimated p-n junction parameters from J-V characteristics	93
<b>Table 6.2</b> Estimated parameters from IS measurements employing equivalent circuit	96
<b>Table A1</b> Estimated ac conductivity parameters at 1 kHz	105

---

## NOMENCLATURE

$\theta$	Phase Shift
$\Delta E_F$	Quasi-Fermi Level Shift
$\phi_B$	Barrier Height
$L_D$	Exciton Diffusion Length
$\eta_{abs}$	Light Absorption Efficiency
$\eta_{coll}$	Charge Collection Efficiency
$\eta_{diss}$	Exciton Dissociation Efficiency
$\eta_{trans}$	Charge Transport Efficiency
$\mu$	Charge Carrier Mobility
$\mu_{IS}$	Charge Carrier Mobility Estimated From Impedance Measurements
$\mu_{SCLC}$	Charge Carrier Mobility In SCLC Regime
A	Area Of The Device
A*	Richardson Constant
ac	Alternating Current
AFM	Atomic Force Microscopy
Ag	Silver
Al	Aluminium
Al <sub>2</sub> O <sub>3</sub>	Aluminium Oxide
Alq <sub>3</sub>	Tris-(8-Hydroxyquinolino) Aluminium
AM	Air Mass
AO	Atomic Orbital
AS	Aqueous Solution Growth
Au	Gold
C <sub>60</sub>	Fullerene
CB	Conduction Band
C <sub>b</sub>	Bulk Capacitance
CET	Cascade Energy Transfer
C <sub>i</sub>	Interface Capacitance
ClAlPc	Chloroaluminium Phthalocyanine
ClInPc	Chloroindiumphthalocyanine

---

Co	Cobalt
Cr	Chromium
CS	Charge-Separated State
CT	Charge Transfer State
Cu	Copper
CuPc	Copper Phthalocyanine
D	Exciton Diffusivity
d	Thickness of active layer
dc	Direct Current
DT	Dexter Energy Transfer
E	Electric Field
e,q	Electron Charge
$E_g$	Optical Bandgap
ETM/ETL	Electron Transport Material
$f$	Frequency
FESEM	Field Emission Scanning Electron Microscopy
FT	Förster Energy Transfer
GDOS	Gaussian Density of States
h	Planks Constant
H <sub>2</sub> Pc	Metal Free Phthalocyanine
HOMO	Highest Occupied Molecular Orbitals
HOMO	Highest Occupied Molecular Orbital
HTM/HTL	Hole Transport Material
$I_0, I_{sat}$	Reverse Saturation Current
$Im[Z(f)]$	Imaginary Part Of Frequency Dependent Impedance
In	Indium
IP	Ionization Energy
ITO	Indium Tin Oxide
J-V	Current Density- Voltage
$k_B$	Boltzmann Constant
$L_A$	Optical Penetration Depth
LUMO	Lowest Unoccupied Molecular Orbital

---

M, $\alpha$	Dispersion Parameters
Mg	Magnesium
MgPc	Magnesium Phthalocyanine
MO	Molecular Orbital
MPc	Metal Phthalocyanine
MPCI	N,N'-Dimethyl-3,4:9,10-Perylenebis(Dicarboximide)
N( $E_f$ )	Density Of States at Fermi level
Ni	Nickel
NiPc	Nickel Phthalocyanine
N <sub>t</sub>	Total Concentration Of Traps
N <sub>v</sub>	Effective Density Of States At Valence Band Edge
OFET	Organic Field Effect Transistor
OLED	Organic Light Emitting Diode
OPD	Organic Photo Diode
OSC	Organic Solar Cell
p <sub>0</sub>	Concentration of Thermally Generated Holes
P <sub>0</sub>	Trap Density per Unit Energy range.
Pb	Lead
PbPc	Lead Phthalocyanine
Pc	Phthalocyanine
Pd	Palladium
PF	Poole-Frenkel
PL	Photoluminescence
POS	Polymeric Organic Semiconductor
PPP	Polyphenylene
PPV	Polyphenylenevinylene
PPy	Polypyrrole
PT	Polythiophene
Pt	Platinum
PVD	Physical Vapour Deposition
R	Minimum Hopping Length
R <sub>b</sub>	Bulk Resistance

---

Re[Z(f)]	Real Part Of Frequency Dependent Impedance
R <sub>i</sub>	Interface Resistance
RMS	Root Mean Square
R <sub>p</sub>	Bulk Resistance
R <sub>ph</sub>	Photocurrent Responsivity
RR	Rectification Ratio
R <sub>s</sub>	Series Resistance
s	Frequency Exponent In Conductivity-Frequency Plot
SCLC	Space Charge Limited Current
Si	Silicon
SnPcCl <sub>2</sub>	Tin chloride phthalocyanine
SSC	Sol-Gel Spin Coating
T	Absolute Temperature
TCNQ	Tetracyanoquinodimethane
TCO	Transparent Conducting Oxide
TiOPc	Titanyl Phthalocyanine
TPyP	5,10,15,20-Tetra(4-Pyridyl)21H,23H-Porphyrine
T <sub>t</sub>	Temperature Parameter For Exponential Trap Distribution
V	Applied Bias Voltage
VB	Valence Band
V <sub>bi</sub>	Built-In Voltage
V <sub>dc</sub>	Applied Dc Bias
VL	Vacuum Level
VOPc	Vanadyl Phthalocyanine
V <sub>t</sub>	Thermal Energy At Room Temperature
VTE	Vacuum Thermal Evaporation
W <sub>m</sub>	Binding Energy
XRD	X-Ray Diffraction
Z	Impedance
Zn	Zinc
ZnPc	Zinc Phthalocyanine
ZNR	Zinc Oxide Nanorod

---

$\beta$	Poole -Frenkel Field Lowering Coefficient.
$\delta$	Slope of The J-V Characteristics In Different Regimes
$\epsilon_0$	Absolute Permittivity
$\epsilon_r$	Dielectric Constant
$\sigma$	Conductivity
$\chi$	Electron Affinity
$\omega$	Angular Frequency
$\tau$	Relaxation Time

---

## CHAPTER 1

### INTRODUCTION

#### *Overview*

*Chapter 1 provides a brief overview of the field of organic electronic devices, the materials used for fabricating them and their operating characteristics. It begins with a description of the relevant properties of various organic semiconductors focussing on the role of interfaces and the charge transfer mechanism on the device performance. A brief description of the organic-inorganic hybrid heterojunctions and their utilization in the organic electronic devices is presented. This is followed by a brief discussion of the charge transport in disordered organic semiconductors. Next, the nature of materials used for respective devices and their characteristics is described. Lastly, the scope and objectives of the thesis are presented, followed by a summary of all the chapters in the thesis.*

#### **1.1 Basics of Organic semiconductors**

The term *organic semiconductor* is used to describe organic materials which possess the ability of electrical conduction due to electrons and/or holes depending on the materials chosen. *The basic constituent of all organic materials is carbon atoms and the most important aspect of organic semiconductors is the conjugation of the c-c bonds* [Stallinga 2009]. In these materials  $\pi$ -conjugation, involving alternating single and double bonds between neighbouring carbon atoms, plays an important role in the charge carrier transport processes.

The formation of  $\pi$ -bonds in a conjugated molecule corresponds to the splitting of the electron energy levels into the molecular orbitals (MOs). The energy of the MOs lower than the original atomic orbitals are known as bonding  $\pi$ -orbitals, while the MOs with higher energies are termed antibonding  $\pi^*$ - orbitals [Brütting 2005]. When the conjugation length increases, the number of  $p_z$  orbitals, which share

their electrons, increases. This leads to the splitting of individual energy levels resulting in quasi-continuous energy bands. The state possessing the highest energy amongst all the occupied orbitals is called the Highest Occupied Molecular Orbitals (HOMO) and is analogous to the top of the Valence Band (VB) in inorganic semiconductors [Hagan Klauk, 2006]. On the other hand, the state with the lowest energy amongst all the unoccupied molecular orbital is known as the Lowest Unoccupied Molecular Orbitals (LUMO) and is analogous to the bottom of the Conduction Band (CB) in inorganic semiconductors. The energy difference between the HOMO and the LUMO is taken to be the energy bandgap ( $E_g$ ). Generally, the bandgap of the organic molecules decreases if the number of atoms in the conjugated system is increased. Addition of electron-withdrawing (or electron-donating) functional groups lowers (or raises) the absolute energy value of the frontier molecular orbital [Hu et al. 2016].

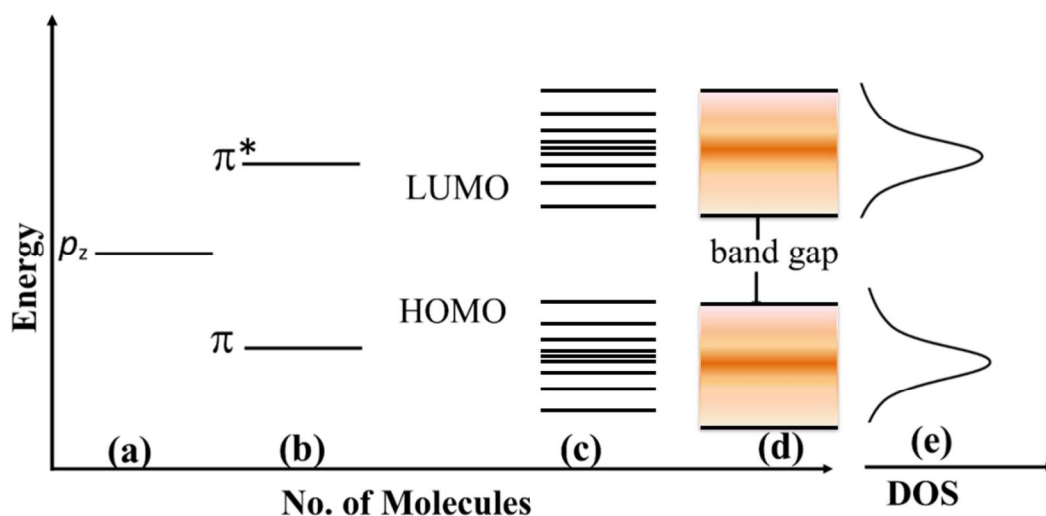


**Figure 1.1** Formation of energy levels (HOMO and LUMO) and the band gap of organic semiconductors.

The variation in conjugation lengths and interaction energies amongst the neighbouring molecules gives rise to locally varying polarization energies. This leads to the formation of broad Gaussian Density of States (GDOS) for bonding and anti-bonding orbitals of the molecules as shown in Figure 1.1. This aspect is also a consequence of the disordered nature of organic semiconductors.

In organic semiconductors, the charge transport occurs largely due to hopping of charge carriers between HOMO (or LUMO) levels, having comparable energies, of neighbouring molecules [Coropceanu et al. 2007]. Thus, organic semiconductors have several unique properties manifested by GDOS of the HOMO and LUMO levels.

## 1.2 Electronic Structure of Organic Molecular Semiconductors

The basic electronic structure of an isolated hydrogen atom is shown in Figure 1.2(a): the vertical axis shows electron energy (in eV). The various bound electron energy levels are shown. The higher energy levels converge to a continuum terminating in the vacuum level (VL), above which the electron is not bound to the nucleus. Figure 1.2(b) represents the electronic structure of a polyatomic molecule. Here, the potential well is formed by atomic nuclei together with the tightly bound electrons. The potential wells of all the nuclei get merged at higher energies to form a single broad well leading to delocalized MOs. On the contrary, AOs closer to the nuclei continue to be localized in the individual potential wells (core levels). The energy differences between the HOMO and LUMO to the VL are termed gas phase ionization energy (IP) and the electron affinity ( $\chi$ ) of the molecule, respectively.

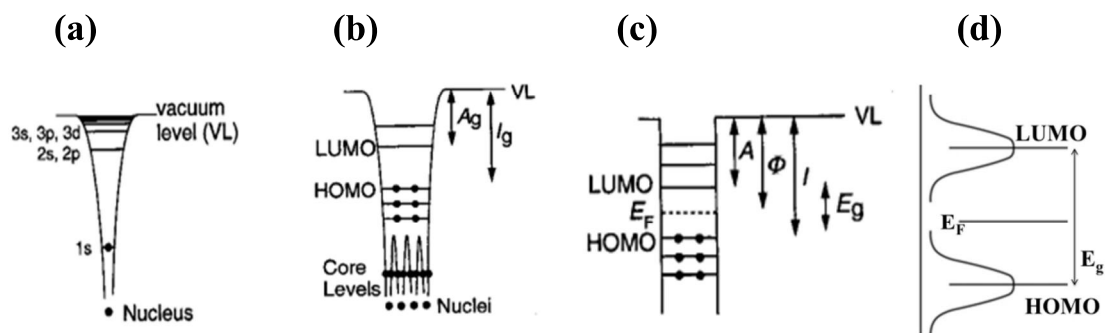


**Figure 1.2(a)** Basic electronic structure of hydrogen atom, **(b)** Electronic structure of the polyatomic molecule **(c)** The simplified representation of the electronic structure of the organic solid and **(d)** Density of States profiles of the HOMO and LUMO of organic molecules [Ishii et al. 1999],  $E_F$  and  $E_g$  represents the Fermi energy level and the energy band gap, respectively

When the molecules or polymer chains come together to form an organic solid, the electronic structure gets altered. The HOMO and LUMO bands are still

---

largely localized to each molecule in spite of the weak van der Waals interaction between the molecules. Since the energies of HOMO and LUMO bands of individual molecules are same, a simplified energy band structure may be adopted for the organic solid as shown in Figure 1.2(c). This model varies between materials, depending on the strength of interaction between the molecules of the solid and the arrangement in the crystal. In cases of weak interactions and/or energy disorder, the bands become broader and shape of the bands can be represented by Gaussian as shown in Figure 1.2(d).

### 1.3 Differences between Organic and Inorganic Semiconductors

In many aspects, organic semiconductors are very different from the widely used inorganic semiconductors. Inorganic semiconductors are characterized by strong covalent bonds or ionic and/or covalent bonds, resulting in electronic bands extending over the entire solid specimen. On the other hand, organic semiconductors are composed of organic molecules, held together by weak van der Waals interactions and have localized energy states [Köhler and Bäessler 2015]. However,  $\pi$ - $\pi$  stacking becomes important in solid organic semiconductors, particularly in samples having a crystalline structure (fully or partly) and high mobility. Moreover, the intramolecular coupling is much stronger compared to the inter-molecular van der Waals force. The mean free path of the charge carriers is of the order of intermolecular spacing.

The mechanisms for electrical conduction are another point of difference between the organic and inorganic semiconductors. The charge transport in the inorganic materials is band type, whereas it is mostly hopping type in organic semiconductors materials. The absence of the long-range order leads to the localization of electronic wave function and the formation of broad Gaussian Density of States (GDOS) for LUMO and HOMO bands. The charge carriers in the organic semiconductors hop between one molecule (site) to a neighboring site due to thermal or electric field activation [Ancumvan et al. 1995]. It is seen that the charge carrier mobility in organic materials is very small in comparison with that in inorganic materials [Rand et al. 2007, Gao and Zhao 2015]. It may be due to the fact that the exciton separation

---

is very difficult in organic semiconductors having low dielectric constants (~3) [Spanggaard and Krebs 2004].

The effective charge carrier mobility in the organic semiconductors is dependent on the temperature and the applied electric field as described by the Poole-Frenkel (PF) relation [Brütting 2005] given below

$$\mu(E, T) = \mu(0, T) \exp[\beta(T) \sqrt{E}] \quad (1.1)$$

where,  $\mu(0, T)$  and  $\beta(T)$  are temperature dependent quantities, known as Zero field mobility and field activation of the mobility, respectively. In these materials, the operating mechanism for transport of charge carriers is hopping between the two molecules having comparable energies for HOMO and LUMO.

#### 1.4 Types of Organic Semiconductors

Organic semiconductors are classified into mainly two groups on the basis of their molecular weight, namely (i)  $\pi$ -conjugated small molecules and (ii) polymeric organic semiconductors (POSs). The small molecule organic semiconductors are low molecular weight (< 900 Da) materials, while POSs have much higher molecular weight (> 900 Da) since they are long-chain organic molecules comprising of repeated sub-molecular units (at least 20 and typically several hundred units) [Thejo Kalyani and Dhoble 2015]. Devices fabricated using POSs have been studied extensively because of their compatibility with low-cost solution processing techniques (spin coating, dip coating, and inkjet printing) [Habas et al. 2010]. Solution process techniques are ideal for manufacturing flexible and large-scale electronic devices and systems. On the other hand, small molecules possess a well-defined chemical structure, but, many of them are insoluble in common organic solvents. Moreover, highly ordered films of small molecules can be obtained by using Physical Vapour Deposition technique (PVD). Generally, thin films of POSs have much higher disorder compared to films of small molecule organic semiconductors. Thus, the charge carrier mobilities in thin films of the small molecules are several orders higher than that of solution processed polymer devices. Figure 1.3(a, b) shows the molecular structure of some well-known organic semiconductor materials, both

small molecules and polymer types. Some of the small molecules, viz. copper phthalocyanine (CuPc), pentacene, fullerene (C<sub>60</sub>), rubrene and tris-(8-hydroxyquinolino) aluminum (Alq<sub>3</sub>) are shown in Figure 1.3(a). The long chain POSs, such as polyphenylene (PPP), polyphenylenevinylene (PPV), polythiophene (PT) and polypyrrole (PPy), are shown in Figure 1.3(b) [Stallinga 2009].

Electrical conductivity in organic solids was first discovered in doped polypyrrole in 1960. Several thousand small molecules and polymeric semiconductors have been synthesized so far, leading to the demonstration of several optoelectronic devices, including organic light emitting diodes (OLEDs), organic solar cells (OSCs), organic field effect transistors (OFETs) and, very recently, photodetectors [Arquer et al. 2017].

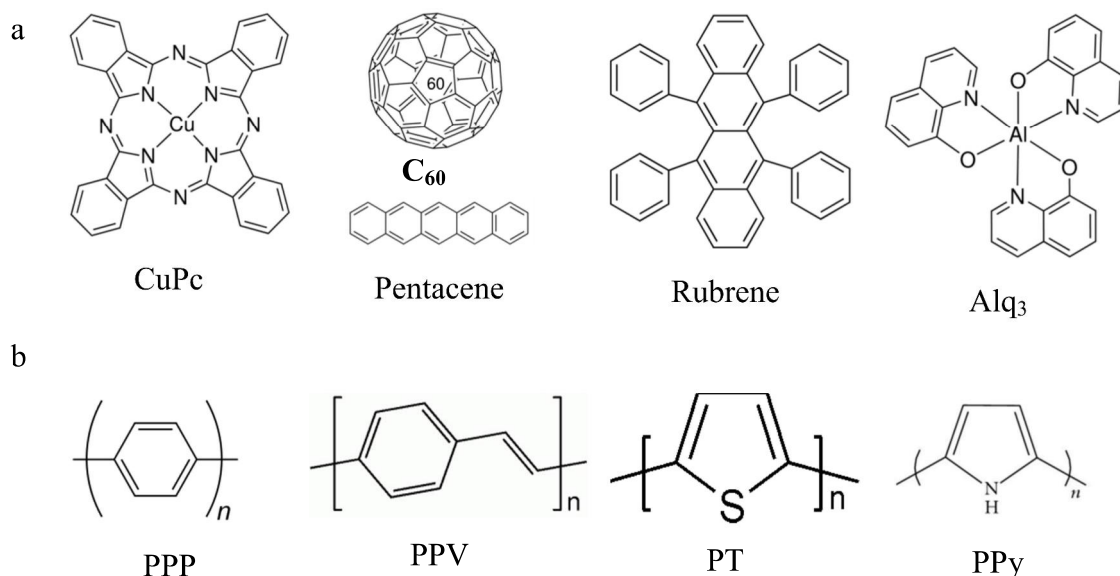


**Figure 1.3** Typical organic semiconductor materials; (a) small molecules and (b) polymer sub-molecular units (POSs) [Stallinga 2009].

## 1.5 ORGANIC PHOTODIODE DESIGN AND OPERATION

An Organic Photo Diode (OPD) is an optoelectronic device, comprising of thin layers of conductors and photoactive organic compounds, and generates current when illuminated by light. Almost all the OPDs have a planar structure, where the light absorbing layer is sandwiched between the two electrodes. One of the electrodes must

---

be a transparent conducting oxide such as indium tin oxide (ITO); thin transparent metal layer can also be used. The other electrode is very often a thin film of aluminum metal; calcium, magnesium, silver, gold and other metals are also used. Basically, the working principle of OPD is opposite to that of an OLED as illustrated in Figure 1.4.

In OLEDs, electrons are injected by the low work function cathode and, equivalently, holes are injected by the high work function anode. The injected electrons and the holes meet and recombine in the organic layers leading to the emission of the light. The reverse process happens in an OPD device, wherein, the light is absorbed by the active material (donor) an electron is excited from HOMO to LUMO forming an ‘exciton’ (coulombically bound electron-hole pair). The excitons are transported to the donor-acceptor junction where they get dissociated followed by charge collection by the electrodes [Spanggaard and Krebs 2004]. In order to achieve the exciton dissociation, an electric field is needed, which is provided by the asymmetrical ionization energy/work function of the electrodes. To facilitate better charge transport through the device and to improve the quality of electrical contacts, transparent charge transport layers are inserted between the active layer and the electrode contacts.

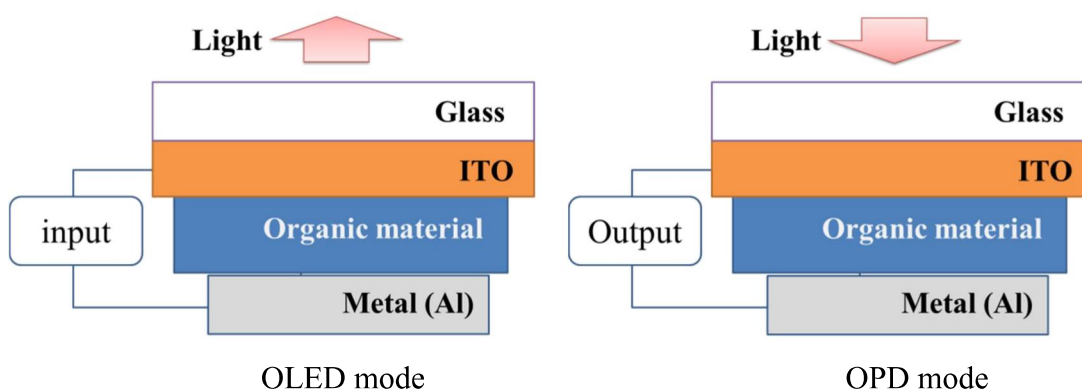


**Figure 1.4** Schematic of OLED and OPD device structures indicating their separate functionality.

The materials used in this work as active layers, transport layers and electrodes are discussed in detail in Chapter 2. The active layers in an OPD, typically, comprise of two organic semiconductors, an electron donor, and an electron acceptor. The donor

materials have a lower Ionization Potential (IP) and Electron Affinity ( $\chi$ ) (or equivalently, higher HOMO and LUMO levels) with respect to the acceptor materials. The energy offset at the donor-acceptor interface is necessary to enable efficient exciton dissociation and generation of free charge carriers in such materials. In the most basic configuration, the donor-acceptor junction consists of a bilayer structure, known as planar heterojunctions (Figure 1.5(a)). To optimize the photo-generation process, alternative device structures have been developed including bulk heterojunctions (Figure 1.5(b)) and tandem architectures (Figure 1.5(c)) [Wright and Uddin 2012].

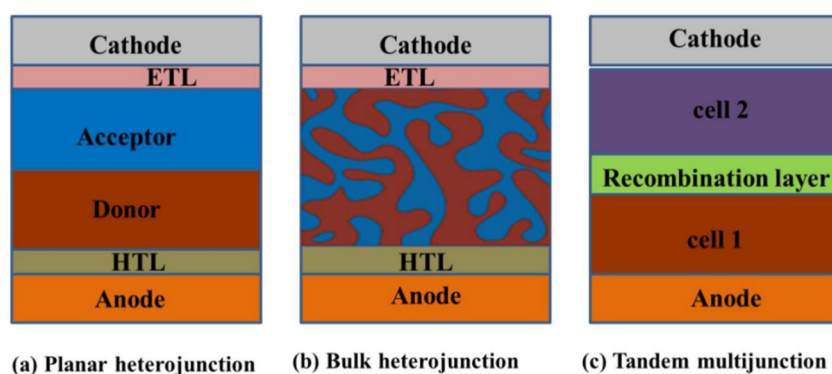


**Figure 1.5** Organic photodiode architectures (a) planar heterojunction, (b) bulk heterojunction and (c) Tandem multi-junction configurations.

## 1.6 PHOTOCURRENT GENERATION PROCESS DETAILS

In this section, the advantages and limitations of individual device architecture will be discussed by taking a closer look at the photocurrent generation processes. The photocurrent generation process in OPDs can be modeled as a sequence of four basic steps: (i) Light absorption (exciton formation), (ii) Exciton migration, (iii) charge separation (exciton dissociation) and (iv) charge migration (charge collection). The overall device efficiency is given by [Moliton and Nunzi 2006]

$$\eta_T = \eta_{abs} \times \eta_{diss} \times \eta_{trans} \times \eta_{coll} \quad (1.2)$$

where,  $\eta_{abs}$  is the light absorption efficiency,  $\eta_{diss}$  is the exciton dissociation efficiency,  $\eta_{trans}$  is the charge transport efficiency and the  $\eta_{coll}$  is the charge collection efficiency.

---

Absorption of a photon in an OPD leads to the formation of an exciton. In contrast to the inorganic semiconductor photodiodes, excitons need to diffuse to the donor-acceptor interface where the exciton dissociation occurs due to the energy offset between the frontier molecular orbitals [Kippelen and Brédas 2009]. This process of exciton dissociation involves transfer of electrons from the donor to the acceptor and/or transfer of hole from the acceptor to donor [Feron et al. 2012]. Finally, upon exciton dissociation, the separated charge carriers can be collected at the respective electrodes resulting in an electric current in the external circuit. The efficiency of each step is determined by the optoelectronic properties of the materials used in the OPD device. The photocurrent generation process is illustrated in Figure 1.6.

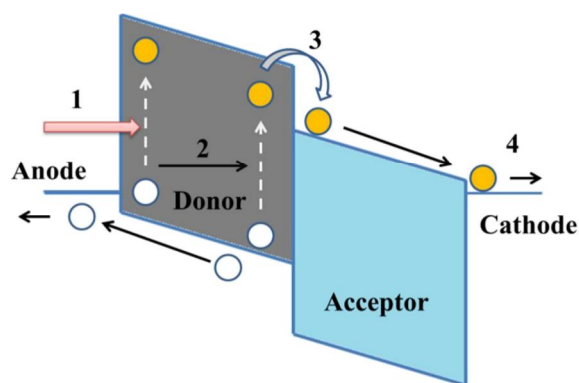


**Figure 1.6** Schematic of a bilayer OPD illustrating the sequence of steps involved in the photocurrent generation process: **1**-light absorption, **2**-exciton migration, **3**-charge separation and **4**-charge migration.

### 1.6.1 Light absorption (exciton formation)

As mentioned earlier, the first step in the photocurrent generation process in an OPD is the absorption of light in the active layer. In general, the optical absorption coefficient of organic molecules is higher compared to inorganic materials ( $>10^5 \text{ cm}^{-1}$  in the visible region). Therefore, a large amount of light can be absorbed by a small amount of organic material, usually as films of thickness on the order of hundreds of nanometers [Nath et al. 2017]. The optical absorption in organic semiconductors is determined by the optical bandgap which is related to the extension of  $\pi$ - $\pi^*$  transitions. The excitons generated by optical excitation are classified into mainly three types based on their binding energy and their exciton (Bohr) radius.

---

**Frenkel excitons:** Upon optical excitation in the materials of low dielectric constants ( $\sim 3$ ), the coulomb attraction between the photo-generated electrons and holes is quite strong. This results in an exciton radius less than 1 nm. These compact excitons are referred to as Frenkel-excitons and the binding energies of such excitons are on the order of 0.1-1eV. These excitons are highly localized to a single molecule and are usually formed in organic semiconductors [Kumar and Pankaj 2017].

**Wannier-Mott excitons:** For materials having high dielectric constant, the force of attraction between the electrons and holes reduces resulting in large exciton radius, which is greater than the lattice spacing  $\sim 10\text{nm}$ . These excitons are known as Wannier-Mott excitons. The attraction force between electrons and holes are influenced by neighboring atoms resulting in large exciton radius. The binding energy between the electrons and holes is in the order of 0.01eV. Such excitons are usually formed in inorganic crystalline semiconductors [Kumar and Pankaj 2017].

**Charge transfer excitons:** This is an intermediate case between Frenkel and Wannier-Mott excitons, wherein, electrons and holes are localized on two different adjacent molecules [Pope. M and Swenberg H. E 1999]. The exciton radius and binding energies are typically in the order of 1-10 nm and 0.01 to 0.1 eV, respectively.

The three types of excitons are schematically shown in Figure 1.7 (a, b and c)

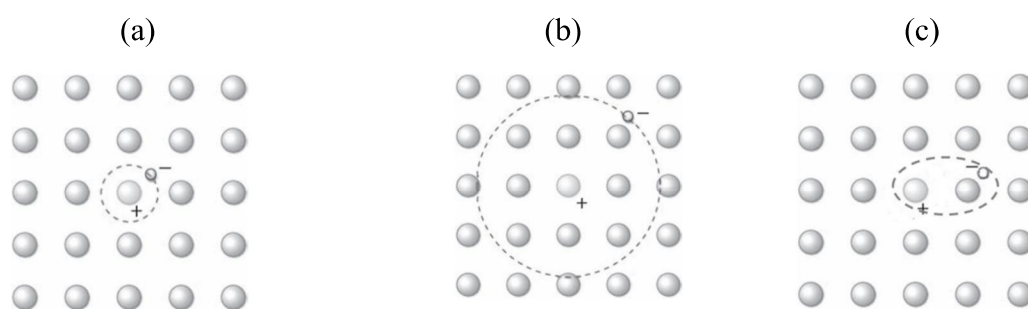


**Figure 1.7** Schematic representations of (a) Frenkel, (b) Wannier-Mott and (c) charge transfer excitons.

The optical absorption of organic semiconductors is limited to a narrow spectral region of the solar spectrum due to the lack of continuous band structure [Cao

---

and Xue 2014]. Consequently, a single donor-acceptor pair has a narrow absorption spectrum. This limitation leads to the development of tandem devices where the multiple films, with the complimentary absorption profiles, are incorporated in a single multi-junction device structure [Cao and Xue 2014] (Figure 1.5(c)). These tandem devices absorb a major portion of the solar spectrum.

### 1.6.2 Exciton migration

The exciton transport is voltage dependent and excitons rely on diffusion to reach the heterojunction. According to Random walk approximation (RWA), the exciton migration occurs via hopping between the neighbouring molecules. The efficiency of the exciton diffusion step is related to the diffusion length  $L_D = \sqrt{D\tau}$ , where  $D$  is the diffusivity and  $\tau$  is the exciton relaxation time. The diffusion length  $L_D$  is defined as the average distance an exciton diffuses before it decays to the ground state.

There are three types of energy transfers that are responsible for the exciton migration namely Cascade energy transfer, Förster transfer (mediated by Coulomb interactions) and Dexter transfer (electron exchange interactions) [Menke and Holmes 2014]. These mechanisms are described below:

- *Cascade energy transfer (CET)* involves the emission and subsequent absorption of a photon between two molecules. This mechanism is also referred to as re-absorption or radiative energy transfer. The energy transfer efficiency is related to the absorption coefficient  $\alpha$ , photoluminescence (PL) quantum yield,  $\eta_{PL}$ , and the Stokes shift. The length scales are relatively long and proportional to the optical penetration depth ( $L_A = 1/\alpha \approx 100$  nm). In the case of organic thin film absorbers, the radiative energy transfer is usually negligible due to very small absorption of remitted photons [Kumar and Pankaj 2017].
- *Förster energy transfer (FT)* is based on the dipole-dipole electromagnetic interaction between two molecules and occurs when the emission spectrum of the donor has a significant overlap with the absorption spectrum of the acceptor. The length scales are typically 1-5 nm. Usually, only singlet excitons

---

can be transferred via the Förster mechanism. However, a triplet exciton that is located at phosphorescent donor can also undergo FT [Mikhnenko et al. 2015].

- *Dexter energy transfer* (DT) involves the direct exchange of electrons (or holes) between two neighbouring molecules. This process requires the overlap of molecular orbitals. Thus, this energy transfer mechanism is limited to length scales of 0.1 nm to 1 nm [Kumar and Pankaj 2017].

The exciton lifetime and the diffusion length can be assessed by spectroscopic techniques (photoluminescence). The diffusion length of excitons in organic semiconductors (amorphous or polycrystalline) films is typically on the order of 10 nm [Spanggaard and Krebs 2004]. The lifetime of the singlet excitons (mediated by FT) is on the order of 1 ns, whereas triplet excitons (mediated by DT) possess much longer lifetime. The exciton diffusion can significantly limit the photocurrent generation in planar heterojunctions in many cases wherein the diffusion length  $L_D \ll L_A$ , the optical penetration depth.

OPDs, comprising of donor-acceptor bulk heterojunctions with interpenetrating networks, were developed to overcome the exciton diffusion length and lifetime-related issues. In such structures, the excitons are expected to be generated within the diffusion length from the donor-acceptor interface (Figure 1.5(b)). This requires precise control over the preparation of the bulk mixtures (phase segregation), followed by controlled deposition conditions and/or post-annealing treatments [Kovacik et al. 2013]. The exciton diffusion efficiency can also be improved by increasing the crystallinity of the organic semiconductor film itself. Incorporating an exciton blocking layers was another approach adopted to improve diffusion by reduction of exciton quenching at the electrodes [Yapi et al. 2010].

### 1.6.3 Exciton dissociation

The exciton dissociation is often described by a simple model where the HOMO/LUMO energy level offset of the donor and acceptor molecules acts as the main driving force for charge separation. Many reports have demonstrated that the dissociation of exciton at the donor-acceptor interface takes place via an intermediate

charge transfer state (CT) [Tress 2014, Wang et al. 2017]. The CT state occurs if the donor (having an electron) is located adjacent to an acceptor (having a hole). The distance between the electron and hole in this CT state is referred as thermalization length. The formation, recombination and dissociation of these excitons play a crucial role in the operation of OPDs. The exact mechanisms enabling efficient exciton dissociation via CT state are still under debate. Extensive reviews on charge transfer processes are available in the literature [Bakulin et al. 2013, Ostroverkhova 2016].

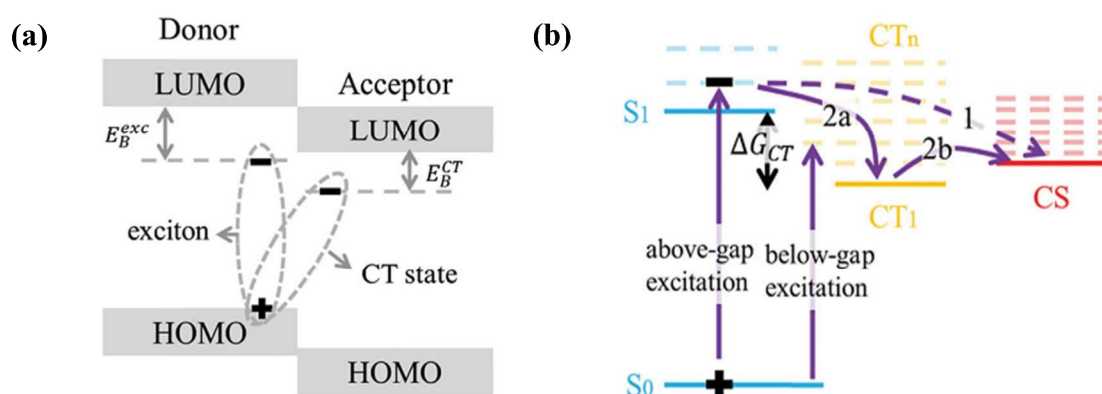


**Figure 1.8(a)** Schematic illustration of the CT state formation and **1.8(b)** Schematic of CT state separation process [Gao and Inganäs 2014].

The schematic representation of the formation of the CT state is shown in Figure 1.8(a), which includes the exciton and CT state binding energies ( $E_B^{exc}$  and  $E_B^{CT}$ ). For simplicity, the binding energies are shown relative to the LUMOs of donor and acceptor materials. Figure 1.8(b) illustrates the CT separation process. In general, the CT state is generated with the thermal energy ( $\Delta G_{CT}$ ), which is greater than the exciton binding energy. This state is referred to as hot CT state and this state can be dissociated by two processes. The hot CT state can either directly dissociate into the charge separated (CS) states, thereby generating free carriers (process **1**), or it can thermally relax initially to the lowest lying CT state ( $CT_1$ , process **2a**), and, then dissociate into the CS state (process **2b**) [Gao and Inganäs 2014]. However, the actual role of these two processes in the dissociation of CT state is still not well understood.

Onsager-Braun theory [Braun 1984] is often used to describe the CT state dissociation. This theory relates the charge separation rate to macroscopic parameters

---

such as dielectric constant, internal electrical field and charge carrier mobility of organic semiconductor. The CT state separation efficiency depends on the thermalization length. However, this model does not account for other factors which may influence the CT separation efficiency, such as, energetic disorder, excess kinetic energy, charge delocalization and entropy contribution to the free energy [Braun 1984]. Since the efficiency of OPD is related to the charge separation efficiency of the CT state (in turn related to open circuit voltage), it is important to minimize the energy losses related to the charge transfer without compromising the CT efficiency.

#### **1.6.4 Charge migration/Collection**

The final step in the photocurrent generation process in OPD is the collection of charge carriers at the respective electrodes. Once the charges are separated at the donor-acceptor interface, they should migrate to the respective electrodes. This charge transport through the organic semiconductor layers is governed by both drift and diffusion. The charge carrier mobility and carrier lifetime are the key parameters that determine the efficiency of the charge transport.

Most of the phthalocyanines possess polycrystalline nature [Dent et al. 1934, Collins and Mohammed 1986, 1996, Dhanya and Menon 2012, Braik et al. 2015]. The mobility of charge carriers is high in the crystalline organic semiconductors due to the reduction of grain boundaries. The charge transport in such materials can be described fairly well by a band like transport similar to that in inorganic crystalline materials. Conversely, due to the molecular disorder and charge localization, the charge carriers in the organic semiconductors are largely transported by hopping mechanism. This leads to the low charge carrier mobility in organic semiconductors [Rand et al. 2007]. Many models have been proposed in the literature to account for the dependence of charge mobility on temperature, electric field and charge carrier density. However, the protocol for using the accurate method is not has been standardized [Blakesley et al. 2014].

Further, traps related to structural and morphological defects, impurities and grain boundaries greatly influence the carrier lifetime and, hence, mobility. In bulk heterojunctions, there is also the possibility of forming isolated donor and acceptor

---

phases during the fine intermixing of the organic semiconductors [Serbenta et al. 2016]. This leads to the low charge mobility and carrier lifetime in the bulk heterojunctions due to trapping of charge carriers in the isolated phases. Furthermore, charge transport layers must be necessarily used to form ohmic contacts with the electrodes to avoid the barrier height related issues and to avoid, at the same time, charge recombination at both the electrodes (top and bottom). These transport layers are usually transparent to visible light and ensure higher charge transport for electrons or holes depending on the material used [Yapi et al. 2010].

## 1.7 LITERATURE REVIEW

The metal-free phthalocyanine (Pc) was first synthesized in 1907 by Braun and Tcherniac [Braun and Tcherniac 1907]. In 1927, Diesbach and Weid were the first to report the synthesis of Copper phthalocyanine (CuPc) along with the copper naphthalocyanine and copper octamethylphthalocyanine [Diesbachde and von der Weid, 1927]. These were the very first metal substituted phthalocyanines synthesized. The term '*phthalocyanine*' was first used by Linstead (1933) to describe a class of organic dyes whose colours ranged from reddish blue to yellow-green. The name phthalocyanine originated from the Greek terms '*naphtha*' for rock oil and '*cyanide*' for dark blue. Later many other metal phthalocyanines were synthesized and a comprehensive study of their chemical properties was initiated by Linstead and co-workers in 1934 [Byrne et al. 1934, Dent and Linstead 1934, Dent et al. 1934, Linstead 1934, Linstead and Lowe 1934a, 1934b]. As a part of these investigations, Dent and Linstead first revealed the structure of planar Pcs [Dent and Linstead 1934]. It consists of four isoindole units linked by azo nitrogen atoms. In simple metal phthalocyanines (MPcs), the metal atoms are coordinated with four nitrogen atoms of the isoindole moieties [Dent and Linstead 1934]. The molecular structure of a typical metal phthalocyanine is shown in Figure 1.9.

Eley was the first to observe the semiconducting behaviour of Pc and CuPc when placed in between two platinum electrodes [Eley 1948]. Heilmeyer and Warfield found that the single crystals of metal-free Pcs exhibit ohmic behaviour under applied electric fields less than  $10^4$  V/cm and square law dependence on voltage (SCLC) for

---

higher fields [Heilmeyer and Warfield 1963]. Delacote et al. investigated the electron injection property of the CuPc thin films sandwiched between gold electrodes. They identified three different types of current density variation with applied voltage, namely, ohmic (at low voltages), exponential (at intermediate voltages) and square law dependence at high voltages [Delacote et al. 1964].

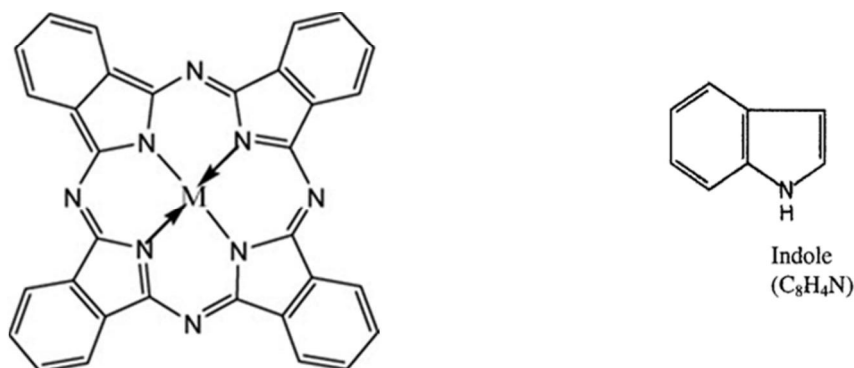


**Figure 1.9** Structure of metal phthalocyanine [Sutarlie and Yang 2008].

### 1.7.1 Planar phthalocyanines

Sussman identified SCLC conduction in CuPc thin films and also studied the effects of using nitrogen, hydrogen and oxygen gas, as background gas while depositing thin films, on the conductivity, trap density and carrier mobility of the films [Sussman 1967a, 1967b]. This effectively laid the foundations for the subsequent works on phthalocyanines as gas detectors. Barkhalov and Vidadi investigated the Schottky barrier of CuPc devices with Al/CuPc/Ag structure. They inferred that the Schottky diode with asymmetrical current characteristics can be obtained by proper selections of electrodes with one blocking and one ohmic contact [Barkhalov and Vidadi 1977]. The Schottky diodes and the photovoltaic properties of different MPcs (Cu, Pb, Zn, Ni and Co) were studied during the 1970s in the metal-insulator-metal structured devices with different metal electrodes (Pd, Pt, Au, Cu, In, Al, Mg). These investigations indicated that light was absorbed only in the space charge layer of the Pc near the interfaces leading to charge carrier generation [Fan and Faulkner 1978b, 1978a, Loutfy and Sharp 1979, Yamamoto et al. 1981].

---

Gould investigated the electrical properties of CuPc thin films sandwiched between the gold (Au) electrodes for different thickness of the active layer. He observed ohmic conduction at low voltages and SCLC, controlled by an exponential trap distribution above the valence band (VB), for higher voltages [Gould 1985]. He also investigated the electrical properties of the CuPc thin films fabricated by PVD as a function of vacuum chamber pressure to deposition rate ratio (P/R). The charge carrier mobility of the films was observed to decrease as the P/R ratio was increased. This was ascribed to the scattering and trapping effects of ambient gas molecules embedded in the film at higher values of pressure, indicating that these parameters are particularly sensitive to deposition conditions [Gould 1986]. Hassan and Gould studied CuPc films sandwiched between different metal electrodes in the device configurations In/CuPc/In, Au/CuPc/Au, Au/CuPc/Pb and Au/CuPc/Al. These studies revealed that symmetrical current density-voltage (J-V) characteristics occur if both the electrodes are of the same metal and, the J-V plots are asymmetrical (very less current in reverse bias) if the metal used for the cathode is different from that used for the anode. These studies also indicated that the conduction mechanism in these devices is ohmic and SCLC type at lower bias voltages and is Poole-Frenkel (PF) type at much higher voltages. They also identified similar behaviour when the devices were exposed to oxygen for longer periods at room temperature [Hassan and Gould 1989, Gould and Hassan 1990, Hassan and Gould 1990].

Fan and Faulkner compared the electrical properties of metal-free phthalocyanine (H<sub>2</sub>Pc) and zinc phthalocyanine (ZnPc) in the Metal/Pc/Au configuration. Al and In were used as injecting metal electrode. The devices showed non-ideal J-V characteristics (ideality factor >1) with Indium as the injecting electrode. This was ascribed to (i) lowering of the potential barrier by the image force, (ii) the presence of an insulating interface layer (iii) charges trapped in the interface states and (iv) minority charge carrier currents. On the other hand, it was reported that the devices with aluminum (Al) cathode are several orders less conductive than those using indium (In) cathode. These devices also showed SCLC conduction at very low voltages instead of ohmic nature. This was ascribed to the oxide layer (Al<sub>2</sub>O<sub>3</sub>) formation in the Al/Pc interfaces [Fan and Faulkner 1978b, 1978a]. Collins and

---

Mohammed studied the dark conductivity of ZnPc as a function of material purity, crystalline phase transformation, temperature, and also the influence of various background gases such as O<sub>2</sub>, N<sub>2</sub>, Argon, NH<sub>3</sub>, and the NH<sub>3</sub>-Air mixture used during film deposition. The decrease in electrical conductivity with NH<sub>3</sub> exposure was more compared to other gases and is found to depend on the material purity. This study indicated that the ZnPc can also be used as a gas sensor [Collins and Mohammed 1986]. Saleh et al. investigated the ac electrical properties of thermally evaporated ZnPc films using gold electrodes. The ac measurements, as a function of frequency and temperature, reveal that hopping conduction is dominant at low temperatures (and at high frequencies) and band-type conduction at high temperatures ( and at lower frequencies) [Saleh et al. 1993]. The electrical and photovoltaic properties of Al/ZnPc/ITO and Al/iodine doped ZnPc/ITO structures were investigated by Sharma et al. and they observed an enhancement in p-type conductivity with the iodine doping [Sharma et al. 1996]. Kerp and Faassen carried out a study on the effect of oxygen doping on the photovoltaic properties of solar cells made of ZnPc. They observed that the post-deposition annealing has a remarkable influence on the activation energy and electrical conductivity of phthalocyanine thin films [Kerp and Van Faassen 2000].

Gould and Blyth studied the electrical conductivity of Nickel phthalocyanine (NiPc) thin films sandwiched between Au electrodes. They observed ohmic conductivity at low voltages with hole concentration in the order of  $10^{15}$  to  $10^{17}$  m<sup>-3</sup> and SCLC conductivity controlled by the exponential distribution of traps (order of  $10^{22}$  m<sup>-3</sup>) for higher voltages [Gould and Blyth 1990]. The effect of annealing on the electrical conductivity in NiPc films was investigated by Hassan and Gould. Both films, as prepared and annealed, showed ohmic conduction and SCLC. While the as-prepared film showed discrete trap levels, the annealed NiPc films possessed exponential trap level distribution [Hassan and Gould 1992]. Schottky barrier sandwich structures were fabricated in Al/NiPc/Ag and Al/Tetracyanoquinodimethane (TCNQ)/NiPc/Ag configurations. The devices show a rather small photovoltaic response in a vacuum environment, while the photovoltaic response is observed to be much better after exposure to air. The use of TCNQ as a hole injection layer was shown to enhance the dark conductivity short-circuit current [McHale et al. 1996,

---

Hooper et al. 1997]. Riad [Riad 1999] fabricated Schottky barrier devices (Al/NiPc/Au) to investigate charge transport under oxygen ambient and annealed conditions. Under forward bias, two distinct regions of SCLC were observed. At lower fields, discrete trap levels were seen to dominate, whereas, exponential trap distributions dominate at higher fields. The oxygen exposure (for 10 days) resulted in an increase in the rectification ratio of the devices. Further, annealing reduces the conductivity of NiPc due to desorption of oxygen [Riad 1999]. Anthopoulos and Shafai performed dc electrical measurements as a function of NiPc film thickness (Au/NiPc/Au) and showed that the electron conduction is initially ohmic and changes over to SCLC as the applied bias is increased [Anthopoulos and Shafai 2000]. They also described the electrical properties of Au/NiPc/In, Au/NiPc/Au, Au/ $\alpha$ -NiPc/Au, Au/NiPc/Al and Au/NiPc/Pb structures in a series of papers. It is seen that the charge carrier concentration decreases for heat treated samples due to the removal of oxygen molecules during the thermal annealing process. Further, the rectifying nature of the junction in the devices was found to improve upon prolonged exposure to dry air. These results were interpreted in terms of O<sub>2</sub> adsorption close to NiPc/Al, NiPc/In and NiPc/Pb interfaces. It was also observed that the Au/NiPc/Pb devices generate substantial photo-induced voltage and photocurrent. The power conversion efficiency of the solar cells was found to increase by a factor of 2.75 upon exposure to dry air due to p-induced doping [Anthopoulos and Shafai 2000, 2003a, 2003b]. The frequency and temperature dependent studies of ac conductivity revealed that hopping-type mechanism dominates at lower temperatures and free-band conduction dominated in the high-temperature region [Anthopoulos and Shafai 2003a].

The electrical properties of other devices having planar phthalocyanine (including Co, Pd, Pt phthalocyanines) were reported recently. The studies indicated the occurrence of ohmic, SCLC and PF conduction mechanisms in single layer devices [Rajesh and Menon 2005, Jarosz 2010, Braik et al. 2015].

### **1.7.2 Non-planar phthalocyanines**

Waclawek reported the electrical conductivity of lead phthalocyanine (PbPc) thin films. The electrical conductivity was found to be raised by 7 to 9 orders of

---

magnitude with iodine doping [Wac lawek and Zabkowska-Waclawek 1987]. Shafai and Gould investigated the dc electrical conductivity of PbPc devices as a function of the thickness of the active layer. At low voltages, ohms law was seen to be valid and the thermally activated hole concentration was  $10^{16}\text{m}^{-3}$ . Above a threshold voltage, a power law dependence of current density on applied voltage was observed indicating SCLC with an exponential distribution of traps [Shafai and Gould 1990]. They also investigated the current density-voltage characteristics for Al/PbPc/Au sandwich devices for both the polarities. Under forward bias, two distinct types of power-law dependence of current density were observed. One part of the plot had a slope of  $\sim 4$  implying SCLC, controlled by the exponential distribution of traps, and a second region had a slope of  $\sim 2$ , implying SCLC with discrete trap levels. Under reverse bias, a transition from an electrode-limited behavior to the bulk-limited regime was observed indicating a change over from the Schottky effect to Poole-Frenkel effect [Shafai and Gould 1992b, 1992a].

Ahmad and Collins investigated the electrical properties of triclinic PbPc thin films in Au/PbPc/Al and Al/PbPc/Au configuration. The results emphasized the role of interfacial oxide layer formation in determining the electrical behaviour of the PbPc based devices [Ahmad and Collins 1991]. Additionally, the conductivity of PbPc thin films is found to be critically dependent upon the presence of oxygen. Prolonged exposure to oxygen enhances conductivity and decreases the conduction activation energies [Ahmad and Collins 1992]. The electrical characteristics of monoclinic PbPc thin films have been studied as a function of substrate temperature during PVD under vacuum and after exposure to both oxygen and air. Oxygen diffusion into the bulk of the PbPc layer implies that the PbPc device can no longer be used as an oxygen sensor [Abass et al. 1993]. AC measurements indicated that capacitance and dissipation factors of the PbPc sandwich devices, with gold electrodes, decrease with increasing frequency and increase with increasing temperature. The hopping conduction was observed to be dominant at low temperatures and high frequencies, whereas band conduction was dominant at high temperatures and low frequencies [Azim-Araghi et al. 1996].

---

Sharma[1995a] observed the dominance of hopping conduction at low temperatures (higher frequencies) and free carrier conduction at higher temperatures (lower frequencies) for chloroaluminum phthalocyanine (ClAlPc) thin film sandwiched between two Au electrodes. He also studied the electrical and optoelectronic properties of ClAlPc based diodes with different electrodes. The devices Al/ClAlPc/ITO and In/ClAlPc/ITO showed rectification, while Au/ClAlPc/Au devices did not show any rectification. The devices exhibited ohmic nature at lower voltages, whereas, SCLC controlled by a discrete trapping level above the valence band edge, was observed at higher voltages [Sharma 1995b]. Araghi also observed similar characteristics for ClAlPc sandwiched devices. For such devices, the hopping model is dominant at low temperatures and high frequencies, whereas the band theory is seen to apply at high temperatures and low frequencies [Azim-Araghi et al. 1997].

Several studies on the dc and ac electrical properties of other non-planar phthalocyanines were also reported to verify their electrical conduction mechanism [Signerski and Kościelska 2005, Song et al. 2008, Kalia et al. 2016, Can Ömür et al. 2017].

### **1.7.3 Two layered Phthalocyanine Devices**

Tang fabricated the first two-layer organic photovoltaic cell using CuPc and perylenetetracarboxylic derivatives. A power conversion efficiency of about 1% was achieved under simulated-air-mass-2 (AM2) illumination. The novel feature of this device is that the charge generation efficiency is independent of the bias voltage, resulting in a fill factor value as high as 0.65 [Tang 1986]. Antohe described the electrical and photovoltaic properties of two-layer solar cell made with CuPc and 5,10,15,20-tetra(4-pyridyl)21H,23H-porphyrine (TPyP). The p-n junction cell with TPyP exhibits optical absorption over a wider part of the solar spectrum than a Schottky cell using CuPc or TPyP layer. They suggested that the interface between the two organic materials is more crucial in determining the photovoltaic properties of the cell rather than the electrode/organic contact [Antohe et al. 1996].

---

The Chloroindiumphthalocyanine (ClInPc)/ C60 heterojunction device was fabricated by Xia *et al.* They showed that the large photo-response is mainly due to the photo-induced charge transfer between the C60 and the ClInPc [Xia et al. 1995]. Tsuzuki *et al.* fabricated p-n heterojunction devices consisting of thin films of Titanium phthalocyanine (TiOPc) and N,N'-dimethyl-3,4:9,10-perylene bis(dicarboximide) (MPCI), sandwiched between ITO and Au. These devices showed a response to light over the entire visible region from 400 to 900 nm. The device having the structure ITO/MPCI/TiOPc/Au (0.7% PCE) was seen to be superior to that with the structure ITO/TiOPc/MPCI/Au (0.35%) in terms of conversion efficiency [Tsuzuki et al. 1996]. They also studied the effect of morphology on the photovoltaic properties of TiOPc in the configuration Au/MCPI/TiOPc/ITO. Solar Cells fabricated using crystalline  $\alpha$ -TiOPc film exhibited higher efficiencies than devices using amorphous TiOPc film [Tsuzuki et al. 1996]. The photovoltaic properties of solar cells in the configuration Al/C60/TiOPc/ITO were studied by Yonehara and Pac revealing relatively high energy conversion efficiencies at 720 nm due to the formation of a p-n junction between C60 and TiOPc. It was found that the insertion of a thin Silica (SiO<sub>2</sub>) insulator layer in-between TiOPc/ Cr.Au (instead of Al) significantly enhanced the device efficiency [Yonehara and Pac 1996].

Over the past few decades, organic and inorganic heterojunctions have drawn much interest for application as photodiodes (and/or photovoltaics). The two-layer devices in combination with Si substrate (n-type or p-type) have been studied by many researchers for different phthalocyanines. The heterojunctions such as MgPc/n-Si, ZnPc/p-Si, H<sub>2</sub>Pc/n-Si, NiPc/n-Si, VOPc/n-Si, CuPc/n-Si, CoPc/n-Si, CoPc/p-Si, InPcCl/p-Si and SnPcCl<sub>2</sub>/p-Si were extensively studied for their electrical and photovoltaic properties. In these device structures, the highest reported photovoltaic efficiencies are 3.76% for CoPc/p-Si and 3.05% for SnPcCl<sub>2</sub>/p-Si configurations [Riad 2000, El-Nahass et al. 2006, 2007, Hussain et al. 2010, Khan et al. 2011, Liu et al. 2012, Murtaza et al. 2012, Popielarski et al. 2013, Wahab et al. 2014, Zeyada et al. 2015, Darwish et al. 2016, Zeyada et al. 2016]. These studies concluded that the efficiency of the devices is dependent on the junction parameters such as junction

---

resistance, potential barrier-height, charge carrier mobility and nature of electrodes used in the devices.

The heterojunctions with transparent conducting oxide (TCO, acceptor) and MPcs have generated great interest for device applications. This is due to the ease of device fabrication, choice in the device configuration mode (inverted or normal mode) and the use of optically transparent metal oxide (TCO) layers. The aim of these investigations was to utilize the advantages of the material properties, such as environmental stability, optical absorption/transmission and charge carrier mobility. The heterojunctions of TiO<sub>2</sub>/CuPc, TiO<sub>2</sub>/PbPc, TiO<sub>2</sub>/AlClPc, TiO<sub>2</sub>/PBrPc, TiO<sub>2</sub>nano-tube (NT)/CuPc, TiO<sub>2</sub>/PdPc and TiO<sub>2</sub>nano-core (NC)/CuPc, TiO<sub>2</sub> NT/CuPc& TiO<sub>2</sub>nano-flower (NF)/CuPc were investigated for their electrical and photovoltaic properties. The heterojunctions of ZnO/CuPc and ZnO/ZnPc and ZnP/CoPc and ZnO/SubPc were also studied recently. ZnO has been prepared by different techniques for use in these devices. However, the photovoltaic efficiencies of these devices were very low. Hence, the interest shifted to using such heterojunctions for photodiodes [Tracey et al. 1998, Ray et al. 2001, Signerski and Kościelska 2005, Ouyang et al. 2008, Signerski et al. 2009, Mali et al. 2014].

Further, phthalocyanines were also used as an active layer in organic field effect transistor (OFET) devices and the charge carrier mobility values were estimated. In the FET configuration, Si and SiO<sub>2</sub> were used as gate and insulator, respectively. Among all these materials, the non-planar phthalocyanines TiOPc (mobility = 1-10 cm<sup>2</sup>/V-s) and VOPc (mobility = 2.6 cm<sup>2</sup>/V-s) are reported to show higher mobilities [Bao et al. 1997, Yasuda and Tsutsui 2006. Li et al. 2007, Wang et al. 2007, Song et al. 2008, Pan et al. 2011, Chen et al. 2013, Fujimoto et al. 2013, Gu et al. 2013, Rajesh and Menon 2014]. However, the electrical properties of VOPc in sandwich structures have not been investigated so far. In addition, the heterostructures based on VOPc/TCO should give a clear insight into the charge transport dynamics and the performance of the actual optoelectronic devices such as OPD, OSC, and OLED.

---

## **1.8 SCOPE AND OBJECTIVE OF THE THESIS**

### **1.8.1 Scope of the thesis**

Phthalocyanines have emerged as important materials for optoelectronic device applications. Wide varieties of MPcs (more than 70) were synthesized and several Pcs were investigated for their structural, optical, electrical and photovoltaic properties and were found to be promising materials for the photovoltaic devices. It was observed that the low photovoltaic efficiencies are dependent on the electrode/Pc interface quality and also the central metal atom which determines VB, CB values and the type of charge carriers. Furthermore, it is observed from recent literature that the non-planar MPcs with oxygen show better stability and higher mobility than other Pcs. Among many Pcs, TiOPc and VOPc are least investigated materials with regard to their electrical and photovoltaic properties. Even though, the mobilities are rather high in the FET configuration, where the properties are dependent on the insulator and dielectric layers, it is essential to investigate the charge transport properties in the sandwich structures which are integral parts of the actual optoelectronic devices (OPD, OPV and OLEDs). There is much scope to improve the charge transport properties of the sandwich structures by incorporating suitable injection and transport materials. The heterojunctions based on the ZnO/VOPc and ZnO/TiOPc devices have not been investigated so far. In view of this, it is imperative to study the electrical charge transport in both the organic (VOPc) and inorganic materials (ZnO) in sandwich structures. It is also essential to investigate the structure-electrical property correlation by varying the deposition and annealing conditions. Further, the role of these materials as a donor (p-type) and acceptor (n-type) layers in VOPc/ZnO heterojunction photodiode is vital to understand the exact nature of the p-n junction in optoelectronic devices. Accordingly, this thesis work has been carried out with the following objectives.

---

### 1.8.2 Objectives of the thesis

- i. To study the morphological, structural and electrical properties of VOPc thin films.
- ii. To prepare and study the structural, morphological, optical and electrical properties of ZnO nanoparticulate thin films and ZnO nanorod (ZNR) thin films.
- iii. To fabricate the heterojunction devices in ZnO/VOPc configuration and determine their optoelectronic properties.
- iv. To fabricate the heterojunction devices in ZNR/VOPc configuration and determine their optoelectronic properties.

### 1.9 ORGANIZATION OF THE THESIS

The contents of this thesis have been divided into seven chapters with several sections in each chapter.

**Chapter 1** is the introductory chapter and it presents the background and motivation for the present work. This chapter describes the basic properties of the organic semiconductors as well as the design and working of the Photodiode devices. Further, a review of the earlier work on organic semiconductors and their application to the organic optoelectronic devices is presented. Lastly, the scope and objectives of the thesis are described.

**Chapter 2** discusses the various materials, device structures, device fabrication and characterization techniques used in this work. A brief theoretical description and relevant formulae used for the estimation of key parameters are provided for all the measurements. The experimental setup used in our laboratory for the electrical and optoelectronic characterizations of the fabricated devices is also described.

**Chapter 3** discusses the experimental investigation of the charge (hole) transport in VOPc thin films using measurements of current density, capacitance and impedance spectroscopy. The morphology dependent electrical properties of VOPc as a function of deposition rate are investigated. The role of the MoO<sub>3</sub> buffer layer and the

---

dependence of the charge conduction of VOPc on the temperature and bias voltage is discussed in detail.

**Chapter 4** discusses the preparation and experimental investigation of electron transport studies in ZnO nanoparticulate thin films. The morphology dependent electrical properties of ZnO as a function of annealing temperature are analyzed by using current density, capacitance and Impedance spectroscopy measurements. The studies on optical, structural and morphological properties of the films are also presented.

**Chapter 5** presents the characterization of the p-n junction diodes made using organic (VOPc) and inorganic (ZnO) thin films. It is demonstrated that the VOPc/ZnO p-n junction devices are potential candidates for photodiode applications.

**Chapter 6** discusses the preparation of ZNR thin films and its suitability for VOPc/ZNR hybrid p-n junction photodiodes. The morphology dependent electrical and optoelectronic properties of these devices are presented in detail.

**Chapter 7** presents a summary of the work presented in the thesis along with the important conclusions drawn from the study. Scope for future research is mentioned at the end.

Appendix, a list of references and a brief resume, including publications in international journals and conferences, are given at the end of the thesis.

---

## CHAPTER 2

### MATERIALS AND EXPERIMENTAL TECHNIQUES

#### *Overview*

*Chapter 2 describes the various organic materials, device structures, device fabrication and characterization techniques used for the work presented in this thesis. It starts with a brief description of materials, their classification according to their functionalities and their properties. This is followed by a description of characterization techniques used for the study of structural, morphological, optical and electrical properties. A description of other instruments used to analyze the materials is also presented. Different device structures that were employed are explained.*

#### **2.1 MATERIALS USED IN THIS WORK**

The materials selected for this study are based on their functional properties in the fabricated devices. The key material properties are hole injection, hole transport (and/or donor), electron transport (and/or acceptor) and nature of the electrodes. We have found it convenient to select both organic semiconductors as well as inorganic semiconductors. The molecular energy levels of some of the materials used in this work are shown in Figure 2.1. The materials, VOPc, MoO<sub>3</sub> and Al were obtained from commercial sources and were used as received without any further purification. ZnO nanoparticles and nanorods, for use in some of the devices, were synthesized in our laboratory and their synthesis, structural, morphological properties are presented in detail in Chapter 4. The materials used for this study are described below.

**2.1.1 Transparent electrode:** Glass substrates with patterned indium tin oxide (ITO, 120 nm), having a sheet resistance of 15Ω/□ and functioning as the transparent electrode, were procured from M/s Kintec Company, Hong Kong, for the proposed devices. The work function of the ITO varies from 4.4eV to 4.9 eV, depending on the method employed for depositing ITO film and subsequent surface treatment carried out prior to the deposition of the organic or inorganic layers [Djurišić et al. 2003, Lee

and Chung 2008].

In this study, ITO was used either as an anode or cathode based on the device configurations. It is used as an anode to inject holes into the organic (VOPc) layer as described in Chapter 3. In Chapter 4, 5 and 6, the use of ITO as a cathode to inject electrons into the inorganic (ZnO) layer is described. The nomenclature of the materials used in this study is given in Table 2.1

**Table 2.1** Organic and inorganic material used in this thesis

Abbreviation	Chemical description
VOPc	:Vanadium(IV)phthalocyanine oxide,
MoO <sub>3</sub>	:Molybdenum trioxide
ZnO	:Zinc oxide

**2.1.2 Hole injection material:** The inorganic material, MoO<sub>3</sub> (Sigma-Aldrich, 99.98% trace metal basis), was used as a hole injection material (HIM) in this study due to the fact that its HOMO energy level (5.3eV) is close to the work functions of both the electrode materials, viz., ITO and Al [Zhu et al. 2001, Greiner et al. 2013]. The HOMO, LUMO and the work functions of the materials used in this thesis are shown in Figure 2.1.

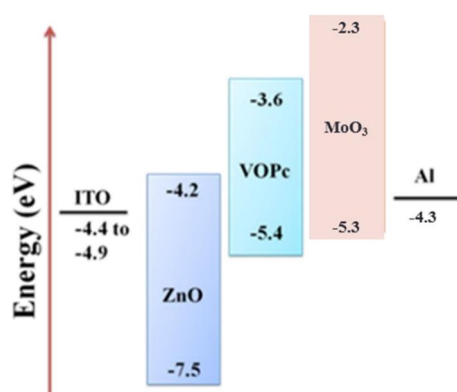


**Figure 2.1** HOMO and LUMO energy levels of all the semiconducting materials used for the fabrication of various devices for the works reported in this thesis.

**2.1.3 Hole Transport Material:** In the present study, Vanadyl phthalocyanine (VOPc, Alfa Aeser, > 85% dye content) was used as a hole transport material (HTM). It is often used in OLEDs and Organic Solar cells as HTM because of its film-forming

---

capability and low lying HOMO ( $\sim 5.4\text{eV}$ ) levels, along with a hole mobility of  $0.26\text{cm}^2/\text{V}\cdot\text{s}$  measured in a FET configuration [Pan et al. 2011].

**2.1.4 Electron Transport material:** Sol-gel synthesized ZnO nanoparticles and nanorods were used as electron transport materials (ETM). Both these have a Conduction band (CB) energy value of  $4.2\text{eV}$ , which is closer to the work function of ITO and Al, used as electrodes in this study. They are often used as an ETM in organic solar cells, OLEDs and hybrid devices due to greater chemical stability as compared to organic n-type materials and high electron mobility (approximately  $1\text{-}40\text{ cm}^2/\text{V}\cdot\text{s}$  in FET configuration [Ong et al. 2007, Esro et al. 2015]). The conduction band and valence band energy levels of ZnO are approximately  $4.2\text{eV}$  and  $7.5\text{eV}$ , respectively [Yoon et al. 2012].

**2.1.5 Metal electrode:** Aluminium (Al, Alfa Aeser, purity  $>99.99$ ) film, with a thin over-layer of  $\text{MoO}_3$ , was used as the metal electrode. It has a work function of approximately  $4.3\text{eV}$  [Yip and Jen 2012]. It is known that the work function of ITO and Al increases with the addition of a overlayer of  $\text{MoO}_3$  [Greiner et al. 2013a].

## 2.2 MATERIALS CHARACTERIZATION

### 2.2.1 X-Ray Diffraction

X-ray diffraction (XRD) was performed using a Rigaku600 MiniFlex diffractometer equipped with Copper target emitting  $\text{K}\alpha$  ( $\lambda = 1.5405\text{\AA}$ ) radiation (Figure 2.2). The analysis of the XRD patterns of thin films used in this study yields information regarding the crystallinity and size distribution of the crystallites. The basic principle involved in the diffraction studies is the well-known Bragg's law and is given by [Cullity 1956]

$$n\lambda = 2d \sin\theta \quad (2.1)$$

where  $n$  is the order of diffraction,  $2\theta$  is the angle of diffraction and  $d$  is the inter-planar distance in the crystalline material. The inter-planar spacing depends on the dimensions of the crystal unit cell, whereas, the intensity of the diffracted rays is a

---

function of the arrangement of the atoms in the unit cell. The crystallite size can be estimated using the well-known Scherrer's equation [Cullity 1956].

$$t = \frac{K\lambda}{B\cos\theta} \quad (2.2)$$

where B is the full width at half maximum (FWHM) of the most intense diffraction peak and K is the shape factor, which usually has a value of 0.9.



**Figure 2.2** Rigaku 600 MiniFlex diffractometer

### **2.2.2 Atomic force microscopy (AFM)**

AFM is a high-resolution imaging technique that can resolve the surface features of the test sample down to a unit cell. The AFM consists of a cantilever which is made up of silicon or silicon nitride with a sharp tip (probe) of radius of curvature of the order of nanometers. This arrangement is used to scan the surface of the specimen. When the tip is brought into the proximity of a sample surface, the electric force between the tip and the specimen lead to a deflection of the cantilever. AFM can be operated in static (contact) or dynamic (non-contact or tapping) modes depending on the application. The surface topography of the samples in this study was observed using Park XE70 atomic force microscope in non-contact mode (Figure 2.3).

In non-contact mode, the AFM tip does not get damaged and there is no scratching of the specimen surface as tip does not touch the surface. The typical distance between the tip and the specimen surface is about 5–14 nm. Thus, non-contact mode is preferable for surface imaging of any soft specimen such as

---

biological samples and organic thin films. The Van der Waals forces acting between the tip and the specimen are sensed and the topographic images are recorded by scanning the tip over the surface. As the attractive forces from the sample surface are substantially weaker than the forces used by non-contact mode, the ac detection methods can be used to detect the small forces between the tip and the sample by measuring the change in amplitude, phase or frequency of the oscillating cantilever in response to the force gradient from the sample [Zhang et al. 2008]. For best resolution, it is necessary to measure force gradients arising out of Van der Waals forces, which may extend only up to a nanometre from the sample surface.



**Figure 2.3** Park Xe70 Atomic Force Microscopy [at NIE, Mysore, India]

### **2.2.3 Scanning Electron Microscopy (SEM)**

The field emission microscope (FESEM, shown in Figure 2.4) is a type of electron microscope that constructs the image of the sample surface by scanning it with a thin high energy electron beam in the raster scan pattern. When the electron beam hits a point on the sample, numerous interactions occur between the incident electrons and the atoms of the specimen. These interactions generate a wide variety of signals such as backscattered electrons, secondary electrons, absorbed electrons, characteristic and continuum x-rays, etc. The secondary electrons have relatively low energy and can be easily detected by the detector. The detector counts the number of electrons emitted from the sample and the resulting pattern is displayed on the computer. The spot size in a FESEM is smaller than the conventional SEM. Therefore, it can produce very high-quality images with a spatial resolution in the

---

range of 1-5 nm. In this study, the surface morphology of the thin films was recorded using Zeiss Sigma FESEM operated at an accelerating voltage in the range 5kV - 15kV.



**Figure 2.4** Scanning Electron Microscopy (FESEM) [at Mangalore University, India]

The surface morphology of the inorganic thin films, such as ZnO thin films was also obtained using the same FESEM and is discussed in the subsequent chapters.

#### **2.2.4 UV- Vis absorption and transmission spectra**

UV-Vis absorption spectrum gives an insight into the absorption of the electromagnetic radiation by the test sample. The absorption process is governed by the Beer-Lambert's law, using which, the absorption/transmission coefficients can be determined by recording the intensity of transmitted light beam through test samples of varying thickness. When the light is incident on the sample, a part of the light will be reflected by the sample, a part will be transmitted through the sample and the rest of the beam will be absorbed. Absorption of photons results in the transition of electrons from the lower energy level to the higher energy levels. The Beer-Lambert's law is written as

$$I_T = I_{T0} \exp(-\alpha d) \quad (2.3)$$

Here,  $I_T$  is the transmitted light intensity and  $I_{T0}$  is the intensity of the incident light,  $\alpha$  is the absorption coefficient and  $d$  is the thickness of the sample.

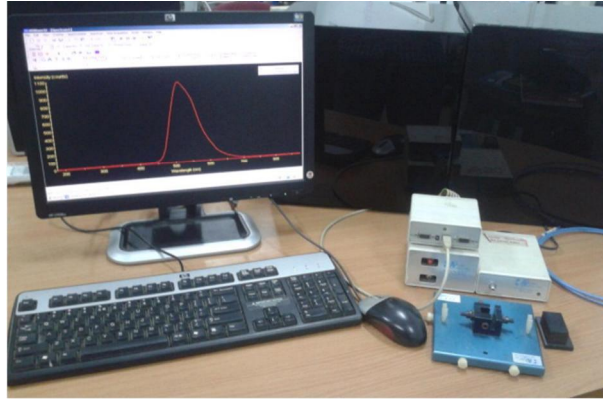


**Figure 2.5** Ocean Optics SD2000 Spectrophotometer

The relation between the absorption coefficient and the optical band gap of the material is given by

$$\alpha = \frac{A(h\nu - E_g)^r}{h\nu} \quad (2.4)$$

Here the material is assumed to possess a parabolic band structure. In Eq.(2.4) the parameter A depends on the transition probability,  $E_g$  is the band gap,  $\nu$  is the frequency of the incident light. The constant  $r$  represents the nature of the electronic transition. For direct allowed transitions  $r = 1/2$ ,  $r = 2$  for indirect allowed transitions,  $r = 3$  for indirect forbidden transitions and  $r = 3/2$  for direct forbidden transitions [Pankove J. I, 2010].

In the present study, the optical absorption/transmission spectra of the samples were recorded using the Ocean Optics SD2000 spectrophotometer shown in Figure 2.5. This instrument consists of a deuterium lamp (UV) and a halogen lamp (Vis) as sources and has a resolution of 0.6 nm in the UV/Visible region. To obtain the absorption or transmission coefficients of the inorganic/organic thin films, the absorption/transmission spectra of a blank glass plate was subtracted from the spectra of each sample.

### 2.3 DEVICE STRUCTURES

In this present work, three types of devices were fabricated: hole only devices, electron-only devices, and organic-inorganic p-n junctions. In this section, the device structures are described.

---

**2.3.1 Hole only devices:** In order to study the hole transport properties in organic materials, hole-only devices were fabricated. A thin film of an organic material was sandwiched between ITO and Al electrodes to fabricate hole only devices. To improve the charge transport through the organic material, a thin hole injection layer was also incorporated in the structures. The details are discussed in Chapter 3. Figure 2.6(a) shows a schematic of the device used for the hole transport study.

**2.3.2 Electron only devices:** To study the electron transport properties in the inorganic semiconductors, a series of electron-only devices were fabricated. Morphology and annealing temperature dependence of charge transport was also investigated for the inorganic materials. The details are presented in Chapter 4. Figure 2.6(b) shows a schematic of the device used for the electron only devices in this study.

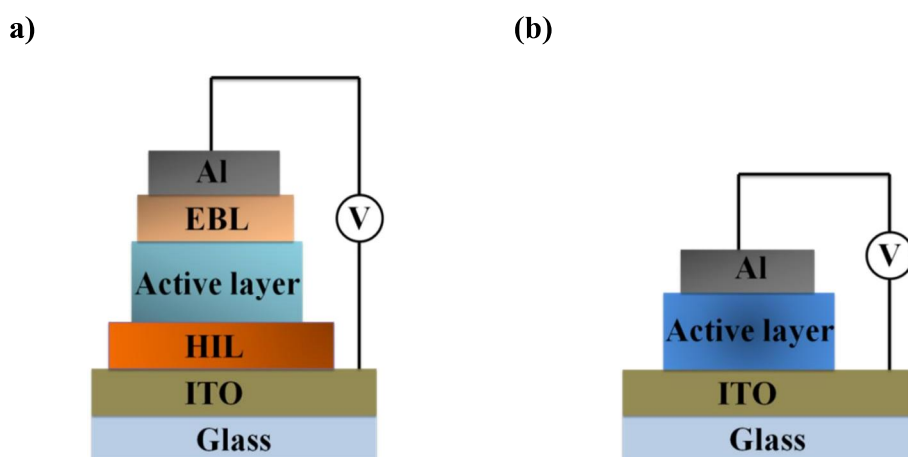


**Figure 2.6** (a) Schematic device structure of the hole only devices and (b) electron-only devices

**2.3.3 Organic-inorganic p-n junction:** Figure 2.7 shows the structure of a typical organic-inorganic hybrid p-n junction device fabricated for the charge transport investigations. In these devices, multiple layers of inorganic and organic layers are deposited over a transparent electrode on a glass substrate. ITO as a cathode allows visible light to fall on the active layers of the device. The other layers of the p-n junction are ETL/acceptor (inorganic), HTL/ donor (organic) and HIL or/and EBL. Finally, a metal electrode is deposited on the top to function as an anode. In this

---

study, MoO<sub>3</sub> is used as a HIL while VOPc was used as a HTL/donor and ZnO as a ETL/acceptor.

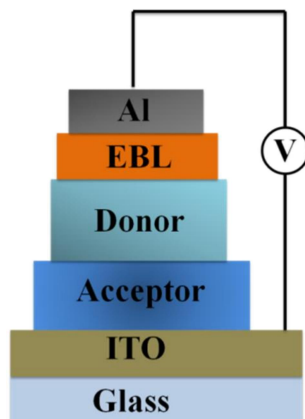


**Figure 2.7** Typical device structure of the organic-inorganic hybrid p-n junction device

## 2.4 DEVICE FABRICATION

In this section, the steps used in the device fabrication are discussed in brief.

### 2.4.1 Cleaning of the patterned ITO coated glass substrates

Proper cleaning of the substrate is very crucial for the successful fabrication and reliable performance of the devices. A small amount of contamination on the surface of ITO can severely alter its work function and/or interfacial barrier height between the organic layer and ITO. Unless the anode is thoroughly cleaned, the electrical and optical characteristics can be highly unstable and unpredictable. Therefore, the substrates are thoroughly cleaned before the deposition of the required thin film. Pre-patterned ITO coated substrates have four ITO stripes (2mm x 25mm) separated by a 2mm gap. The thickness and the sheet resistance of each stripe are 120 nm and 15Ω/□, respectively. These substrates are first mechanically washed with labolene solution and rinsed well using distilled water. Next, these substrates are sequentially ultrasonicated in labolene (to remove oil contaminants), distilled water (to remove detergent), acetone (to remove the chemical contaminants) and 2-propanol (to remove acetone stains), respectively, for about 20 min duration for each step. Further, the substrates are ultrasonically cleaned with distilled water multiple times

---

and then dried using ultra-pure (99.999%) N<sub>2</sub> gas. Finally, the substrates are degreased with acetone and then dried in a vacuum oven for 10 min at a temperature of 100<sup>0</sup>C. To improve the wettability and the work function of ITO, the cleaned substrates were treated by UV generated ozone for 15 min. This treatment has been proved to increase the work function of ITO from 4.5eV up to 4.9eV [Djurišić et al. 2003, Brütting 2005].

#### **2.4.2 Fabrication procedure**

In the present work, both vacuum thermal evaporation (VTE) and sol-gel spin coating techniques (SSC) were employed for thin film deposition depending on the material. VTE technique is often used to make thin films of organic small molecules which are thermally stable. This process is based on the sublimation of the material, kept in a Molybdenum boat, by resistive heating of the boat under high vacuum ( $\sim 10^{-6}$  mbar). On the other hand, in SSC, the solution-gel is deposited, using a microsyringe, onto the substrate mounted on the Spin-Coater platform. The Spin-Coater is then turned on so as to spin the substrate at the desired speed. Centrifugal force drives the solution to spread uniformly on the rotating substrate resulting in a film of the required thickness. The solvent evaporation and annealing of the films are necessary steps to be taken after the spin coating of thin film to get desired optoelectronic properties

**2.4.3 Fabrication of hole only devices:** The fabrication of the hole only devices was carried out using a custom-made VTE system shown in Figure 2.8. This system is capable of evaporating six materials with a rotary filament (boat) arrangement. This enables one to sequentially evaporate six materials without breaking the vacuum. This system is also equipped with turbo molecular pump (backed by Roots pump) to eliminate contamination by oil vapours.

For the fabrication of all the devices, the substrate to source (molybdenum boat/ tungsten filament) distance was maintained as 15 cm. The organic materials in granular or powder form, used for the deposition, were put into small molybdenum boats. For deposition of Al, aluminum wire (purity of 99.95%) was placed in a tungsten helical filament. The entire chamber was pumped down to a base pressure of

---

$\sim 10^{-6}$  mbar and the source was heated by passing electrical current (resistive heating) through the boats containing them. The evaporated materials condense on the surface of the substrate. The current flow through the boat/filament was controlled manually such that the evaporation rates for  $\text{MoO}_3$ , and Al metal electrode, were 0.1-0.2 Å/s, 0.1-0.2 Å/s, and 5-6 Å/s, respectively. The deposition rate of the organic material (VOPc) was varied for studying its effect on the device properties; this is discussed in Chapter 3. The effective device area was  $\sim 1.6 \text{ mm}^2$ , which was achieved using a shadow mask. The film thickness and the deposition rates were monitored in-situ by a quartz crystal balance. During the multilayer deposition, in between two successive depositions, the chamber was pumped down to high vacuum and kept in that condition for 30 min to avoid contamination from the previously evaporated material.



**Figure 2.8** VTE system equipped with turbo-molecular pump used for the fabrication of hole- only devices and inorganic-organic p-n junction devices.

**2.4.4 Fabrication of electron-only devices:** For these devices, the active layer was deposited on the pre-cleaned ITO substrate by means of sol-gel spin coating technique. The details of the preparation of precursors for the active layer deposition are discussed in Chapter 4. Spin coating was done using Milman-SPN2000 Spin Coater (shown in Figure 2.9). This is a two stage spin coater having the option to vary the rotation rate ramping-up at each stage and finally ramp down to zero speed. In this thesis, the samples were coated at a spin speed of 500 rpm for the first 30s and 1000 rpm for the next 30s. The ramping speed was set at 100 rpm/s between two stages.

---

The spin-coated substrates are subjected to heat treatment to enable evaporation of the solvent.



**Figure 2.9** Milman SPN 2000 Spin coating unit

For fabrication of electron-only devices with films of an inorganic semiconductor with different morphologies, spin coating with solvent evaporation step was repeated 3 times to get films of the required thickness. The deposited thin films were subjected to different annealing temperatures for about 1 hr. Finally, the Al layer (cathode) was deposited over the spin-coated (annealed) films using a shadow mask.

**2.4.5 Fabrication of hybrid p-n junctions:** The fabrication of p-n junction was a three-step process in which both spin coating and VTE were utilized as described below:

Step 1: The inorganic material, ZnO, was spin coated on the pre-cleaned substrates and annealed at the desired temperatures.

Step 2: The organic material, VOPc, was evaporated thermally on the ZnO/ITO layers (films annealed in step-1) at a base pressure of  $\sim 10^{-6}$  mbar.

Step 3: Finally, the MoO<sub>3</sub>/Al electrode was deposited over the organic materials using the shadow mask.

## **2.5 ELECTRICAL CHARACTERIZATION**

The fabricated devices were characterized electrically by measuring the current-voltage characteristics and by impedance spectroscopy. The suitability of

---

these methods for our devices is discussed in this section along with a brief theoretical background.

### 2.5.1 Current density-voltage ( $J$ - $V$ ) characteristics

Current density-voltage characteristic ( $J$ - $V$ ) were obtained by measuring the current through the device upon varying the bias voltage. The  $J$ - $V$  characteristics are used to determine the basic electronic properties of the organic semiconductors in different device configurations. One may estimate material properties such as charge injection, electrical conductivity and, hence, the mobility. Optimization of the device performance requires a good understanding of not only the electrical properties of individual materials used in device, but also the details of device architecture. They yield a good insight into the underlying conduction mechanism that operates in the devices as well as role of the quality of the interfaces between the organic semiconductor layer and the electrodes.

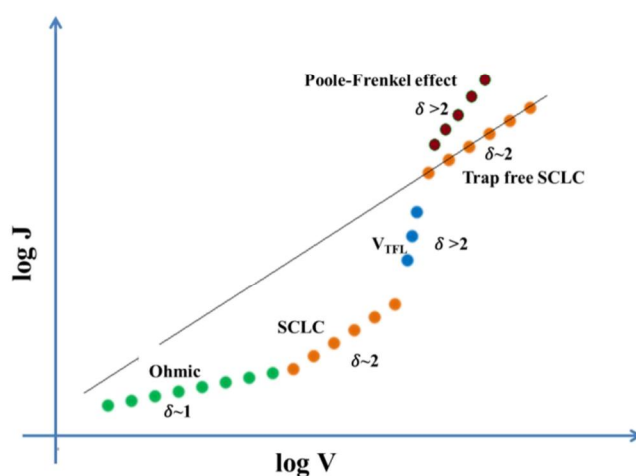


**Figure 2.10** Typical  $J$ - $V$  characteristics of the electronic devices illustrating different regimes of electrical conduction.

$J$ - $V$  characteristics of metal/semiconductor/metal devices are controlled by two basic processes: (i) the charge carrier injection from the electrodes into the semiconductor, and (ii) the charge carrier transport through the bulk of the film. The difference between the electrode work function and the HOMO (or LUMO) of the organic semiconductor determines whether the charge transport is injection limited or

---

bulk limited. One can also derive information regarding charge trapping as well as the intrinsic bulk mobility of the charge carriers in a given device configuration. Further, a precise control over the deposition parameters can minimize the surface states at a metal/semiconductor interface, which is of vital importance.

In the case of single carrier devices, the current density under forward bias usually shows a power law dependence on the applied voltage (see Figure. 2.10) [Gould 1996, Shafai and Anthopoulos 2001], and is given by,

$$J \propto V^\delta \quad (2.5)$$

where  $\delta$  is the slope of the J-V characteristics and may take different values in different regions of the J-V plot. The first region  $\delta = 1$  is the ohmic region. The second regime ( $\delta \sim 2$ ) indicates that the electrical conduction in this region follows the SCLC mechanism with traps. The third region (high value of  $\delta$ ) is the transition region wherein deep traps get filled by the injected charge carriers, leading to a transition from the trap charge SCLC conduction mechanism to the trap-free SCLC ( $\delta = 2$ ) mechanism. This region is known as the trap filled limit region (TFL) [Stallinga 2009]. When high electric fields are applied, some of the trapped charges are ejected from the traps. Therefore, the current density and hence the slope of the J-V plot reduces in comparison with the TFL region without achieving the trap-free SCLC. This region is described by the Poole-Frenkel effect [Spahr et al. 2013]. The mobility estimation from SCLC analysis will be discussed in the subsequent chapters in this thesis.

In this study, J-V characteristics were measured (under dark and illuminated conditions) using the Source Measure Unit (SMU) Keithley 2400 interfaced to a computer through the IEEE488.1 interface. Labtracer and Kickstart software were used to operate the SMU through the computer.

### **2.5.2 Capacitance-Voltage (C-V) Characteristics**

The typical Capacitance-voltage characteristics (C-V) for a single layer device is shown in Figure 2.11(a) and the corresponding Mott-Schottky plots are presented in Figure 2.11(b). The C-V characteristics are used to estimate the concentration of

conduction charge carriers in a single carrier type device. It was shown that the C-V analysis for a single carrier device can also provide information about the quality of the injection barrier and the built-in voltage resulting from the use of different metal contacts [Nowy et al. 2009, Sharma et al. 2011, Ramar et al. 2014]. This analysis is also used to monitor the dynamics of an electron-hole pair in two-layer devices such as OLED, OPD and OPV [Macdonald 1992, Nowy et al. 2009].

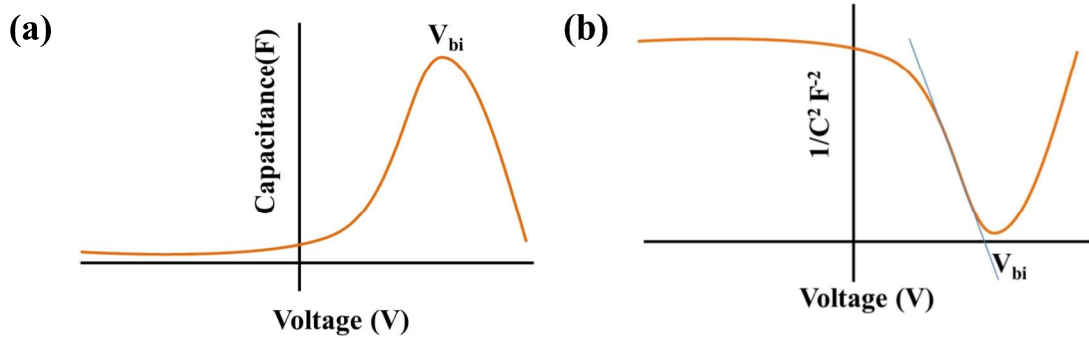


**Figure 2.11(a)** Typical Capacitance-voltage characteristics and (b) Mott-Schottky plots for a single layer device.

According to the standard Mott-Schottky equation, the dependence of capacitance on the applied bias is given by [Singh and Ghosh 2015]

$$\frac{1}{C^2} = \frac{2(V_{bi} - V)}{A^2 q \epsilon_0 \epsilon_r N_A} \quad (2.6)$$

where  $V_{bi}$  is the built-in voltage,  $A$  is the interface area of the device,  $q$  is the electron charge,  $\epsilon_r$  is the dielectric constant of the material,  $\epsilon_0$  is the absolute permittivity and  $N_A$  is the effective charge carrier concentration of the conduction charge carriers.

In this study, C-V measurements were carried out using Agilent E4980A, 20Hz-2MHz precision LCR meter at a fixed frequency of 1 KHz with ac amplitude of 500mV. Prior to the measurements, the system was corrected for short and open measurements

---

### 2.5.3 Impedance Spectroscopy (IS)

Impedance spectroscopy is a widely used non-destructive characterization technique to study many of the electrical properties of the semiconducting materials and their interfaces. It is often employed to obtain information related to the factors influencing charge transport, quality of the electrodes used for device fabrication, nature of electrode/semiconductor interface, defect density at the electrode/semiconductor interface, defect density in the bulk of the semiconductor, charge injection efficiency and mobility. From the literature, it is observed that IS has been successfully applied to investigate a variety of issues in organic materials.

In a typical measurement involving IS, a small ac signal,  $V_{ac}(t) = V_1 \sin(2\pi ft)$  with an amplitude  $V_1$  and frequency  $f$ , is applied to the device in addition to a dc bias voltage  $V_{dc} = V_0$ . Therefore, the total bias voltage applied to the device and the current through it are given by

$$V = V_0 + V_1 \sin(2\pi ft) \quad (2.7)$$

$$I_{ac}(t) = I_1 \sin(2\pi ft + \varphi) \quad (2.8)$$

where  $\varphi$  is the phase shift between the voltage and current. Electrical impedance,  $Z(f)$ , is a complex quantity and is defined as the ratio of the voltage phasor ( $\hat{V}$ ) to the current response phasor ( $\hat{I}$ ), to include their phase angles, and may be written

$$Z(f) = \frac{\hat{V}}{\hat{I}} = \text{Re}[Z] + i \text{Im}[Z] \quad (2.9)$$

The real and imaginary parts of the complex impedance are given by

$$\left. \begin{aligned} \text{Re}[Z] &= Z \cos\theta & \text{Im}[Z] &= Z \sin\theta \\ \text{Therefore } |Z| &= \sqrt{(\text{Re}[Z])^2 + (\text{Im}[Z])^2} \\ \text{The phase angle } \varphi &= \tan^{-1} \left( \frac{\text{Im}[Z]}{\text{Re}[Z]} \right) \end{aligned} \right\} \quad (2.10)$$

If the real and imaginary parts of impedance are plotted against each other, one may obtain a single semicircle, or a plot which may be a combination of

semicircles, depending on the response of the device to the total applied voltage, as shown in Figure 2.12(a). In Figure 2.12(b),  $R_s$  represents the series resistance of the device. This series resistance is analogous to the resistance at the metal/semiconductor contacts.  $R_p$  represents the parallel resistance of the device which is the electrical resistance of the bulk of the film sandwiched between the metal electrodes. The parameter  $C_p$  is the parallel capacitance of the device.

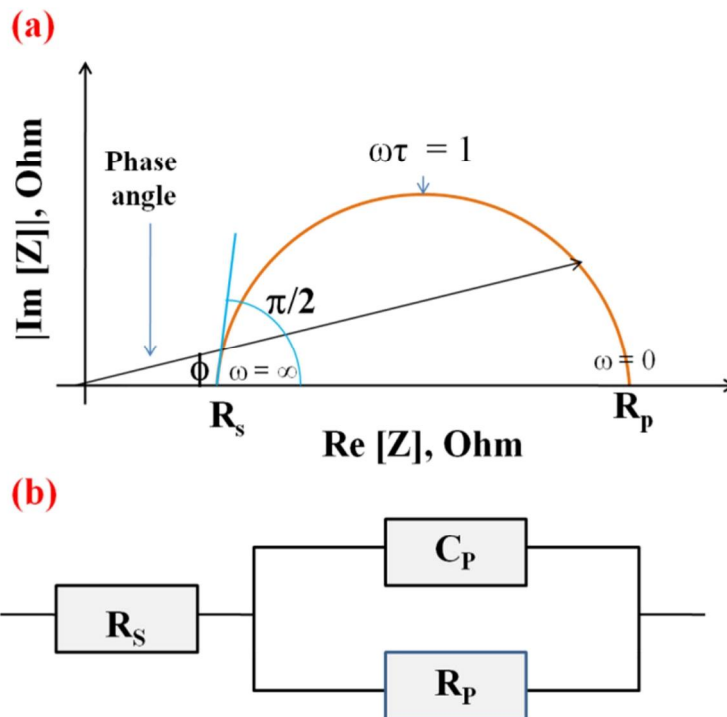


**Figure 2.12** Plot of  $\text{Im}[Z]$  versus  $\text{Re}[Z]$ , also known as Cole-Cole plot, and (b) the corresponding equivalent circuit to model the Cole-Cole plot.

In the present work, the impedance measurements were done using Agilent E4980A, 20-2MHz precision LCR meter equipped with 16089B Kelvin clip lead (Figure 2.13(a & b)). This instrument can provide ac voltage in the range of  $\pm 12\text{V}$  and dc voltage in the range of  $\pm 40\text{V}$ . All the IS measurements in this work were performed at a constant ac amplitude of 100mV. Prior to the measurements, the system was corrected for short and open measurements.

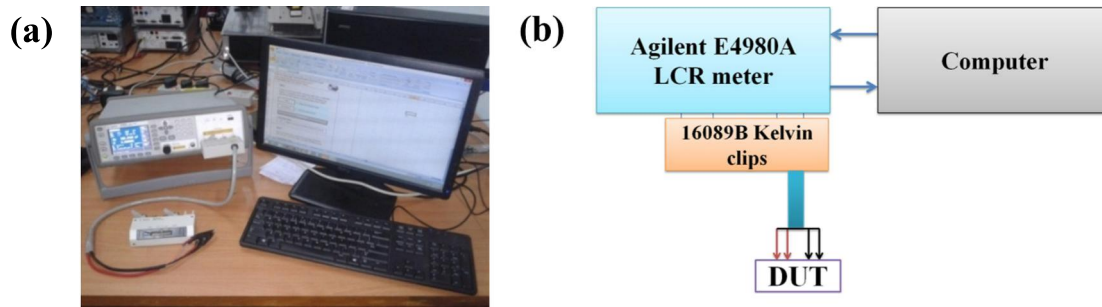


**Figure 2.13** (a) Impedance measurements setup (Agilent 4980A) and (b) schematic of the setup for the IS measurements.

#### 2.5.4 Characterization of Devices under illumination

Hybrid p-n junctions were fabricated for our investigations. They were characterized through J-V, C-V and IS measurements in the dark condition as well as under illumination. The devices were illuminated inside a custom-made lamp-housing having a 150W metal halide lamp. The incident power of the light on the sample surface was measured using Ophir NOVA2 power meter. The detailed analyses are presented in Chapter 5 and 6. Since the VOPc has an absorption peak around 660nm (as shown in Figure 2.14), the responsivity of all the photodiodes in this thesis were estimated with respect to the incident light wavelength of 600nm.

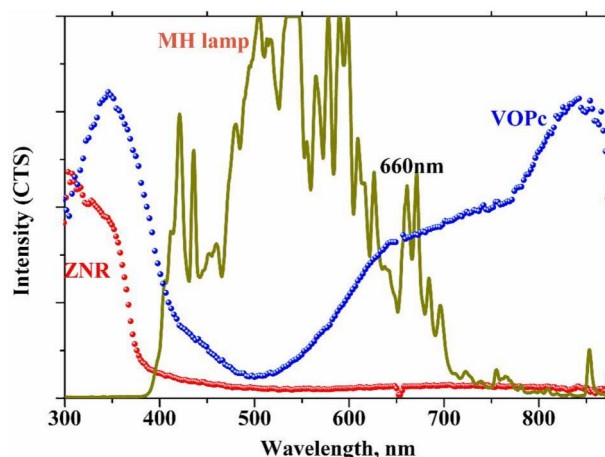


**Figure 2.14** Emission spectrum of the metal halide lamp (dark green) and the absorption spectra of the ZNR (red dots) and VOPc (blue dots) films.

---

## **2.6 CONCLUSION**

In this chapter, a brief description of the materials used for fabricating our devices was presented. The different techniques to characterize the materials for their structural, morphological, and optical properties were described. The different techniques employed for fabricating the devices and the various electrical and optoelectronic characterization techniques were explained in detail, thus laying the foundation for the chapters to follow.



---

## CHAPTER 3

### CHARGE TRANSPORT INVESTIGATIONS IN HOLE- ONLY DEVICES MADE USING VANADYL PHTHALOCYANINE THIN FILMS

#### *Overview*

*This chapter explores the charge transport properties of Vanadyl phthalocyanine (VOPc) thin films in hole-only device configuration: ITO/MoO<sub>3</sub>/VOPc/MoO<sub>3</sub>/Al. The VOPc thin films were characterized for their structural and morphological properties. The morphology-electrical property relation for the VOPc films was established using various electrical characterization techniques which include J-V, C-V and IS studies. The results suggest that the VOPc films deposited at lower rates are better suited for optoelectronic applications as they possess higher hole mobility.*

#### 3.1 INTRODUCTION

The electronic structure of metal phthalocyanines (MPcs) and their optical, morphological and electrical properties play an important role in device applications. Special attention has been devoted to MPcs due to their environmental stability [Ohta et al. 2003]. Several investigations have been reported on charge transport and device applications of planar phthalocyanines (CuPc and ZnPc) as well as non-planar phthalocyanines (SubPc and TiOPc)[Kim and Yim 2011, Williams et al. 2014]. Non-planar phthalocyanine-based devices offer better performance in comparison with planar phthalocyanines [Song et al. 2008, Jin et al. 2014]. An example of such a material is VOPc which has been used in several optoelectronic devices such as OLEDs, OPVs, OFETs and sensors [Williams et al. 2014]. However, the charge transport in VOPc based devices has not been extensively investigated.

In order to achieve higher device performance, it is essential to understand the charge conduction mechanism that operates in these devices. In this chapter, the effects of the deposition rate on the transport properties of VOPc in hole-only devices with the configuration: ITO/MoO<sub>3</sub>/VOPc/MoO<sub>3</sub>/Al is discussed. The dependence of

---

electrical conductivity on the frequency of the applied signal, bias voltage, and temperature was investigated in order to understand charge transport mechanism operative in these devices.

## **3.2 FABRICATION AND CHARACTERIZATION OF THE DEVICES**

### **3.2.1 Fabrication of hole only devices**

Several devices with different deposition rates of VOPc were fabricated by sequentially evaporating MoO<sub>3</sub> (3 nm, 0.1–0.2 Å/s), VOPc (100 nm) and MoO<sub>3</sub> (3 nm, 0.1–0.2 Å/s) on the pre-cleaned patterned ITO (120 nm) substrates. A 100 nm thick Aluminium (Al) layer was deposited at a rate of 5–6 Å/s on the top layer of MoO<sub>3</sub> using a shadow mask to function as a cathode. The deposition rate of VOPc was maintained at 0.1–0.2 Å/s, 1–2 Å/s and 5–6 Å/s, respectively, for these devices. For simplicity, these deposition rates are denoted as 0.1 Å/s, 1 Å/s and 5 Å/s throughout the chapter. During the deposition, the substrates were maintained at room temperature under a vacuum of  $8 \times 10^{-6}$  mbar. The active area of the device was 0.016 cm<sup>2</sup>. All the devices were characterized under ambient conditions without encapsulation.

### **3.2.2 Structural and morphological properties**

The structure of VOPc is illustrated in Figure 3.1(a). Ziolo et al. [1980] first determined the VOPc crystal structure along with TiOPc. VOPc molecule has C<sub>1</sub> symmetry and belongs to the non-planar category of Pcs. The vanadium atom is five-coordinated in a square pyramidal geometry and is 0.575 Å above the plane of four Nitrogen atoms. The V=O distance is 1.580 Å; the V-N distance does not differ significantly and has a mean value of 2.026 Å [Ziolo et al. 1980, Tverdova et al. 2013]. VOPc is known to exhibit polymorphism and exists in three polymorphic phases namely phase I, phase II and phase III. Among these phases, VOPc of phase II is a stable form of the molecule. Phase I is deemed to be a meta-stable form and phase III is reported to be a result of fast cooling VOPc from the melt (>600<sup>0</sup>C) [Griffiths et al. 1976, Wang et al. 2014b, J. Ramadan et al. 2016].

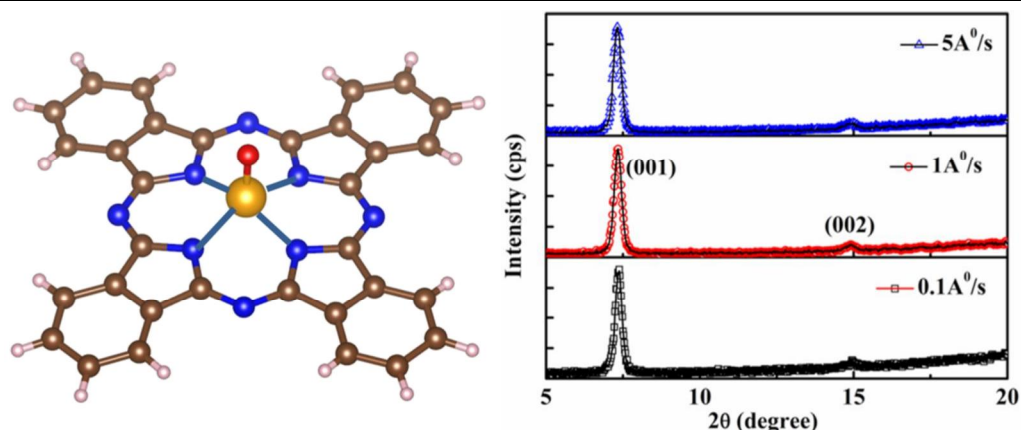


**Figure 3.1(a)** molecular structure of VOPc; the yellow, blue, brown and pink coloured spheres represent vanadium (V), Nitrogen (N), carbon (C), Hydrogen (H) atoms, respectively and **(b)** X-ray diffraction patterns of the VOPc thin films at different deposition rates

The X-ray diffraction patterns of all the VOPc films (deposited at 0.1 Å/s, 1 Å/s, and 5 Å/s) prepared at room temperature is shown in figure 3.1(b). The existence of different phases of VOPc thin films has been widely investigated [Pan et al. 1998a, 1998b]. However, in this study, the VOPc thin films were identified to be in the phase-II structure. The most intense characteristic peak, observed at  $2\theta = 7.38^\circ$ , corresponds to an inter-stack spacing of 11.9 Å. This implies the predominance of (001) orientation of the VOPc occurring with the backbone (a-axis) parallel to the surface plane of the substrate [Pan et al. 1998b]. The low-intensity diffraction peak (002) observed at  $2\theta = 14.9^\circ$  corresponds to the inter-stack distance of 5.9 Å. The full width at half maximum (FWHM) for the films prepared at 0.1 Å/s, 1 Å/s, and 5 Å/s are  $2\theta = 0.22^\circ$ ,  $0.29^\circ$  and  $0.37^\circ$ , respectively, which indicates that the grain size/crystalline nature decreases with increase in deposition rate. The average grain size can be calculated using Scherrer's formula (see Eq. 2.1).

The average grain sizes of the VOPc thin films at different deposition rates were found to be 36.2 nm, 27.4 nm and 21.4 nm for 0.1 Å/s, 1 Å/s and 5 Å/s deposition rates, respectively. The large grain size (or better crystallinity) at lower deposition rates is attributed to the fact that at low deposition rates the molecules have enough time to reach the thermodynamical position

---

(equilibrium). This is also confirmed by the surface morphology of the films shown in Figure 3.2, which shows the AFM images of the thin films evaporated at different deposition rates. It is clearly observed that the film deposited at 0.1 Å/s shows elongated grain structure, whereas the films deposited at 1 Å/s and 5 Å/s show smaller and nearly spherical grain structure, which has also been reported earlier [Singh and Ghosh 2013]. The root mean square (RMS) roughness of the films was estimated as 6.2 nm (0.1 Å/s), 4.5 nm (1 Å/s), and 4.3 nm (5 Å/s).

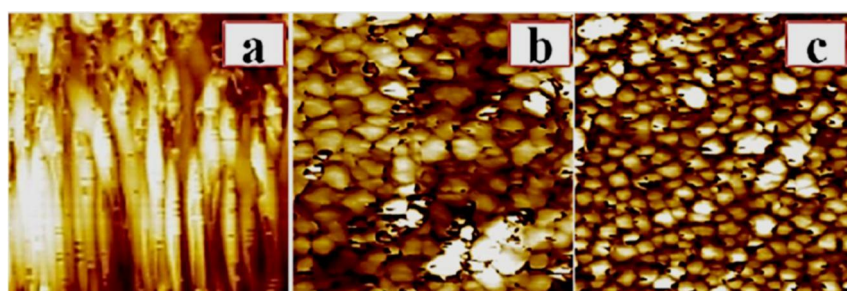


**Figure 3.2** Surface morphology of VOPc films recorded at a scale of  $2\mu\text{m}\times 2\mu\text{m}$  for the deposition rate of (a) 0.1 Å/s; (b) 1 Å/s and (c) 5 Å/s

### 3.2.3 J-V Characteristics

The schematic representation of the fabricated devices is shown in Figure 3.3(a) together with the molecular energy level diagram (Figure 3.3(b)). The values of highest occupied molecular orbital (HOMO) and lowest unoccupied molecular orbital (LUMO) of VOPc, the work function of ITO and Al electrodes have been taken from existing literature [Cai et al. 2009, Jin et al. 2015, Kiran et al. 2015]. The disagreement in the HOMO-LUMO energy level values 2.3–5.3 eV and 6.7–9.7 eV for MoO<sub>3</sub> in the literature are still under debate [Zhao et al. 2008, Kroger et al. 2009]. The sensitivity of UPS and/or other measurements for MoO<sub>3</sub> energy level to surface states, the material purity, the thin film processing and the post-treatment techniques determine the energy levels of MoO<sub>3</sub>. However, there is no discrepancy in the energy gap of approximately 3 eV. In the present work, we have assigned the energy band values as 2.3–5.3 eV as shown in Figure 3.3(b). Insertion of a thin layer of MoO<sub>3</sub> is reported to increase the work function of ITO and Al electrodes [Greiner et al. 2013b]. This helps in achieving an ohmic contact between ITO and VOPc molecules.

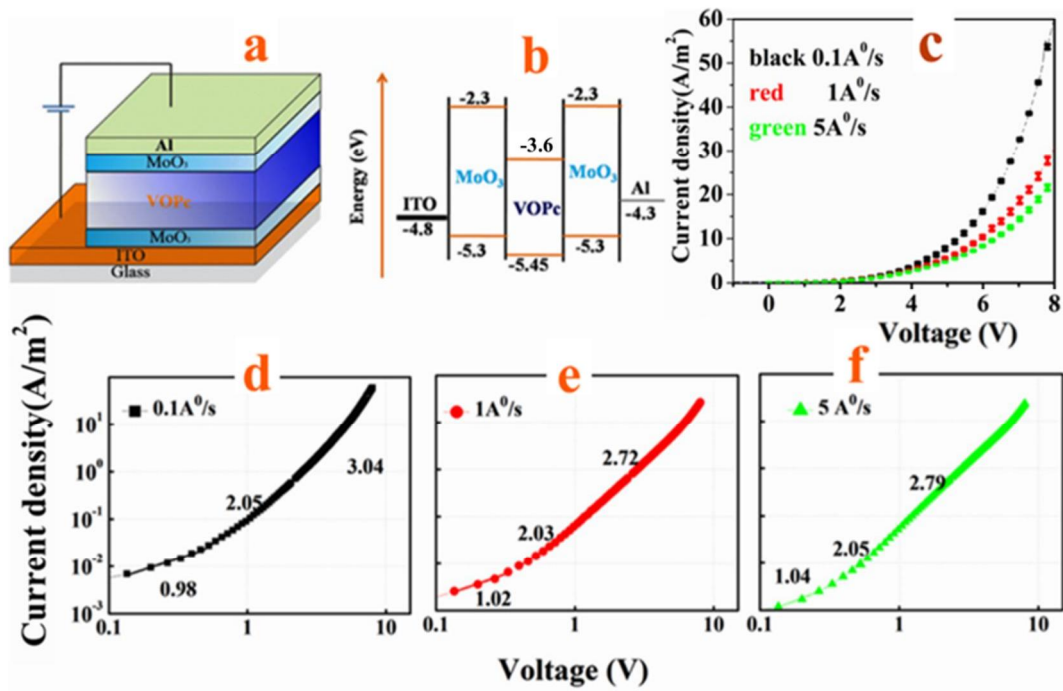


**Figure 3.3(a)** Schematic representation of the VOPc hole only device (error bars included); **(b)** Energy level diagram; **(c)** Forward bias J-V characteristics of all the samples deposited at different deposition rates; **(d-f)** double logarithmic plots for the devices at 0.1 Å/s, 1 Å/s and 5 Å/s.

Figure 3.3(c) shows the forward bias J-V characteristics for the device deposited at different deposition rates. For each deposition rate, four samples have been investigated for J-V characteristics. The results are reproducible within the experimental errors and are presented with the error bars in Figure 3.3(c). The main observation drawn from Figure 3.3(c) is that there is no significant change in the current density in case of devices deposited at 1 Å/s and 5 Å/s. However, there is an improvement of 40 A/cm<sup>2</sup> (at 8 V) in the case of deposition at 0.1 Å/s compared to the devices deposited at higher rates (1 Å/s and 5 Å/s). Figure 3.3(d-f) depicts J-V characteristics of devices deposited at 0.1 Å/s, 1 Å/s and 5 Å/s on log-log scale. Each plot exhibits three different regions. The power law which governs the current density in the three regions is [Shafai and Anthopoulos 2001]

$$J \propto V^\delta \quad (3.1)$$

where  $\delta$  is the slope of the J-V characteristics in different regimes. The first is the ohmic region where  $\delta \sim 1$  ( $V < 0.52$  V for 0.1 Å/s,  $V < 0.33$  for 1 Å/s and  $V < 0.26$  for 5 Å/s). This implies that the electrical conduction in this region is due to the thermally generated charge carriers (excluding traps). Hence, in the ohmic region, the current density of the device is given by [Gould 1996b]

$$J = p_0 e \mu \frac{V}{d} \quad (3.2)$$

where,  $p_0$  is the concentration of thermally generated holes,  $e$  is the electron charge,  $\mu$  is the hole mobility,  $d$  is the thickness of the VOPc layer and  $V$  is the applied bias voltage. In the second regime, the gradient of the current density is  $\delta \sim 2$  ( $0.52 < V < 1.6$  for 0.1 Å/s,  $0.33 < V < 1.0$  for 1 Å/s and  $0.33 < V < 0.6$  for 5 Å/s) indicating that the electrical conduction in this region follows SCLC mechanism given by [Gould 1996b]

$$J = \frac{9}{8} \varepsilon_r \varepsilon_0 \mu \frac{V^2}{d^3} \quad (3.3)$$

where  $\varepsilon_r$  (=3.6) is the dielectric constant of VOPc and  $\varepsilon_0$  is the absolute permittivity. The J-V plots in Figure 3.3(d-f) demonstrate that, as the deposition rate increases, the extent of the SCLC region decreases. This is an indication of the rise in trap density with the deposition rate of VOPc. Further, the third region ( $\delta > 2$ ) represents the trap-charge SCLC, which is governed by [Reis et al. 2004].

$$J = e \mu N_V \left( \frac{\varepsilon_r \varepsilon_0}{e P_0 k_B T_t} \right)^l \frac{V^{l+1}}{d^{2l+1}} \quad (3.4)$$

where  $N_V$  ( $\sim 10^{27} \text{ m}^{-3}$ ) is the effective density of states at the valence band edge (HOMO) [Gould and Rahman 1981, Shafai and Anthopoulos 2001],  $P_0$  is the trap density per unit energy range at the valence band edge (HOMO),  $l = \delta - 1$ ,  $T_t = lT$  is a temperature parameter describing the exponential trap distribution and  $k_B$  is the Boltzmann constant. The total concentration of trap distribution is given by [Gould and Rahman 1981]

$$N_t = P_0 k_B T_t \quad (3.5)$$

The value of  $N_t$  at room temperature can be calculated using the ohmic characteristics (Eq. (3.1)), mobility (Eq. (3.2)) and SCLC characteristics (Eqs.(3.3) and (3.4)). The estimated parameters are presented in Table 3.1.

**Table 3.1** Estimated parameters from J-V characteristics

Rate ( $\text{\AA}/\text{s}$ )	$T_t$ (K) <sup>a</sup>	$p_0$ ( $\text{m}^{-3}$ ) <sup>b</sup>	$P_0$ ( $\text{m}^{-3}$ ) <sup>c</sup>	$N_t$ ( $\text{m}^{-3}$ ) <sup>d</sup>	$\mu_{\text{SCLC}}$ , ( $\text{cm}^2/\text{V}\cdot\text{s}$ ) <sup>e</sup>	$\mu_{\text{IS}}$ , ( $\text{cm}^2/\text{V}\cdot\text{s}$ ) <sup>f</sup>
0.1	613	$1.0 \times 10^{22}$	$0.5 \times 10^{44}$	$4.2 \times 10^{24}$	$2.7 \pm 0.06 \times 10^{-8}$	$1.5 \times 10^{-7}$
1	516	$1.1 \times 10^{22}$	$1.4 \times 10^{44}$	$9.4 \times 10^{24}$	$1.5 \pm 0.18 \times 10^{-8}$	$2.1 \times 10^{-8}$
5	511	$0.8 \times 10^{22}$	$1.2 \times 10^{44}$	$8.1 \times 10^{24}$	$0.9 \pm 0.12 \times 10^{-8}$	$1.1 \times 10^{-8}$

<sup>a</sup> Temperature parameter for exponential trap distribution

<sup>b</sup> Concentration of thermally generated holes

<sup>c</sup> Trap density per unit energy range at the valence band edge

<sup>d</sup> The total concentration of trap distribution

<sup>e</sup> Charge carrier mobility in the SCLC regime

<sup>f</sup> Charge carrier mobility estimated from Impedance measurements.

The results show that there is no significant change in hole concentration for all the devices deposited at different rates. This may be due to the identical injecting contact (ITO/MoO<sub>3</sub>) employed for all the devices to realize ohmic conduction at low bias voltages. However, the calculated values of  $P_0$  and  $N_t$  obtained from high deposition rates (1  $\text{\AA}/\text{s}$  and 5  $\text{\AA}/\text{s}$ ) are twice that of the device deposited at a lower rate (0.1  $\text{\AA}/\text{s}$ ). Also, the estimated mobilities (from trap charge SCLC) of the devices with different deposition rates are almost of the same order as the mobilities obtained from impedance measurements. This high value of trap density may be due to the presence of various intrinsic impurity centers as well as the defects introduced during thin film formation. These defects are common characteristics of organic thin films [Roy et al. 2008]. Since there is no significant change between the device characteristics for 1  $\text{\AA}/\text{s}$  and 5  $\text{\AA}/\text{s}$ , further discussion will be mainly focused on the devices deposited at lower deposition rate (0.1  $\text{\AA}/\text{s}$ ) and at a higher rate (5  $\text{\AA}/\text{s}$ ). The elongated grain

structure in the VOPc films, deposited at lower rates may be the reason for the low concentration of traps and the resulting improvement in the mobility and the current density. Moreover, the electrical conduction in all the devices follows SCLC conduction with an exponential distribution of traps.

### 3.2.4 Device stability

To explore the device stability, a few test devices (deposited at 0.1 Å/s) were examined under ambient conditions. The J-V characteristics were recorded periodically over 4 days. The data is shown in Figure 3.4.

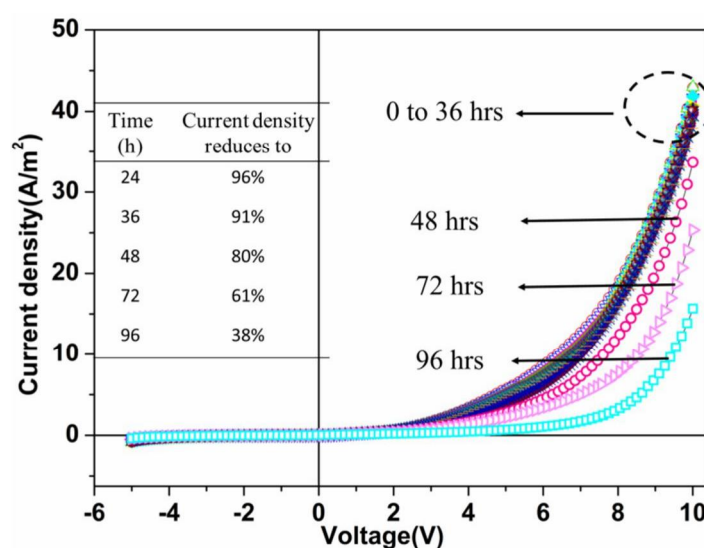


**Figure 3.4** Stability study of VOPc under ambient conditions

From Figure 3.4, it is observed that, for the first 24 h, there is no significant change in the J-V characteristics. Thereafter, the current density decreases rapidly to 80% of its initial value in the next 24 h and to 60% of its initial value after another 24 h (see Table in the inset of Figure 3.4. Similar results were also reported recently [Song et al. 2008, Kim and Yim 2011]. Since the devices remain reasonably stable for the first 24 h, all the measurements were carried out immediately after the fabrication. Devices fabricated at other deposition rates also showed a similar trend as indicated by Figure 3.4.

### 3.2.5 C-V Characteristics

The Capacitance-Voltage (C-V) characteristics as shown in Figure 3.5 were obtained at a frequency of 1 kHz with a fixed ac voltage of 100 mV under dark conditions.

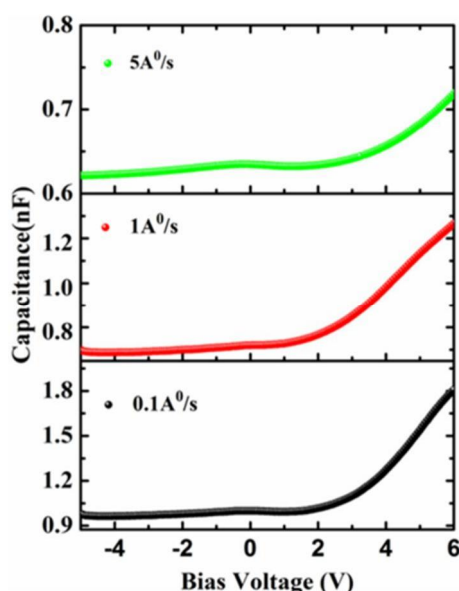


**Figure 3.5** C-V characteristics of the devices at different deposition rate.

Generally, the occurrence of a small capacitance peak in the forward bias characteristics yields a voltage which is numerically equal to the difference in work functions of ITO and Al electrode. In our case, due to the introduction of a thin layer of MoO<sub>3</sub> on either side of the organic, a flat band condition is achieved due to the collapse of depletion layer for MoO<sub>3</sub>/VOPc/MoO<sub>3</sub> structure [Barea et al. 2010, Guerrero et al. 2012]. This may be the reason for the absence of the capacitance peak in our devices (Figure 3.5). As the bias voltage increases, the capacitance of the devices is found to be monotonically increasing beyond 2 V. This increment in the capacitance is due to the contribution from deep traps located in the VOPc bulk. Since the device is hole-only, the traps may capture the injected holes, which leads to the increase in the capacitance [Sharma et al. 2011]. The small decrement in the geometric capacitance of the devices with an increase in deposition rate may be due to the structurally induced defects and/or due to the surface roughness of the organic material [Sharma et al. 2011].

---

### 3.2.6 Impedance Spectroscopy (IS) measurements

IS is a non-destructive characterization tool to study the frequency dependent behaviour of charge transport through the devices. It also yields information about the factors influencing charge transport such as the quality of the deposited electrodes, nature of electrode/semiconductor interface, defect density at the electrode/semiconductor interface, the defect density in the bulk of the semiconductor, charge injection and mobility. In this work, IS measurements were performed to investigate the conduction mechanism operating in the devices fabricated at different deposition rates. The frequency dependent complex impedance of this equivalent circuit is given by [Rouis et al. 2007].

$$Z(f) = Re[Z(f)] + jIm[Z(f)] = R_s + \frac{R_p}{1 + j\omega\tau} \quad (3.6)$$

where,  $\omega = 2\pi f$  is the angular frequency of ac signal,  $\tau$  is the single carrier relaxation time,  $R_s$  is the series resistance of the device which is analogous to the resistance at electrode/organic interface and  $R_p$  is the bulk resistance through the organic semiconductor.

At a given dc bias, the frequency dependence of  $Re[Z]$  of devices with the deposition rate 0.1 Å/s and 5 Å/s are shown in Figure 3.6(a) and (b), respectively. The magnitude of  $Re[Z]$  decreases with the applied bias at low frequencies, whereas, the value of  $Re[Z]$  for all bias voltages merge in the high-frequency region (above 500 kHz). Further, the crossover value of the frequency, where the value of  $Re[Z]$  changes from being frequency independent to being frequency dependent (up to 10 kHz for 0.1 Å/s and 5 kHz for 5 Å/s) shifts to the higher frequency side. This may be attributed to the increase of ac conductivity with applied bias at a higher frequency on account of the release of space charge due to the reduction of barrier height [Suman et al. 2010].

Figure 3.6(c–d) shows the phase versus frequency characteristics of devices with the deposition rates of 0.1 Å/s and 5 Å/s. It can be seen from Figure 3.6(a–b) that the devices show a high impedance of 2 MΩ (for 0.1 Å/s) and 5 MΩ (for 5 Å/s) at a frequency of 100 Hz under 0 V bias conditions. The corresponding phase value of -

80°, as shown in Figure 3.6(c–d), indicates that these devices display a high resistance state (behaves almost as an insulator). At frequencies less than 10 kHz, with the increase in bias voltage, the magnitude of the impedance gradually decreases (Figure 3.6(a–b)) and the corresponding phase gradually reduces from -80 to -10° (at 100 Hz).

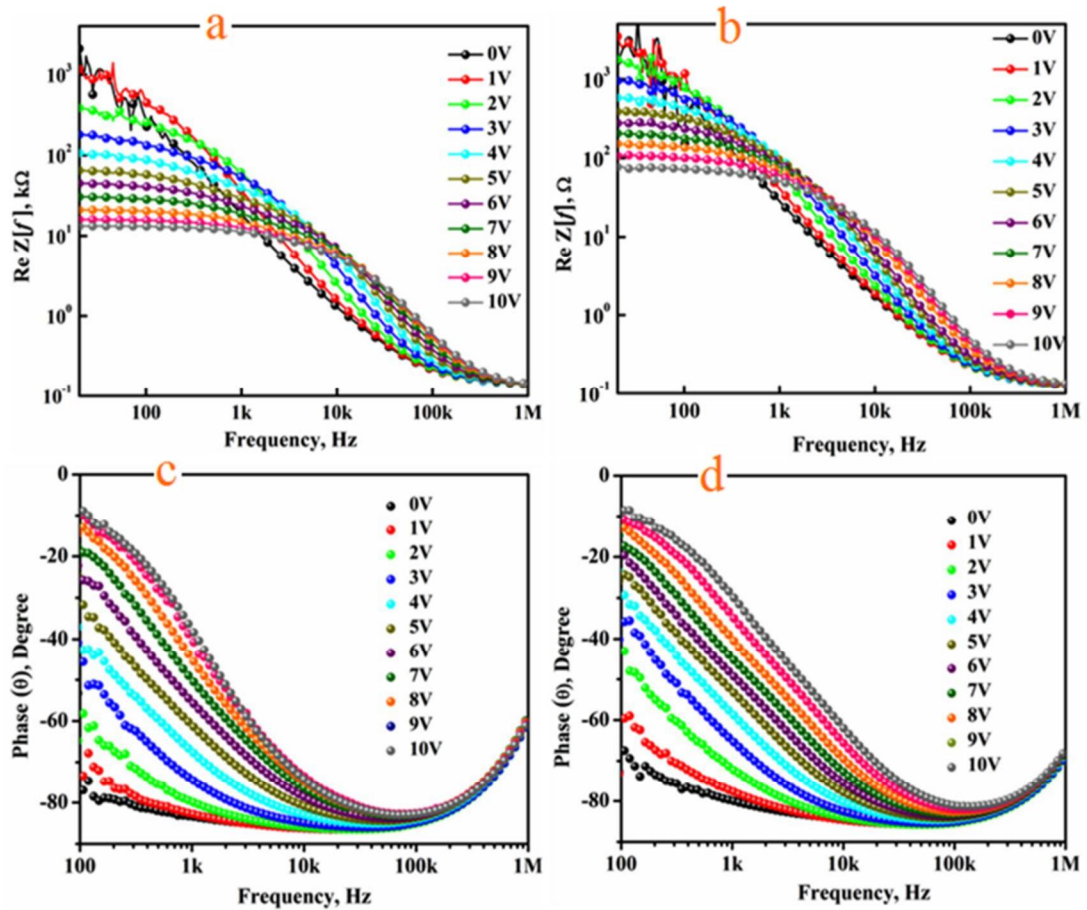


**Figure 3.6(a-b)**  $Re [Z(f)]$ -  $f$  measurements for the devices at 0.1 Å/s and 5 Å/s; **(c-d)** phase-frequency measurements for devices at 0.1 Å/s and 5 Å/s.

The Cole-Cole plots for the devices with the deposition rates of 0.1 Å/s and 5 Å/s are shown in Figure 3.7(a–b). This data can be looked upon as a combination of two semicircles in the range of measurement range. To understand this behaviour, the equivalent circuit is shown in Figure 3.7(e) is adopted. The parallel combination of  $R_b$  &  $C_b$  represents VOPc (bulk), whereas the parallel combination of  $R_i$  &  $C_i$  represents  $MoO_3$  (interface). These two parallel combinations result in two distinct semi-circular Cole-Cole plots, the actual experimental data in Figure 3.7(a, b) is being a combination of these two semicircles. The curves are a fit to the experimental data

obtained by using Eq. (3.7). Figure 3.7(c) shows  $\text{Im}[Z]$  versus frequency plots which show a main ‘peak’ at lower frequencies and a ‘shoulder’ at higher frequencies for various bias voltages. From these plots, one can estimate the relaxation time and, hence, mobility. The frequency at which the ‘peak’ occurs is used to estimate relaxation time at the metal/organic interface. Similarly, the frequency at which the ‘shoulder’ occurs is used to estimate the relaxation time in the bulk VOPc [Reddy et al. 2007].

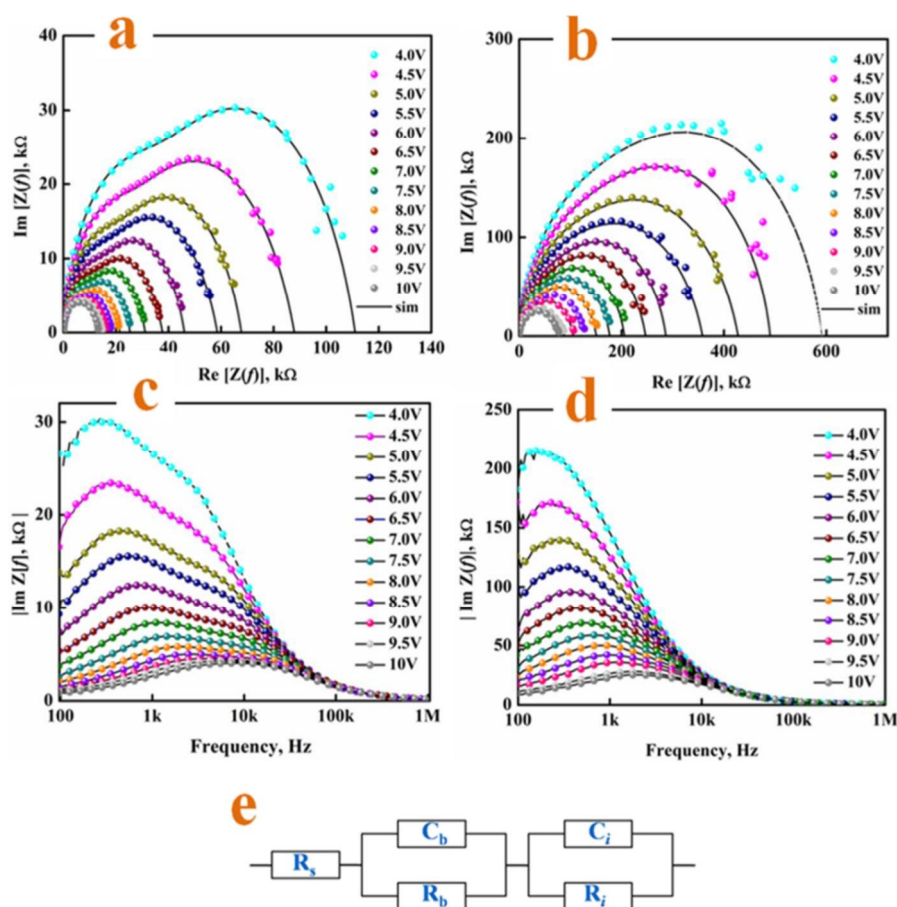


**Figure 3.7**(a) Cole-Cole plot for device deposited at  $0.1 \text{ \AA/s}$ , (b) Cole-Cole plot for device deposited at  $5 \text{ \AA/s}$ , (c) Imaginary impedance-frequency characteristics of device deposited at  $0.1 \text{ \AA/s}$ , (d) Imaginary impedance-frequency characteristics of device deposited at  $5 \text{ \AA/s}$  and (e) the equivalent circuit used for simulation.

As the dc bias increases, the ‘peak’ as well as the ‘shoulder’ shift to higher frequencies. However, their corresponding magnitude progressively reduces. The

Cole-Cole plots, shown in Figure 3.7(a and b), can be modelled by the equivalent circuit shown in Figure 3.7(e) The equation fitting the equivalent circuit is given by [Reddy et al. 2007].

$$Z = R_s + \frac{R_b}{1 + (j\omega R_b C_b)^{Q_b}} + \frac{R_i}{1 + (j\omega R_i C_i)^{Q_i}} \quad (3.7)$$

where the exponent  $Q$  accounts for distribution of relaxation times,  $R_b$  and  $R_i$  are the resistance of VOPc layer and the  $\text{MoO}_3$  interface layer, respectively.  $C_b$  and  $C_i$  are the capacitance of VOPc and  $\text{MoO}_3$  interface, respectively. In the present work, the exponent,  $Q_b$ , for the bulk region, is found to be 1.0 for all the devices and the exponent  $Q_i$  for the interface region is found to be 0.7 (for lower deposition rates) and 0.8 (for higher deposition rates). This indicates that the relaxation process in the bulk region ( $Q_b = 1$ ) may be a Debye type, whereas, the interface has multiple relaxations [Macdonald 1992, Suman et al. 2010]. The values of exponents less than 1.0 indicate a significant dielectric loss due to the dipole-dipole interactions. The relaxation times for the bulk and interface regions are given by  $\tau_b = R_b C_b$  and  $\tau_i = R_i C_i$ , respectively [Reddy et al. 2007]. The series resistance ( $R_s \sim 50 \Omega$ ) estimated from the equivalent circuit model (Figure 3.7(e)) is almost constant for all the bias voltages. This usually arises due to contact resistance of the metal electrode (ITO/ $\text{MoO}_3$ ).

Figure 3.8(a) shows the variation of the resistance of both the devices (0.1  $\text{\AA}/\text{s}$  and 5  $\text{\AA}/\text{s}$ ) in bulk and in the interface region. For both devices, the resistance of the interface region is 5 times greater than that of the bulk. Besides that, the device deposited at a higher rate (5  $\text{\AA}/\text{s}$ ) shows 5 times higher bulk resistance than the devices at a lower rate (0.1  $\text{\AA}/\text{s}$ ). According to the SCLC model (with an exponential distribution of traps), the charge carriers move through the bulk of the organic material by hopping from trap to trap. The high resistance of the interface region indicated that there are enough number of traps to be filled with the injected charges leading to SCLC behaviour. This means that the interface region has a higher density of traps than the bulk region. It also conveys that the devices deposited at higher rates have a high density of traps than the devices at a lower deposition rate. This agrees well with the estimated traps densities from the steady-state dc J-V characteristics,

wherein, the trap density is 2 times higher for the devices deposited at a higher rate (5 Å/s).

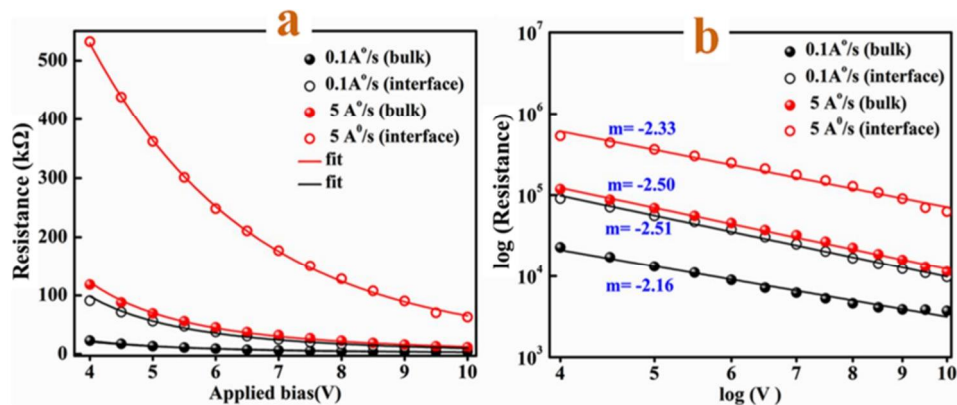


**Figure 3.8(a)** Variation of resistance with applied bias in bulk and at the interface and **(b)** log-log plot of resistance variation with applied bias.

The bulk capacitances of the devices 1.9nF (0.1 Å/s) and 1.7nF (5 Å/s), estimated from the equivalent model, are independent of the applied bias. This suggests that the applied bias does not lead to any change in the molecular structure of VOPc. On the other hand, the resistance of the bulk region varies exponentially with the applied voltage. According to the SCLC theory, the voltage-dependent resistance  $R_b$  for a single type carrier (hole) transport is given by the equation

$$R_b \propto V^{-m} \quad (3.8)$$

For ideal trap free SCLC condition, the value of exponent  $m$  should be approximately 1. However, the value of  $m$  deviates from 1 in the presence of traps [Chung et al. 2008, Anjaneyulu et al. 2011, Braik et al. 2015, Rasool et al. 2015]. In the present work, the  $m$  values of 2.33 (0.1 Å/s, bulk region), 2.50 (0.1 Å/s, interface region), 2.51 (5 Å/s, bulk region) and 2.16 (5 Å/s, interface region) obtained from Figure 3.8(b) are in good agreement with the slopes obtained from J-V characteristics (Figure 3.3(d-f)). This suggests that the electrical conduction in these devices follows the SCLC mechanism with an exponential distribution of traps. Similar results (slope ~2.2) are also observed in the device deposited at 1.0 Å/s suggesting similar conduction mechanism.

### 3.2.7 Estimation of mobility using Impedance technique

The charge carrier mobility ( $\mu$ ) of the organic semiconductor is given by [Tripathi et al. 2011a].

$$\mu = \frac{d^2}{\tau_{dc} V_{dc}} \quad (3.9)$$

where  $d$  is the thickness of the organic layer ( $d_{VOPc} = 100$  nm),  $V_{dc}$  is the applied dc bias and  $\tau_{dc} (= \kappa \tau_r)$  is the charge carrier relaxation time. The numerical value of  $\kappa$  can be obtained from the computer simulations using Matlab similar to the work carried out by Tripathi et al. [Tripathi et al. 2011]. The following two equations are used to carry out simulations for frequency dependent imaginary impedance.

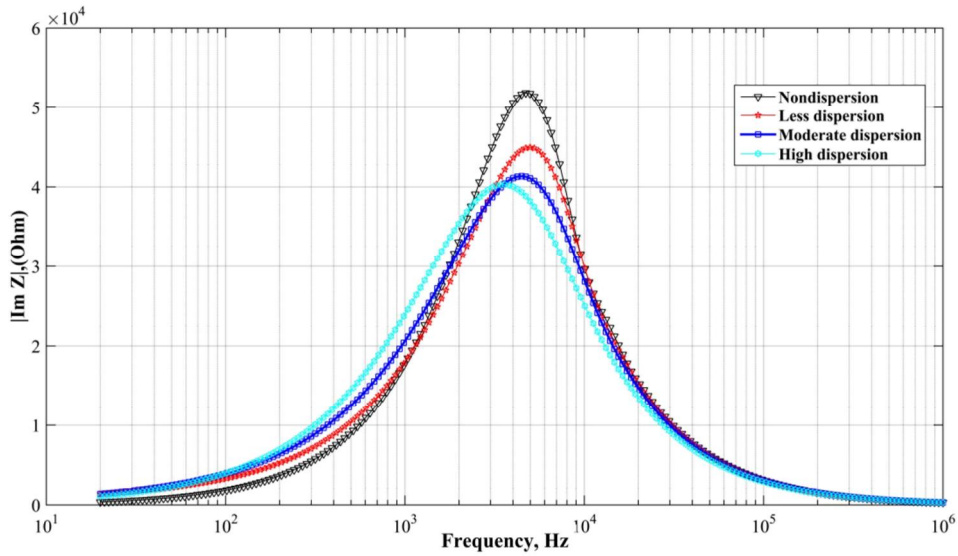


**Figure 3.9** Simulation of frequency dependent Im  $Z$  for the different degree of dispersion Here,  $\epsilon_r = 3.6$  for VOPc films,  $\tau_{dc} = 1 \times 10^{-4}$  s, device area  $A = 0.016$  cm<sup>2</sup> and thickness  $d = 100$  nm.

If organic material is trap-free, with a dielectric constant  $\epsilon$ , then the complex Impedance  $Z(\Omega)$  can be written in the form [Martens et al. 1999, 2000, Tsang et al. 2006b, 2006a]

$$Z(\Omega) = \frac{\tau_{dc} d}{\epsilon A} \times \left( \frac{2i[0.75\bar{\mu}(\Omega)]^2 \{1 - \exp[-4i\Omega/3\bar{\mu}(\Omega)]\} + 1.5\bar{\mu}(\Omega)\Omega - i\Omega^2}{\Omega^3} \right) \quad (3.10)$$

where the normalized frequency is  $\Omega = 2\pi f\tau_{dc} = \omega\tau_{dc}$ ,  $\omega$  is the angular frequency,  $\tau_{dc}$  is the dc transit time. The normalized mobility is given by [Martens et al. 1999, 2000, Tsang et al. 2006b, 2006a]

$$\tilde{\mu}(\Omega) = \frac{\mu(\Omega)}{\mu_{dc}} = 1 + M(i\Omega)^{1-\alpha} \quad (3.11)$$

where  $M$  and  $\alpha$  are the dispersion parameters,  $\mu_{dc}$  is the dc mobility and  $\tau_{dc}$  is the average carrier transit time. The simulations for frequency dependent imaginary part of the impedance were carried out for the different dispersions (presented in Figure 3.9) and the corresponding  $\kappa$  values are presented in Table 3.2.

**Table 3.2**  $\tau_{dc}$  to  $\tau_r$  ratio as obtained using Im Z method

Degree of dispersion	$\kappa = \tau_{dc}/\tau_r$
Non dispersion $M=0, \alpha=1$	0.47
Less dispersion $M=0.1, \alpha=0.7$	0.49
Moderate dispersion $M=0.15, \alpha=0.5$	0.45
High dispersion $M=0.2, \alpha=0.3$	0.36

From Table 3.2, the mean value of  $\kappa$  along with the dispersion is found to be 0.44. The Poole-Frenkel field dependent mobility is given by

$$\mu(E) = \mu_0 \exp(\beta\sqrt{E}) \quad (3.12)$$

where  $E = V/d$  is the applied electric field at voltage  $V$ . The field independent mobility ( $\mu_0$ ) (also called as Zero-field mobility) and the Poole-Frenkel (PF) coefficient ( $\beta$ ) are obtained from the intercept and slope of the linear fit to the above equation (in Figure 3.10), respectively.

The field dependent charge carrier mobilities of all the devices are presented in Figure 3.10. The zero-field charge carrier mobility values  $1.5 \times 10^{-7} \text{cm}^2/\text{V-s}$  (for 0.1 Å/s),  $2.1 \times 10^{-8} \text{cm}^2/\text{V-s}$  (for 1 Å/s) and  $1.1 \times 10^{-8} \text{cm}^2/\text{V-s}$  (for 5 Å/s) are consistent with the values obtained using the dc J-V measurements. This is also consistent with the available literature ( $1.59 \times 10^{-9} \text{cm}^2/\text{V-s}$  for CuPc [Shah et al.2011] and  $6.35 \times 10^{-6} \text{cm}^2/\text{V-s}$  for ZnPc [Murtaza et al. 2011]). Further, the charge carrier mobility of the

devices are found to be  $5.7 \times 10^{-10} \text{ cm}^2/\text{V}\cdot\text{s}$  (for  $1 \text{ \AA}/\text{s}$ ) and it is two orders less than that of devices with  $\text{MoO}_3$  as a hole injection layer. This can be attributed to the fact that the  $\text{ITO}/\text{MoO}_3$  facilitate better hole injection by lowering the barrier height between  $\text{ITO}$  and  $\text{VOPc}$ . The total charge transport is due to the transport through the grains in addition to the transport across the grain boundaries. Thus, the reason for high mobility in the device deposited at  $0.1 \text{ \AA}/\text{s}$  compared to  $1 \text{ \AA}/\text{s}$  and  $5 \text{ \AA}/\text{s}$  can be attributed to the elongated grain structure wherein the grain boundary effect is lesser compared to the devices fabricated at higher deposition rates

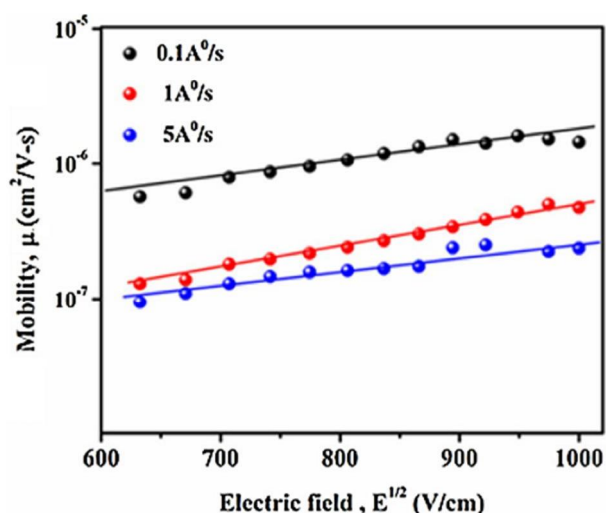


**Figure 3.10** Field dependent hole mobility of VOPc film with different deposition rates

### 3.2.8 AC conductivity

The conductivity–frequency characteristics at different bias for all the devices are shown in Figure 3.11(a). Since ac conductivity graphs for devices with higher deposition rates also follow a similar pattern as those deposited at lower rates, Figure 3.11(a) shows only the data corresponding to the deposition rate of  $0.1 \text{ \AA}/\text{s}$ . Figure 3.11(a) displays the plots of  $\ln(\sigma)$  versus  $\ln(\omega)$  at room temperature for various bias voltages. As seen from Figure 3.11(a),  $\ln(\sigma)$  is practically constant at very low frequencies and saturates to almost a constant value at very high frequencies. In between these two extremes  $\ln(\sigma)$  increases almost linearly with increasing frequency. It is also seen that the onset of the linear increase in the graph progressively shifts to

higher frequencies as bias increases. From these observations, we conclude that the dominant charge transport is hopping type.

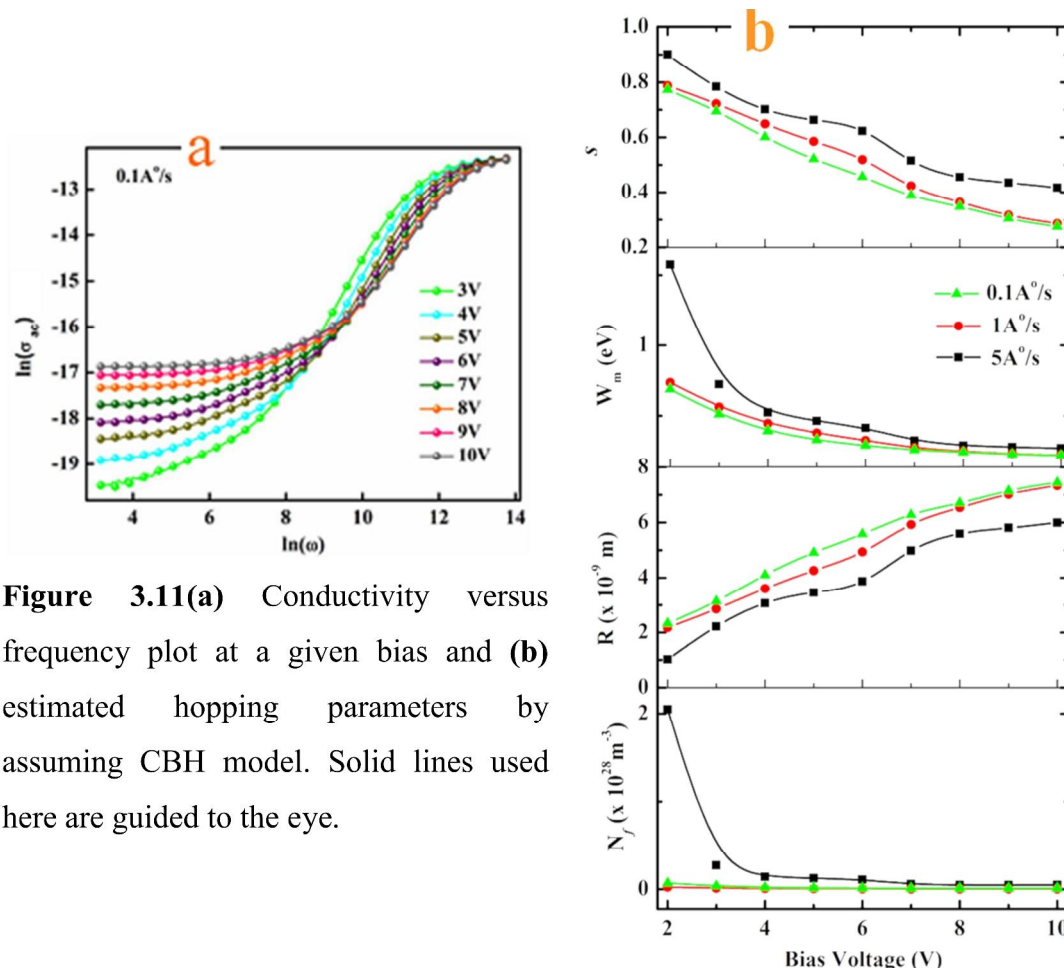


**Figure 3.11(a)** Conductivity versus frequency plot at a given bias and **(b)** estimated hopping parameters by assuming CBH model. Solid lines used here are guided to the eye.

The power law which governs the frequency dependent ac conductivity is given by [Ghosh and Pan 2000, Suman et al. 2009]

$$\sigma_{\text{tot}}(\omega) = \sigma_{\text{dc}} + C\omega^s \quad (3.13)$$

where,  $\sigma_{\text{dc}}$  is the frequency independent conductivity (observed at lower frequencies),  $\omega$  is the angular frequency of the applied ac signal in the frequency range 100 Hz to 1 MHz, the constant  $C$  represents the strength of the polarizability and the frequency exponent  $s$  represents the degree of interaction between the mobile charge carriers and their surroundings. The slope of the linear portion of the graph gives the value of  $s$ . In general, the decrease in conductivity ( $\sigma$ ) with the increase in signal frequency is indicative of band type conduction process. On the other hand, the increase in

---

conductivity with frequency is associated with a hopping type conduction process [Elliott 1977, Anthopoulos and Shafai 2003].

Our studies from Figure 3.11(b) indicate that, the value of ‘s’ decreases from 0.9 to 0.3 as the applied bias voltage is increased from 2 V to 10 V. Thus, the dispersion in the value of ‘s’ could arise due to variation in signal frequency as well as bias voltage, which is an indicative of charge transport by CBH process (Temperature dependencies explained in Appendix ) [Suman et al. 2009, Murtaza et al. 2011b, Ramar et al. 2015]. In this model, hopping of carriers (holes) is most likely to occur between the two equivalent adjacent localized states [Abu-Hilal et al. 2005].

The ac conductivity of the CBH mechanism is given by [Suman et al. 2009, Mansour et al. 2015].

$$\sigma_{ac} = \frac{\pi^3}{24} N_f^2 \epsilon_0 \epsilon_r \omega R^6 \quad (3.14)$$

where 
$$R = \frac{e^2}{\pi \epsilon_0 \epsilon_r W_m} \quad (3.15)$$

and 
$$W_m = \frac{6k_B T}{1 - s} \quad (3.16)$$

where  $N_f$  is a pair of localized density of states at the Fermi level,  $W_m$  is the binding energy (the energy required for a charge carrier to move from one site to another),  $R$  is the minimum hopping length,  $k_B$  is the Boltzmann constant and  $T$  is the absolute temperature. Figure 3.11(b) shows the calculated binding energy  $W_m$ , minimum hopping distance  $R$  and the density of states  $N_f$  for all the devices deposited at different deposition rates. It is clear that the exponents for all the devices decrease with the increase in applied bias. The binding energy and the density of states decrease marginally with increasing bias voltage above 4.0 V for all the devices. Below 4.0 V, both  $W_m$  and  $N_f$  increase sharply. Also, at low deposition rates, the value of  $N_f$  is significantly lower which leads to an increase in conductivity in the devices fabricated at the low deposition rates.

---

### 3.3 CONCLUSION

In this chapter, three devices were fabricated in a hole only configuration: ITO/MoO<sub>3</sub>/VOPC/MoO<sub>3</sub>/Al by varying the deposition rate of the active layer (VOPc). The improvement in the current density and the mobility of the device at a low deposition rate (0.1 Å/s) is attributed to the elongated grains, high carrier density and high mobility. It is also found that the electrical conduction follows SCLC mechanism with an exponential distribution of traps within the band gap and it was found that the estimated trap density ( $8.1 \times 10^{24} \text{m}^{-3}$ ) of the devices at higher deposition rate was twice the that of the device fabricated at lower deposition rates. The hole mobility values were obtained from IS measurements and the higher hole mobility of  $1.5 \times 10^{-7} \text{cm}^2/\text{V-s}$  was achieved in the VOPc film with 0.1 Å/s when compared to the films at higher deposition rates. The experiments show that the dominant charge transport mechanism is of hopping type and follows the CBH model. It is also seen that the charge transport does not depend on the deposition rate. In addition, there is an improvement in the current density, charge carrier mobility and localized density of states for devices fabricated at low deposition rates (0.1 Å/s) and hence shows better performance.

---

## CHAPTER 4

### ELECTRICAL CHARGE TRANSPORT IN ELECTRON ONLY DEVICES MADE USING ZINC OXIDE THIN FILMS

#### *Overview*

*Chapter 4 explores the electron transport properties of the devices based on Zinc oxide (ZnO) in the electron only device configuration: ITO/ZnO/Al. For this study, the ZnO thin films were fabricated using sol-gel spin coating technique and the annealing temperatures were varied from 150°C to 450°C in steps of 100 °C. The structural, morphological, optical and electrical properties were also studied for different annealing temperatures. The parameters related to ITO/ZnO interface, such as ideality factor, barrier height, and rectification ratio of the diode, were determined using current density-voltage (J-V) characteristics. The results clearly demonstrate that ZnO film annealed at 350°C exhibits much better optoelectronic characteristics on account of increased grain size, improved charge injection due to the reduction of barrier height and hence higher (up to 5 orders) charge carrier mobility.*

#### **4.1 INTRODUCTION**

Zinc oxide (ZnO) is a strong contender for future optoelectronics applications that include transparent conductors, solar cells, varistors, liquid crystal displays, gas sensors and photodetectors [Brückner et al. 1980, Levinson et al. 1982, Carotta et al. 2009, Lee et al. 2010, Kidowaki et al. 2012, Yuan 2014]. ZnO is a direct wide-band-gap ( $E_g = 3.27$  eV) semiconductor (n-type) with high exciton binding energy of 60 meV. Apart from the planar interfaces with ZnO films, various nanostructures of ZnO (particles, rods, tubes, wires, belts, etc.) have been explored due to their potential applications in various miniaturized devices; such devices include sensors, thin film transistors (TFT), light emitting diodes (LEDs), photodetectors and solar cells. Due to the ease of synthesis, high surface area and superior optoelectronic properties, ZnO nanoparticles have been widely exploited.

---

To gain insight into the use of ZnO in organic-inorganic hybrid structures, one needs to explore the electrical properties of ZnO thin films in sandwich structures. The properties of sandwich structures can be correlated with the properties of actual thin film devices. In this chapter, the effects of annealing temperature on the charge transport properties of ITO/ZnO/Al electron-only devices are presented. These investigations were carried out with the motivation of understanding the charge carrier dynamics at ITO/ZnO interface and its effect on the charge transport.

## 4.2 FABRICATION AND CHARACTERIZATION OF THE DEVICES

### 4.2.1 Preparation of ZnO thin films and fabrication of electron-only devices

The schematic of the proposed devices is shown in Figure 4.1.

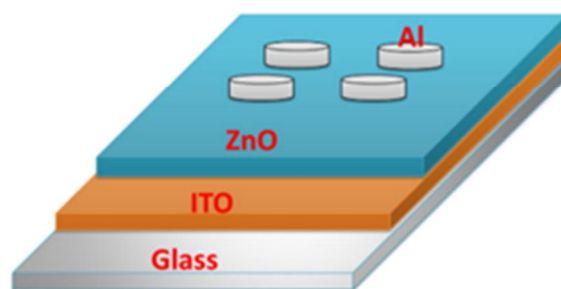


**Figure 4.1** Schematic of the electron-only device

ZnO nanoparticulate thin films were prepared by sol-gel spin coating technique similar to the method used in our previous study [Kiran et al. 2015a]. The precursor was prepared by dissolving 4g of zinc acetate dehydrate [ $\text{Zn}(\text{CH}_3\text{COO})_2 \cdot 2\text{H}_2\text{O}$ ] in 50 ml of 2-methoxy ethanol. This colloidal solution was stirred for 1h on the pre-heated hot plate ( $70^\circ\text{C}$ ), and 1.2 ml of monoethanolamine (MEA; acts as a stabilizer) was added drop-wise for about 10 min and the mixture was stirred for about 2h. The resulting clear solution was aged (48 h) at room temperature to form a gel. The aged sol-gel was spin coated on pre-cleaned and UV-Ozone treated (15 minutes) pre-patterned ITO coated glass substrates at a spin rate of 500 rpm for the first 30s and at 1000 rpm for next 30s. The deposited film was baked at  $120^\circ\text{C}$  for 10 min. The deposition process is repeated three times to achieve the desired film thickness. These films were further annealed in air at either  $150^\circ\text{C}$ ,  $250^\circ\text{C}$ ,  $350^\circ\text{C}$  or

450°C for about 1 hour. The thickness of the films measured by spectral reflectometry was about 200±10 nm.

For the fabrication of single layer devices, a 100 nm thick aluminium (Al) electrode layer was thermally evaporated on the pre-coated (and annealed) ZnO at the rate of 5-6 Å/s using a shadow mask.

#### 4.2.2 Structural and morphological properties

ZnO films, prepared on glass substrates, were annealed at different temperatures. Their XRD patterns are shown in Figure 4.2. The XRD analysis confirmed that the samples crystallized in hexagonal wurtzite structure [JCPDS 36-1451]. As the annealing temperature was increased, the XRD peaks became sharper, indicating better crystallinity of the synthesized samples. The predominant XRD peaks at  $2\theta = 31^\circ, 34^\circ, 36^\circ$  and  $54^\circ$  were assigned to (110), (002), (101) and (110) planes. The estimated nanoparticles/grain sizes in the thin films, calculated from Scherrer's formula (Eq.2.1) are presented in Table 4.1.

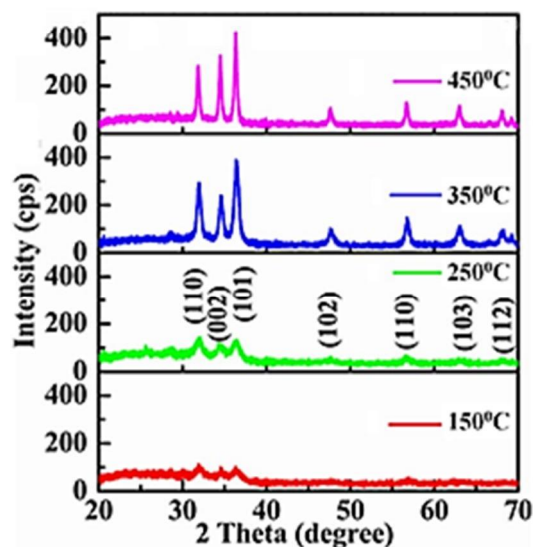


**Figure 4.2** X-ray diffraction patterns of ZnO nanoparticulate thin films on a glass substrate for different annealing temperatures.

The SEM images of the ZnO films annealed at different temperatures are shown in Figure 4.3. It can be clearly seen that the ZnO nanoparticles (grain) size

increased with the increase in annealing temperatures. The particles sizes obtained from these SEM images agree well with the values estimated from XRD spectra.

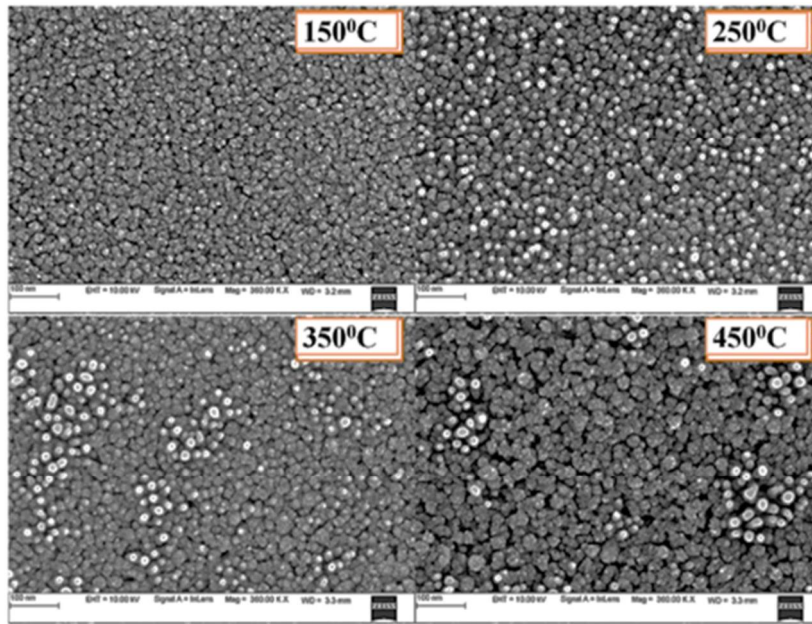


**Figure 4.3** SEM images on 100 nm scale, of ZnO films on glass annealed at different temperatures

#### 4.2.3 Optical Transmission spectra

A large number of applications on ZnO are based on its remarkable optical properties. The optical transmission spectra of ZnO thin films, annealed at different temperatures, are shown in Figure 4.4(a). The average transmission of all the films is seen to be 85% to 95% in the visible optical region. A sharp spike seen at around 650 nm in the transmission spectra for all the thin film samples was confirmed to be a spectral line emitted by the Deuterium source used for the measurement and does not originate from the ZnO films. The optical band gap of the films at different annealing temperatures was estimated from the fundamental absorption edge by considering direct allowed transitions. For the direct transitions, the absorption coefficient can be written as

$$\alpha h\nu = A(h\nu - E_g)^{1/2} \quad (4.1)$$

where,  $A$  is the constant,  $E_g$  is the optical band gap,  $\nu$  is the frequency of the incident radiation and  $h$  is the Planck's constant. Figure 4.4 (b) shows the plot of  $(\alpha h\nu)^2$  versus  $E_g$  for the ZnO thin films annealed at different temperatures. The presence of a single slope in the plot suggested that the films had direct and allowed transition (direct band gap). The band gap energy was obtained by extrapolating the straight line portion of the plot to zero absorption coefficient. The optical band gap values are seen to reduce from 3.35eV to 3.28eV as the annealing temperature increased from 150°C to 350°C. This can be attributed to improved crystalline nature of ZnO thin films, that resulted in reduced traps by extended localized states in conduction band and valence band [Mathew et al. 2012].

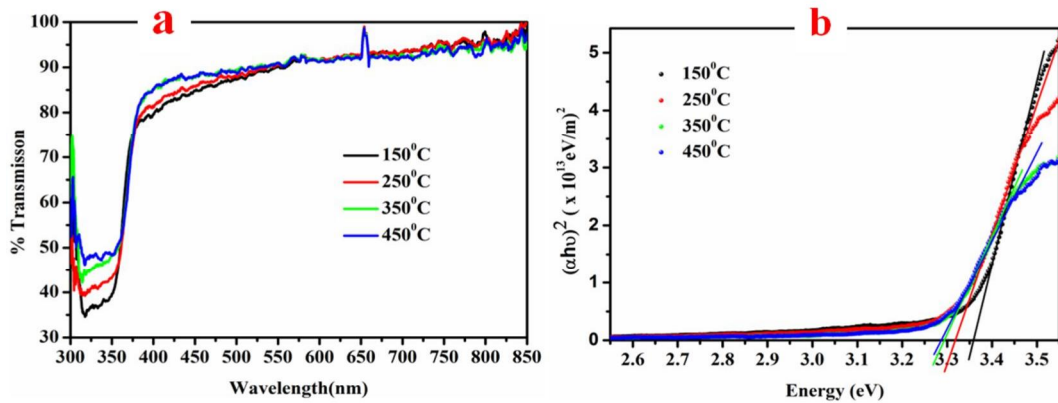


**Figure 4.4(a)** Optical transmittance spectra of ZnO at different annealing temperatures and **(b)** Tauc's plots to estimate the band gap of ZnO at different annealing temperatures.

#### 4.2.4 J-V Characteristics

Figure 4.5(a) shows energy level diagram of the proposed devices with ZnO as an active layer. The valence band (VB)-conduction band (CB) energy levels of ZnO and the work function of ITO and Al have been taken from the literature [Zhao et al. 2008, Yoon et al. 2012, Alam Khan and Farva 2017]. The energy difference ( $\Delta E_{FC}$ ) between the work function of ITO and the CB of ZnO is less compared to the energy difference ( $\Delta E_{FV}$ ) between the work function of ITO and the VB of ZnO. Hence, it is concluded that electron injection dominates at the ITO/ZnO junction.

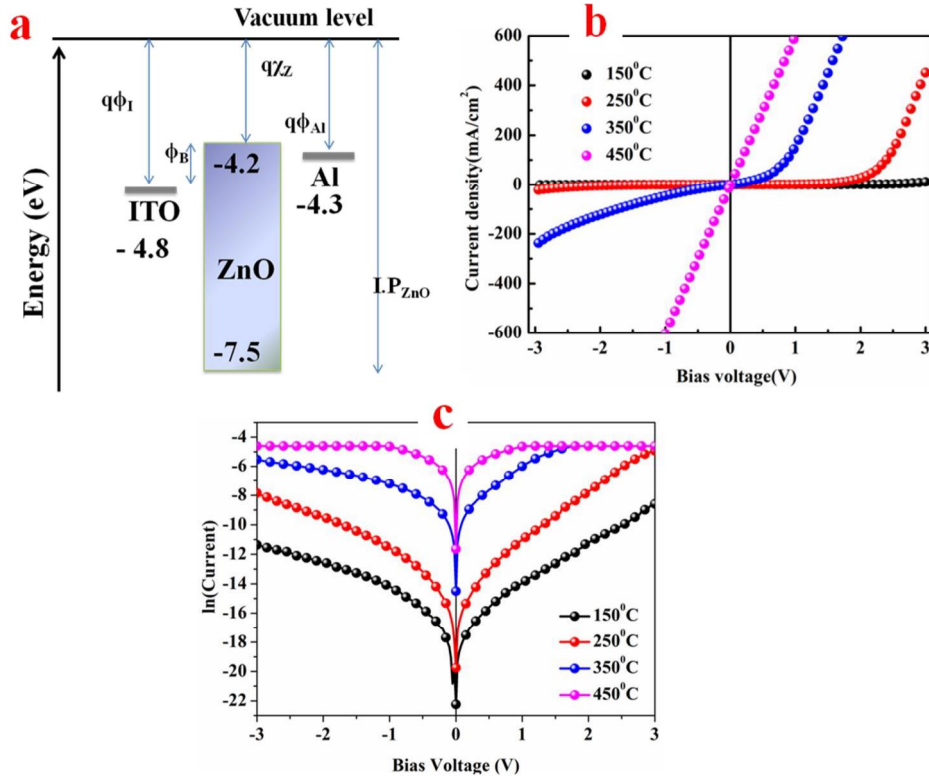


**Figure 4.5(a)** Energy level representation of the electron only devices with ITO/ZnO/Al configuration. Here,  $q\phi_I$ ,  $q\phi_{Al}$  and  $q\chi_z$  represent the work functions of ITO, Al and the electron affinity of ZnO, respectively.  $IP_{ZnO}$  is the ionization potential of ZnO; **(b)** J-V characteristics of the single layer devices at different annealing temperatures; **(c)**  $\ln(I)$ -V characteristics of the single layer devices.

The room temperature J-V characteristics of the devices fabricated using ZnO films annealed at different temperatures are shown in Figure 4.5(b). Clearly, the devices annealed at 150°C, 250°C and 350°C showed rectification behaviour and the corresponding rectification ratios (RR) of the three devices, at a bias voltage of 1.5V, were found to be 1.89, 2.77 and 5.53, respectively. It was also found that the device with ZnO film annealed at a temperature of 450°C did not show any rectification. The characteristic diode equation under forward bias greater than a few millivolts is given by [Yuan et al. 2012, Kiran et al. 2015b]

$$I = I_0 \exp\left(\frac{V}{nV_t}\right) \quad (4.2)$$

where  $V_t$  is the thermal energy at 300K (~26 meV),  $V$  is the applied bias,  $n$  is the diode ideality factor.  $I_0$  is the reverse saturation current which can be expressed as [Gupta et al. 2011]

$$I_0 = AA^*T^2 \exp\left(\frac{q\phi_B}{k_B T}\right) \quad (4.3)$$

Here,  $A$  is the area of the device ( $1.6 \times 10^{-2} \text{ cm}^2$ ),  $A^*$  is the effective Richardson's constant ( $1.3 \times 10^5 \text{ Am}^{-2} \text{ K}^{-2}$  for ITO contact) [Kiran et al. 2015c],  $(q\phi_B)$  is the barrier height in eV,  $k_B$  is the Boltzmann constant and  $T$  is the absolute temperature in K.

**Table 4.1** Estimated parameters for the ZnO films annealed at different deposition rates

Annealing temperature	Grain size (nm)		$n^a$	$I_0^b$ (amp)	$\phi_B^c$ (meV)	R.R @1.5V	$\mu^d$ ( $\text{cm}^2/\text{V-s}$ )	$N(E_F)^e$ ( $\text{eV}^{-1} \text{cm}^{-3}$ )	$N_A^f$ ( $\text{cm}^{-3}$ )	$V_{bi}^g$ (V)
	XRD	SEM								
150°C	8	11	7.2	$1.2 \times 10^{-8}$	550	1.89	$3.22 \times 10^{-10}$	$3.2 \times 10^{17}$	$8.0 \times 10^{17}$	3.6
250°C	11	15	6.7	$9.0 \times 10^{-8}$	497	2.77	$4.19 \times 10^{-8}$	$4.2 \times 10^{17}$	$1.3 \times 10^{18}$	0.75
350°C	16	17	8.4	$4.9 \times 10^{-5}$	333	5.53	$4.16 \times 10^{-5}$	$5.4 \times 10^{17}$	$2.1 \times 10^{19}$	0.25
450°C	25	21	-	-	-	--	-	-	-	-

<sup>a</sup> diode ideality factor

<sup>e</sup> Density of states at Fermi level

<sup>b</sup> reverse saturation current

<sup>f</sup> charge carrier density

<sup>c</sup> interfacial barrier height

<sup>g</sup> built-in voltage

<sup>d</sup> charge carrier mobility

The diode ideality factors and the reverse saturation currents of the devices with different ZnO annealing temperatures were obtained from  $\ln I-V$  plots as shown in Figure 4.5(c). The slope and intercept of the graphs in the linear region (0.1 to 0.8V) yielded the values of  $n$  and  $I_0$ , respectively. From Table 4.1, it is observed that the reverse saturation current increased by about three orders of magnitude, whereas

---

the Schottky barrier height ( $q\phi_B$ ) reduced from 550 meV to 330 meV as the annealing temperature of the ZnO increased from 150°C to 350°C. However, the high value of ideality factors ( $>1$ ) is observed for all the devices prepared at different annealing temperatures, implying that the current conduction mechanism does not follow the thermionic emission conduction mechanism alone and that it depends on the various charge transport mechanisms. This suggests that the interface is not an ideal metal/semiconductor contact and that there must be some trapping states present at the interface, which can act as localized carrier generation-recombination centers [Dey et al. 2015]. A similar set of experiments were conducted multiple times for each annealing temperature. All the results are reproducible within experimental errors. The best values obtained, at a given annealing temperature, are presented in this study.

In general, the potential barrier height ( $q\phi_B$ ) is related to the work function ( $q\phi_M$ ) of the metal and electron affinity of the semiconductor ( $q\chi$ ) of the semiconductor ( $q\phi_B \approx (q\phi_M - q\chi)$ ) (Figure 4.5(a)). Here we observed that the potential barrier height for the electron only devices reduced with increasing annealing temperatures. This may be ascribed to the dissimilarity in electron affinity of semiconductor nanoparticles depending upon their band structure and band gap energy [Middy et al. 2014]. Similar behaviour has also been observed in earlier reports based on Kelvin probe and XPS measurements for sol-gel ZnO thin films [Sun et al. 2011, Dearden et al. 2014, Sharma et al. 2014]. In this study, we had employed Impedance spectroscopy technique (IS) to investigate the behaviour of our devices and to estimate the electron mobilities.

For SCLC conduction mechanism with exponential trap distribution (also confirmed from IS measurements), the density of states (DOS) at the Fermi level is estimated using the following equation [Şahin et al. 2006]

$$N(E_F) = \frac{2\varepsilon_r\varepsilon_0\Delta V}{ed^2\Delta E_F} \quad (4.4)$$

where  $\varepsilon_r$  is the dielectric constant of the ZnO film (8.5) [Efafi et al. 2014],  $\varepsilon_0$  is the permittivity of free space,  $e$  is the electron charge,  $d$  is the thickness of the ZnO layer,

$\Delta E_F$  is the shift in the quasi-Fermi level and  $\Delta V = V_1 \sim V_2$ ,  $V_1$  and  $V_2$  being two different voltages applied to the device. When the applied potential is increased from  $V_1$  to  $V_2$  (extremes of SCLC region), the quasi-Fermi level shift is given by the equation,

$$\Delta E_F = k_B T \ln \left( \frac{I_2 V_1}{I_1 V_2} \right) \quad 4.5$$

where  $k_B$  is the Boltzmann constant,  $T$  is the absolute temperature and  $I_1, I_2$  are current values measured at the voltages  $V_1$  and  $V_2$  respectively. From Table 4.1, it is noted that there is no significant change in the estimated values of effective DOS around the Fermi level which indicated that the trap density at the interface was same for all the samples. The observed values of the effective DOS at the Fermi level for all the devices ( $10^{17} \text{ eV}^{-1} \text{ cm}^{-3}$ ) are comparable with values reported earlier [Dey et al. 2015].

#### 4.2.5 C-V Characteristics

The Mott-Schottky plots ( $1/C^2$  versus  $V$ ) for the devices made at different ZnO annealing temperature are shown in Figure 4.6. These characteristics were obtained at a fixed frequency of 1 kHz with ac amplitude of 500mV. Extrapolating the linear portion of the Mott-Schottky plots to the x-axis (where  $1/C^2 = 0$ ) yielded the built-in voltage  $V_{bi}$ . According to the standard Mott-Schottky equation, the dependence of capacitance on the applied bias is given by [Singh and Ghosh 2015].

$$\frac{1}{C^2} = \frac{2(V_{bi} - V)}{A^2 e \epsilon_0 \epsilon_r N_A} \quad (4.6)$$

where  $V_{bi}$  is the built-in voltage,  $A$  is the area of the interface in device,  $e$  is the electron charge,  $\epsilon_r$  is the dielectric constant of ZnO,  $\epsilon_0$  is the absolute permittivity and  $N_A$  is the effective charge carrier concentration of the conduction charge carriers. The estimated carrier concentration and the corresponding  $V_{bi}$  values for the devices made at different ZnO annealing temperatures were estimated using Eq.4.6, and are presented in Table 4.1.

From the C-V characteristics, it was found that the charge carrier density in the devices increased from  $8.0 \times 10^{17} \text{ cm}^{-3}$  to  $2.1 \times 10^{19} \text{ cm}^{-3}$  (about 25 times) as the

annealing temperature increased. This may be due to the changes in barrier height, facilitating injection of much larger number of charge carriers into the device. The corresponding built-in voltage values are tabulated in Table 4.1. ZnO annealed at 450°C showed ohmic nature due to the intermixing of ITO and ZnO layers owing to diffusion at the interface [Lee et al. 2001 Tang et al. 2001].

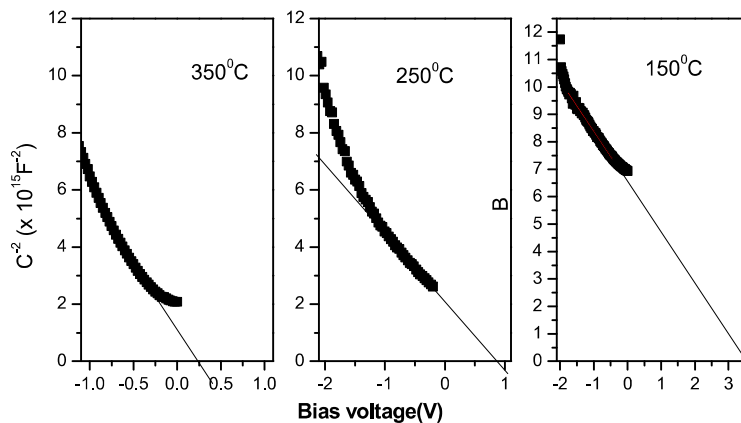


**Figure 4.6** Mott-Schottky plots (C-V characteristics) for the electron only device made at different ZnO annealing temperatures.

#### 4.2.6 IS measurements

In order to investigate the influence of factors affecting charge transport in devices with annealed ZnO, we employed impedance spectroscopy. The corresponding Cole-Cole plots are shown in Figure 4.7(a) for the device with ZnO annealed at 350°C, at different bias voltages. For a given bias, the results showed only one semicircle in the measured frequency range (20Hz to 1kHz) indicating the predominance of single carrier lifetime. The Cole-Cole plots shown in Figure 4.7(a), can be modelled by the equivalent circuit shown in Figure 4.7(b) and the impedance of the equivalent circuit may be written as

$$z(f) = Re[z(f)] - jIm[z(f)] = R_s + \frac{R_p}{1 + j\omega\tau} \quad (4.7)$$

where  $\omega = 2\pi f$  is the angular frequency of ac signal,  $\tau$  is the charge carrier relaxation time,  $R_s$  is the series resistance of the device which is a measure of the resistance of the metal /semiconductor interface and  $R_p$  is the bulk resistance of the semiconductor

film. The estimated parameters from the equivalent model of the devices were plotted as a function of bias voltage in Figure 4.7(c). The parallel resistance–voltage plots (Figure 4.7(c)), showed exponential behaviour. In contrast, the value of constant phase element (CPE) is seen to be constant with changing applied bias and has a value  $\sim 1.8 \times 10^{-8}$  F for 150°C,  $1.2 \times 10^{-8}$  F for 250°C and  $1.6 \times 10^{-8}$  F for 350°C and was seen to be constant with changing applied bias. Further, the slopes obtained from the log(resistance)-voltage plots for different annealing temperatures (Figure 4.7(d)) were 3.98 for 150°C, 3.35 for 250°C and 1.51 for 350°C, respectively. This indicated that SCLC was the dominant mechanism in our devices having exponential trap distribution [Bi-Xin et al. 2011]. The decrease in slope values with increase in annealing temperatures indicated reduction in trap density in the bulk of ZnO film. Interestingly, the device with ZnO annealed at 450°C exhibited ohmic conduction.

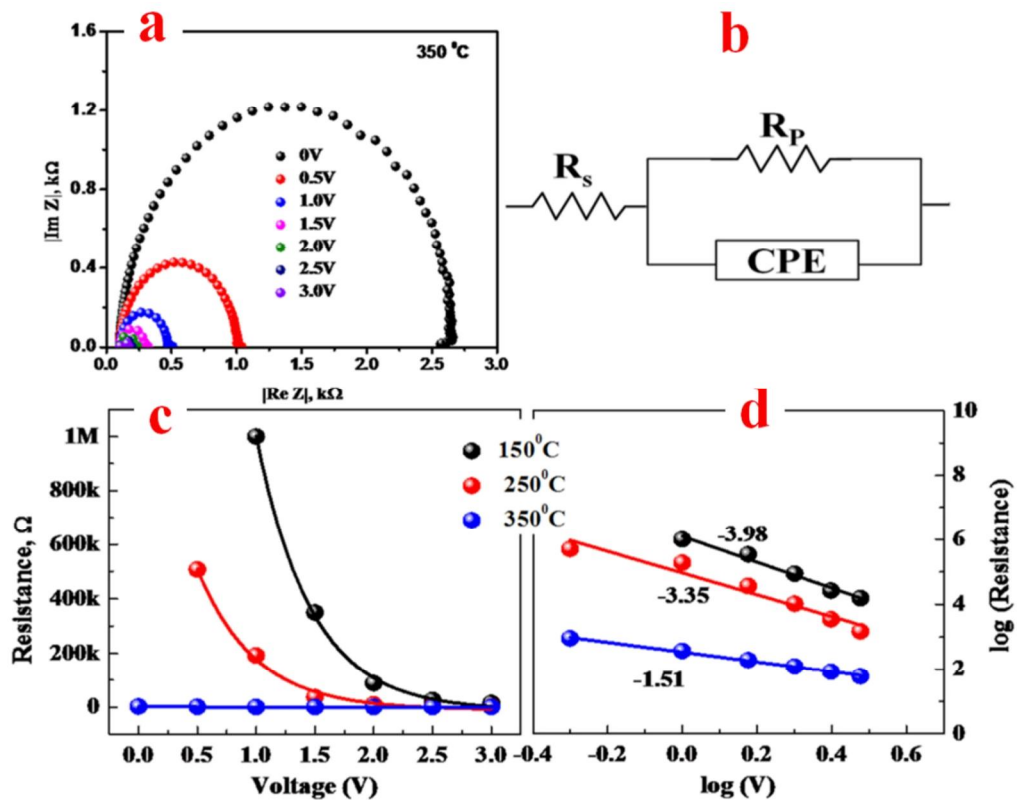


**Figure 4.7** (a) Cole-Cole plots for ZnO annealed at 350°C as a function of bias voltage, (b) equivalent circuit to fit impedance plots (c) resistance-voltage measurements for devices at different annealing temperatures and (d) plots of parallel resistance voltage plots in logarithmic values to verify SCLC mechanism

---

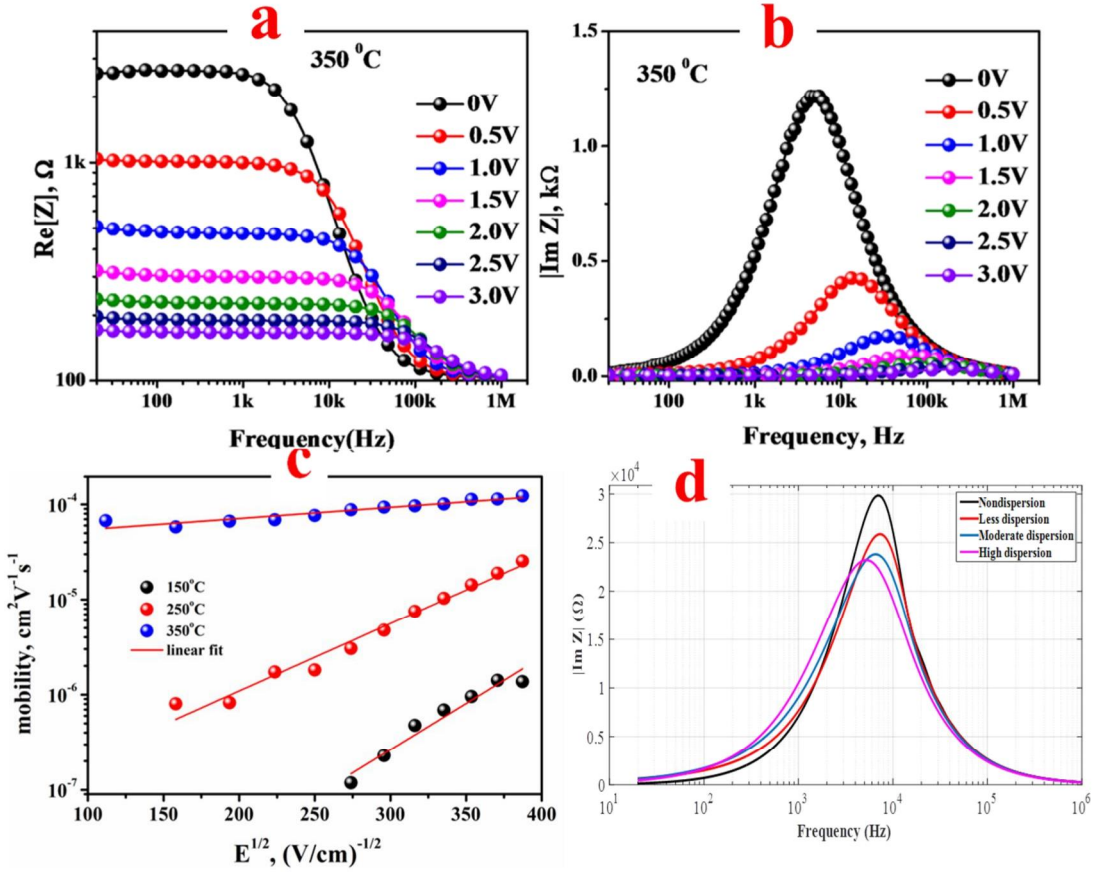
Figure 4.8(a) depicts the Re [Z]-f characteristics as a function of applied dc bias for the device fabricated with ZnO annealed at 350°C. At lower frequencies, it is seen that the magnitude of Re[Z] decreases progressively from 1000kΩ to 15.3 kΩ with an increase in dc bias over a range of 1-3V indicating that the device turned from high resistance state to the semiconducting state. This is due to the increase in charge carrier injection and better transport promoted by the applied bias resulting in a reduction in the bulk resistance of the device. However, at frequencies greater than 100 kHz, the Re[Z]-f plot for all dc biases converged. It can also be noticed from the plot that, the point at which Re[Z] gradually changes from being frequency independent to becoming frequency dependent shifts towards higher frequencies with increase in bias voltage. This may be attributed to increase in conductivity due to the release of the space charge resulting from reduction in barrier height as the applied bias increases. It is also seen that the magnitude of the Re[Z] reduces with increase in annealing temperature of ZnO. This may be due to the reduction in ITO/ZnO potential barrier height with increasing annealing temperature; the barrier height is reduced from 550meV to 333meV (Table 4.1).

Figure 4.8(b) shows the Im[Z]-f plots for different dc bias voltages. Generally, the frequency corresponding to the peak in Im[Z]-f plot is used to estimate the relaxation time ( $\tau_r$ ) and, thereby, the mobility of the charge carriers in the ZnO layer. The peak shifts to higher frequencies with increase in dc bias voltage, but its magnitude reduces monotonically. The charge carrier mobility ( $\mu$ ) of the annealed ZnO films were estimated using the relation [Tsang et al. 2006a, Tripathi et al. 2011]

$$\mu = \frac{d^2}{\tau_{dc} V_{dc}} \quad (4.8)$$

Here,  $d$  is the thickness of the active layer,  $V_{dc}$  is the applied dc bias and  $\tau_{dc} = \kappa \tau_r$ ,  $\kappa$  is numerical correction factor accounting for dispersive transport [Tripathi et al. 2011].  $\tau_{dc}$  and  $\tau_r$  are the average charge carrier transit time and charge carrier relaxation time, respectively. From the computer simulations, similar to that described in Chapter 3, it was found that the value of  $\kappa = 0.46$  for the nondispersive transport

and changed by  $\pm 0.052$  in case of dispersive transport. The simulated frequency dependent impedance plots are presented in Figure 4.8(d).



**Figure 4.8(a)**  $\text{Re}[Z]-f$  characteristics of the ZnO film annealed at  $350^\circ\text{C}$ , **(b)**  $\text{Im}[Z]-f$  characteristics of the ZnO film annealed at  $350^\circ\text{C}$  and **(c)** Poole-Frenkel mobilities for samples annealed at different temperatures and **(d)** computer simulations to find the numerical constant  $\kappa$ .

The Poole-Frenkel field-dependent mobility is given by the relation [Brütting et al. 2001]

$$\mu(E) = \mu_0 \exp(\beta\sqrt{E}) \quad (4.9)$$

where  $E = V/d$  is the applied electric field at a given voltage  $V$ . The field-independent mobility ( $\mu_0$ ) and the Poole-Frenkel (PF) coefficient ( $\beta$ ) are obtained from the intercept and slope of the linear fit to the above equation (Figure 5(c)). The charge carrier mobility values, thus obtained, were comparable with those obtained from sol-

---

gel ZnO thin films reported by others [Patil et al. 2011]. From Table 4.1, it is evident that the electron mobility of the ZnO increased by up to 5 orders of magnitude as the ZnO annealing temperature increased from 150°C to 350°C. This enhanced mobility at higher temperatures can be attributed to the following reasons: (i) reduction of barrier height, which facilitates higher electron injection from ITO to ZnO, and (ii) increase in the crystallinity of ZnO with annealing temperature which results in larger grain size and hence reduction in grain boundaries (which act as defects/traps). Higher charge injection due to the reduction of barrier height, lower defect density and improved crystallinity (increased grain size) makes the ZnO film annealed at 350°C, a suitable for optoelectronics applications.

#### 4.3 CONCLUSION

In this chapter, we have investigated four electron-only devices having the configuration: ITO/ZnO/Al by varying the annealing temperature of the active layer (ZnO). The improvement in the current density as well as the charge carrier mobility of the devices, made with ZnO film annealed at 350°C, is attributed to the increase in grain size, reduction of the Schottky barrier height and higher carrier density. We infer that the electrical conduction in these devices is dominated by SCLC mechanism with an exponential density of traps. The DOS at Fermi level is found to be  $\sim 10^{17}$  eV<sup>-1</sup>cm<sup>-3</sup> and is almost same for all the devices. The electron mobility values are obtained from the impedance measurements. A larger electron mobility of  $1.91 \times 10^{-5}$  cm<sup>2</sup>V<sup>-1</sup>s<sup>-1</sup> was achieved in the device with ZnO film annealed at 350°C. The results suggest that ZnO films annealed at 350°C are suitable for the optoelectronic device applications as they show high electron mobility.

---

## CHAPTER 5

### OPTOELECTRONIC PROPERTIES OF VOPc/ZnO HYBRID DIODES

#### *Overview*

*Chapter 5 explores the optoelectronic properties of a hybrid p-n diode using an organic p-type VOPc and n-type ZnO. In this chapter, the p-n junction diodes in the configuration ITO/ZnO/VOPc/MoO<sub>3</sub>/Al were investigated for the electrical properties in dark and under illuminated conditions. The results clearly demonstrate that a p-n junction with ZnO film annealed at 350°C exhibits much better optoelectronic characteristics on account of increased grain size, improved charge injection due to the reduction of barrier height and hence higher (up to 5 orders) charge carrier mobility.*

#### 5.1 INTRODUCTION

Organic-inorganic hybrid diodes have been of interest in optoelectronic applications in recent years. They are seen to play a prominent role in devices such as light emitting diodes, solar cells and photodiodes [J. Bolink et al. 2010, Sessolo and Bolink 2011, Wright and Uddin 2012, Kettle et al. 2015]. In such hybrid diodes, one can exploit the advantages of both organic and inorganic materials. Inorganic semiconductors, such as Zinc Oxide (ZnO) and Titanium oxide (TiO<sub>2</sub>) are stable n-type semiconductors and have higher electron mobility ( $5\text{-}6\text{ cm}^2\text{ V}^{-1}\text{ s}^{-1}$ ) compared to organic semiconductors ( $10^{-5}$  to  $1\text{ cm}^2\text{ V}^{-1}\text{ s}^{-1}$ ) [Ong et al. 2007]. On the other hand, organic p-type semiconductors (phthalocyanines, pentacene, and P3HT) are known to have broad absorption spectra in the visible region which can lead to high efficiency in photodiodes and solar cells [Beek et al. 2006, Sharma et al. 2006, Lee et al. 2011]. Moreover, these devices can be easily fabricated at low cost, even on flexible substrates [Wang et al. 2010]. Hybrid interfaces of ZnO with organic semiconductors have been studied by several groups to explore their suitability in applications such as photodiodes [Kumar et al. 2009, Gupta et al. 2011, Lee et al. 2011, Yuan 2014a, Yuan et al. 2014, Kettle et al. 2015].

---

Recently, various nanostructures of ZnO (particles, rods, tubes, wires, belts, etc.) have been explored due to their potential applications in various miniaturized devices. Due to the ease of synthesis, high surface area and superior optoelectronic properties, ZnO nanoparticles have been widely exploited. Since a p-n junction is fundamentally important in all semiconductor devices, it is imperative to understand the role of quality of the junction on charge transport, in order to achieve high device performance. In devices involving ZnO/organic semiconductor interfaces, the effect of annealing of ZnO layer on the interface properties have not been explored much.

In this chapter, we have investigated the optoelectronic properties of hybrid diodes involving ZnO and Vanadyl-phthalocyanine (VOPc), a well-known metal phthalocyanine (MPc). MPcs possess relatively good electronic properties, are inexpensive and exhibit high environmental stability [Song et al. 2008, Pan et al. 2011]. ZnO/MPc photodiodes have been investigated by several groups [Gupta et al. 2011, Ma et al. 2011, Yuan et al. 2012]. Our specific choice of VOPc was based on the fact that it is a non-planar phthalocyanine molecule and is known to offer better performance in comparison to planar phthalocyanines [Kim and Yim 2011, Jin et al. 2014, Ramar et al. 2015]. Further, VOPc is commonly employed as a hole transport material [Zhu et al. 2001].

To the best of our knowledge, photodiodes based on ZnO/VOPc combination has not been investigated so far. In an earlier work on hole transport through the VOPc thin films, we have shown that films deposited at low rates are better for optoelectronic applications (Chapter 3). In addition, the effects of annealing ZnO film at different temperatures on the charge transport properties of ITO/ZnO/Al electron-only devices were explored. It was found that the ZnO film annealed at 350°C had better electrical properties (Chapter 4). In this chapter, the fabrication and electrical characterization of p-n junctions with the configuration ITO/ZnO/VOPc/MoO<sub>3</sub>/Al, is investigated under dark and illuminated conditions. These investigations were carried out with the motivation of understanding charge carrier dynamics at ZnO/VOPc interfaces and its effect on the charge transport.

---

## 5.2 FABRICATION AND CHARACTERIZATION OF THE DEVICES

### 5.2.1 Fabrication of hybrid p-n junction diode

VOPc (dye content >85%) was procured from Alfa Aesar and was used without any further purification. A 100 nm thick VOPc layer was deposited on ZnO thin films (prepared as described in Chapter 4) by thermal evaporation at a base pressure of  $8 \times 10^{-6}$  mbar and a deposition rate of 0.1-0.2 Å/s. Subsequently, a thin layer of Molybdenum Oxide ( $\text{MoO}_3$ , 3 nm) was deposited at a rate of 0.1-0.2 Å/s to facilitate hole injection. Finally, a 100 nm thick Al layer (electrode) was deposited as described earlier for the electron only devices. The schematic of the fabricated device configuration is shown in Figure 5.1. All the measurements (characterizations) were performed at room temperature and under ambient conditions without any encapsulation of the devices.

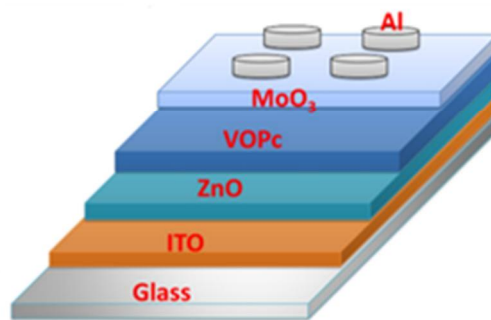


**Figure 5.1** Schematic of ZnO/VOPc hybrid diode

### 5.2.2. J-V characteristics

Figure 5.2(a) shows the energy level diagram of the p-n junction diode with the configuration: ITO/ZnO (annealed)/VOPc/ $\text{MoO}_3$ /Al. The energy levels of VOPc and  $\text{MoO}_3$  have been taken from the literature [Sakurai et al. 2011, Kiran et al. 2017]. In our earlier work, it was shown that VOPc thin films produced at low deposition rates ( $\sim 0.1$  Å/s) exhibit high hole mobilities (Chapter 3). Therefore, we investigated the characteristics of the p-n junction formed by VOPc with ZnO.

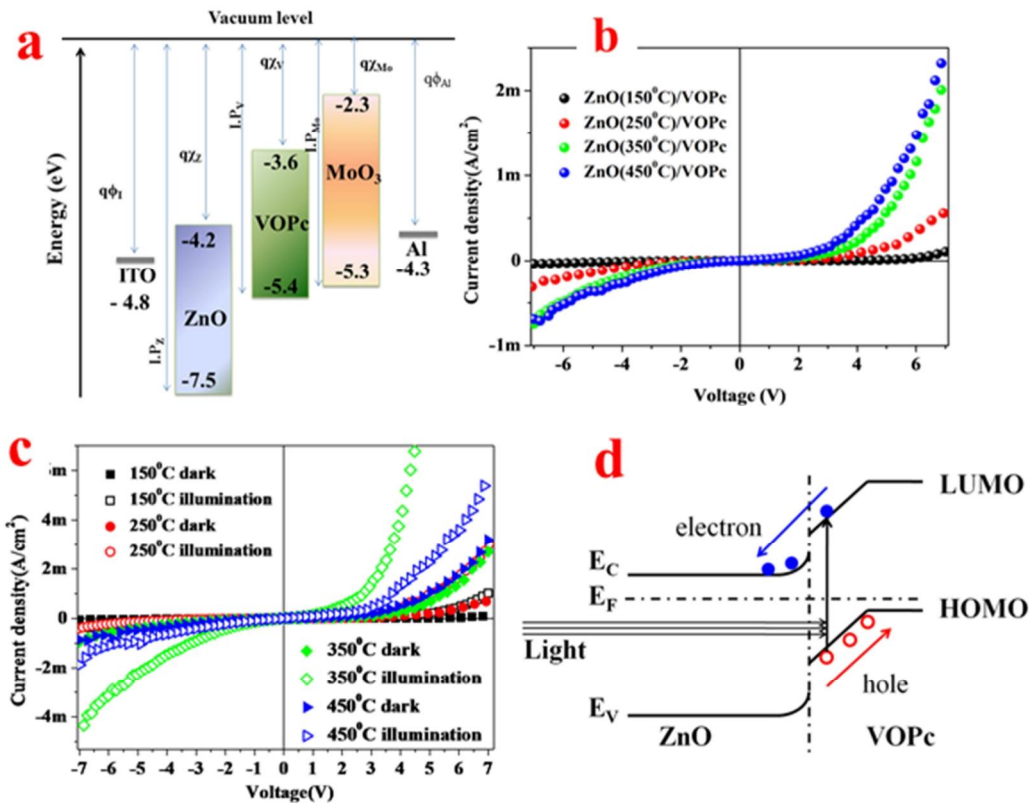


**Figure 5.2(a)** Energy level representation of the VOPc/ZnO diode in the configuration: ITO/ZnO/VOPc/MoO<sub>3</sub>/Al; **(b)** J-V characteristics of a VOPc/ZnO p-n junction in dark conditions; **(c)** J-V characteristics of a VOPc/ZnO p-n junction in dark and illuminated conditions and **(d)** illustration of photocurrent generation mechanism in VOPc/ZnO p-n diode. The plots in different colors correspond to different annealing temperatures of the ZnO film indicated in the inset.

The room temperature J-V characteristics in dark and illuminated conditions for the p-n junction with ZnO annealed at different temperatures are shown in Figure 5.2(b) and (c), respectively. When a negative voltage is applied to ITO, the p-n junction gets forward biased when ZnO is held more negative than VOPc. Therefore, the current flows easily through the junction. When ITO is given positive bias, ZnO becomes more positive with respect to VOPc making the junction reverse biased, thereby limiting the current flow. It is seen that all the diodes clearly exhibit rectification behaviour when not exposed to light. On fitting the experimental data of J-V measurements at different ZnO annealing temperatures, it was observed that the

---

ideality factors were rather high, ranging from 19 to 24 compared to that of an ideal diode ( $n=1$ ). This could be due to the following reasons (i) the presence of imperfections/traps at ZnO/VOPc interface which may lead to different tunneling assisted transport, and (ii) enhanced electron-hole recombination in the depletion region (ZnO/VOPc), thereby increasing the series resistance of the device.

Further, from Figure 5.2(b), it can be seen that the current through the device is higher if the ZnO film is annealed. As mentioned earlier, higher annealing temperatures increase the ZnO grain size (from 11 nm to 21 nm, Chapter 4), which in turn leads to a reduction in grain boundaries and also to lowering of the Schottky barrier height from 572meV to 471meV. This might be the reason for the higher current through the devices having annealed ZnO films. When the p-n diode is subjected to illumination, the ideal diode equation is given by [Yuan 2014a]

$$I_{total} = I_{dark} + I_{photo} = I_{sat} \left[ \exp\left(\frac{V}{nV_t}\right) \right] - I_{photo} \quad (5.1)$$

where  $I_{photo}$  is the photocurrent generated due to the illumination of the device. The mechanism which governs the charge transfer across the VOPc/ZnO interface is illustrated in Figure 5.2(d). When the device is illuminated from ITO side, a large number of excitons are formed in the VOPc layer due to absorption of photons. The optical transparency of all the ZnO films were greater than 85%, (see Figure 4.4a in Chapter 4). The photogenerated excitons diffuse into the VOPc/ZnO interface. At the interface, the dissociation of excitons takes place rapidly due to the large LUMO offset between the ZnO and VOPc. Though the CB of ZnO is much lower ( $\sim 0.9\text{eV}$ ) than the LUMO of VOPc, the electrons are easily transferred to the ZnO layer and are collected by the ITO electrode. Simultaneously, the holes move easily through the VOPc layer, as it acts as an efficient hole transporter, and gets collected by the Al metal electrode. The photocurrent responsivity ( $R_{ph}$ ) is given by [Yuan 2014a]

$$R_{ph} = \frac{I_{photo}}{P_{optical}} \quad (5.2)$$

where,  $P_{optical}$  is the incident optical power. The values of ' $R_{ph}$ ' estimated at different annealed temperatures are presented in Table 5.1.

It is observed from Figure 5.2(b) that the dark current is more for the p-n diode with ZnO annealed at 450°C. However, from Figure 5.2(c), it can be observed that the photocurrent and, hence, the photocurrent responsivity (both at positive and negative bias voltages) is high for the device with ZnO annealed at 350°C. This may be due to the lower electron-hole recombination at the interface and better charge collection in case of the hybrid p-n diode with ZnO annealed at 350°C.

**Table 5.1** Estimated p-n junction parameters from J-V characteristics

ZnO annealing temperature	Measurement condition	Barrier height (meV)	RR@6V	Photo responsivity (mA/W)	
				@ -6V	@6V
150°C	Dark	562	0.5	6.2	13.0
	illumination		1.8		
250°C	Dark	543	1.6	12.9	33.3
	illumination		7.7		
350°C	Dark	490	2.4	131	470
	illumination		6.0		
450°C	Dark	471	2.9	12.5	47.5
	illumination		3.3		

### 5.2.3. IS measurements

To further investigate the photoresponse of the device, IS measurements were also carried out for the p-n diode with ZnO film annealed at 350°C. Figure 5.3(a) shows the Cole-Cole plots generated for the same device under dark and as well as illuminated conditions. Figure 5.3(b) displays the real part of the impedance versus frequency at a given bias. From Figure 5.3(a) and (b), it can be noted that the difference between the Cole-Cole plots for a given condition (dark or illuminated) at a particular bias represents the rectification ratio. Also, the difference between the Cole-Cole plots for dark and illuminated conditions at a given bias (say at -6V) is indicative of the photo-response of the p-n junction.

The Cole-Cole plots for VOPc/ZnO diode interface at a given bias show a single semicircle for a given condition (dark or illuminated), which indicates the

predominance of a single carrier lifetime. It can be seen that, at higher frequencies, the Cole-Cole plots are not perfect semicircles. To understand the nature of the Cole-Cole plots, we employed the equivalent circuit model for our devices, similar to the one shown in Figure 4.7(b) in Chapter 4.

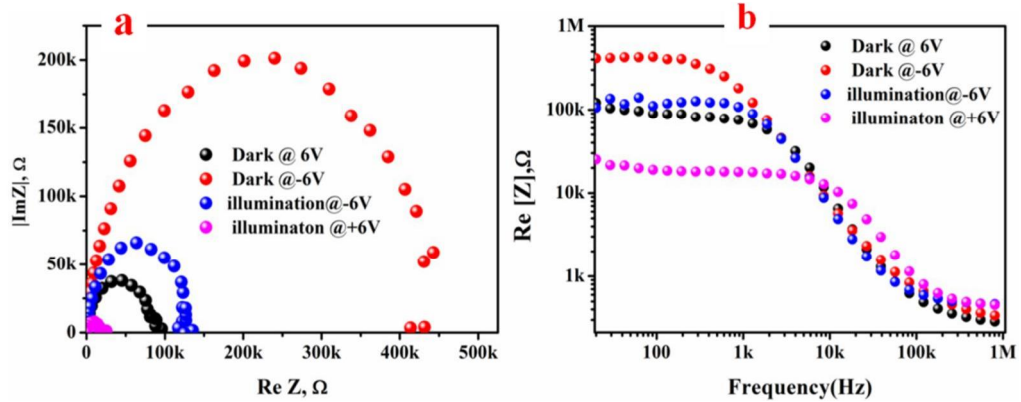


**Figure 5.3(a)** Cole-Cole plots for VOPc/ZnO device (annealed at 350°C) p-n junction in dark and illuminated conditions for a given bias and **(b)**  $\text{re}[z] - f$  plots of a VOPc/ZnO (annealed at 350°C) p-n junction diode.

In general, at a given bias, two semicircles are expected for a junction of two materials. Since the bulk resistance ( $R_p$ ) of ZnO in the electron only device configuration (Figure 4.7a) is almost equal to the estimated series resistance ( $R_s$ ) for the VOPc/ZnO interface (Figure 5.3(a)), the semicircle corresponding to ZnO is not observed in the obtained Cole-Cole plots for VOPc/ZnO. It is also observed from Figure 5.3 (b) that the bulk resistance of the VOPc/ZnO p-n diode under illumination is, approximately, 5 times lower in forward bias and 2 times lower in reverse bias than that under dark condition at a bias of 6V. The rectification ratios were found to be 3.42 and 8.1 in dark and illuminated conditions at 6V, respectively. These rectification ratios agree well with the values obtained from the J-V characteristics. From IS studies, it is clear that the excitons are created only in the VOPc layer and the higher photo-current is generated due to the reduction in the VOPc bulk resistance. A higher photocurrent in the devices with ZnO annealed at 350°C is attributed to the collective effects of ZnO and VOPc films resulting in efficient exciton dissociation at ZnO/VOPc interface and, thereby improved charge collection.

---

### 5.3 CONCLUSION

In this chapter, we have investigated four hybrid diode devices having the configuration: ITO/ZnO/VOPc/MoO<sub>3</sub>/Al by varying the annealing temperature of the ZnO film (active layer). The interface parameters such as ideality factor ( $n$ ), the Schottky barrier height ( $q\phi_B$ ) and the rectification ratio (RR) of the devices were determined from J-V characteristics. It is observed that the devices with the ZnO film annealed at 350°C show higher photocurrent responsivity (470mA/W) at a wavelength 660nm. This suggests better exciton dissociation at the interface and, hence, efficient charge collection at both the electrodes. Hence, ZnO films annealed at 350°C are suitable for organic-inorganic hybrid optoelectronic device applications.

---

## CHAPTER 6

### OPTOELECTRONIC PROPERTIES OF HYBRID DIODES BASED ON VOPc AND ZnO NANOROD THIN FILMS

#### *Overview*

*This chapter explores the optoelectronic properties of hybrid p-n junction diodes based on p-type VOPc and n-type ZnO nanorods (ZNR) with the configuration: ITO/ZnO nanorods (ZNR)/VOPc/ MoO<sub>3</sub>/Al. Vertically aligned ZnO nanorods were grown using a simple aqueous solution (AS) method as a function of growth temperature. The correlation between the morphology of ZNR films and the optoelectronic properties of the ZNR/VOPc hybrid devices was investigated. The results show that the hybrid diodes with ZNR films grown at 120<sup>o</sup>C offer the best optoelectronic properties.*

#### 6.1 INTRODUCTION

We have seen in the previous chapter that the morphology of the films plays a significant role in enhancing the performance of organic-inorganic photodiodes. By utilizing the advantages of the individual material properties, such as high charge carrier mobility and environmental stability, these hybrid p-n junctions can minimize several factors limiting the performance of the devices. Hybrid p-n interfaces of ZnO nanostructures with organic semiconductors have been explored by several research groups due to their potential applications in miniature devices [Beek et al. 2006 Sharma et al. 2006 Gupta et al. 2011a Yuan 2014a Yuan et al. 2014 Pickett et al. 2017]. Since a p-n junction is the basic component of any optoelectronic device, it is essential to understand the charge carrier dynamics at such heterojunctions. As the next step in the investigations, we studied devices made using ZnO nanorod (ZNR) films instead of ZnO nanoparticle films forming p-n junction with organic semiconductor films. The heterojunction devices based on ZnO/MPcs have been well studied [Gupta et al. 2011a, Yuan et al. 2012, Al-Hartomy et al. 2014, Yuan 2014b]. However, the devices based on ZNR/MPcs have not been explored much. Especially,

---

devices having a heterojunction of MPc film and ZNR (vertically aligned) film or ZNR film prepared by aqueous solution growth has not been studied so far. The influence of the growth parameters of vertically aligned nanorods film on the ZNR/MPc heterojunction also needs to be studied.

In Chapter 3, we have shown that VOPc films deposited at lower rates acquire improved charge carrier mobilities. It is also shown in Chapter 5 that ZnO nanoparticle films, annealed at 350<sup>0</sup>C, exhibit better optoelectronic properties in hybrid diodes based on ZnO and VOPc thin films. However, to the best of our knowledge, the hybrid devices based on ZNR/VOPc have not been investigated so far.

In this chapter, the optoelectronic properties of hybrid diodes involving ZNR and VOPc films are investigated as a function of nanorod growth temperature. We first investigated the effect of growth temperature on the structural, morphological and optical properties of the ZNR thin films. Subsequently, we also fabricated and performed electrical characterization of p-n junction devices with the configuration: ITO/ZNR/VOPc/MoO<sub>3</sub>/Al, under dark and illuminated conditions. These investigations were carried out with the motivation to understand the charge carrier dynamics at ZNR/VOPc interfaces and its effect on charge carrier transport.

## **6.2 FABRICATION AND CHARACTERIZATION OF THE DEVICES**

### **6.2.1 Preparation of ZNR thin films and fabrication**

The preparation of ZNR thin films was done in two steps, namely, (i) seed layer deposition and (ii) nanorod growth. The details of these steps are described below.

#### ***Preparation of seed layer thin films***

The nanoparticulate seed layer thin films of ZnO were prepared by sol-gel spin coating as described in Chapter 4. The prepared sol-gel was spin coated on pre-cleaned ITO coated glass substrates at a spin rate of 500 rpm for the first 30s and then 100 rpm for next 30sec. The deposited films were baked at 120°C for 10 min to remove the solvents.

---

### ***Growth of ZNR thin films***

To grow the nanorods of ZnO, a 1:1 aqueous solution of 0.06M zinc nitrate hexahydrate and hexamethyl tetra-amine was prepared in a glass reagent bottle (GL 45, BOROSIL). This served as the precursor solution. The substrates with pre-coated ZnO seed layer thin film were dipped vertically into the precursor solution in the bottle and kept in an oven at the desired temperature. After one hour, the substrate was taken out and cleaned thoroughly multiple times with distilled water and further annealed at 350 °C for about 60 min. This process yielded ZnO nanorod thin film with nanorods aligned vertically to the surface of the substrate. These films were characterized in terms of their structural, morphological and optical properties.

The aqueous solution (AS) method employed in this work is a simple and less expensive technique, allowing one to grow uniform vertically aligned nanorods on large scale at low temperatures. In the present work, we have grown the nanorods at three different temperatures viz., 60 °C, 90 °C and 120 °C. We were not able to proceed beyond 120 °C due to rapid evaporation.

#### **6.2.2 Fabrication of hybrid photodiode**

The VOPc layer (100 nm thick) was deposited on the pre-coated ZNR films using thermal evaporation method at a base pressure of  $8 \times 10^{-6}$  mbar at a deposition rate of 0.1-0.2 Å/s. Subsequently, a thin layer of Molybdenum Oxide ( $\text{MoO}_3$ , 3 nm) was deposited at a rate of 0.1-0.2 Å/s to facilitate hole transport. Finally, a 100 nm thick Al layer (electrode) was deposited on the top as described earlier (Chapter 5).

#### **6.2.3 Structural and morphological properties.**

The XRD pattern of the ZNR thin films grown on ITO coated glass substrate at different temperatures is shown in Figure 6.1 (a). This clearly indicates that all the ZNR films are crystallized in hexagonal wurtzite structure [JCPDS 36-1451]. The intense peak appearing at  $2\theta=34.2^\circ$  is assigned to (002) crystal plane. This indicates that almost all the nanorods are oriented parallel to the c-axis. Further, the peak intensity is found to increase with growth temperature. A less intense peak also appears in the XRD pattern of each sample at  $2\theta=30.2^\circ$  and this is ascribed due to the

ITO film [Kärber et al. 2011, Henni et al. 2016]. The average crystallite size (~diameter) of the nanorods was estimated using Scherrer's formula and is found to increase from 31 nm to 50 nm as the growth temperature increases from 60°C to 120°C. The results are presented in Table 6.1.

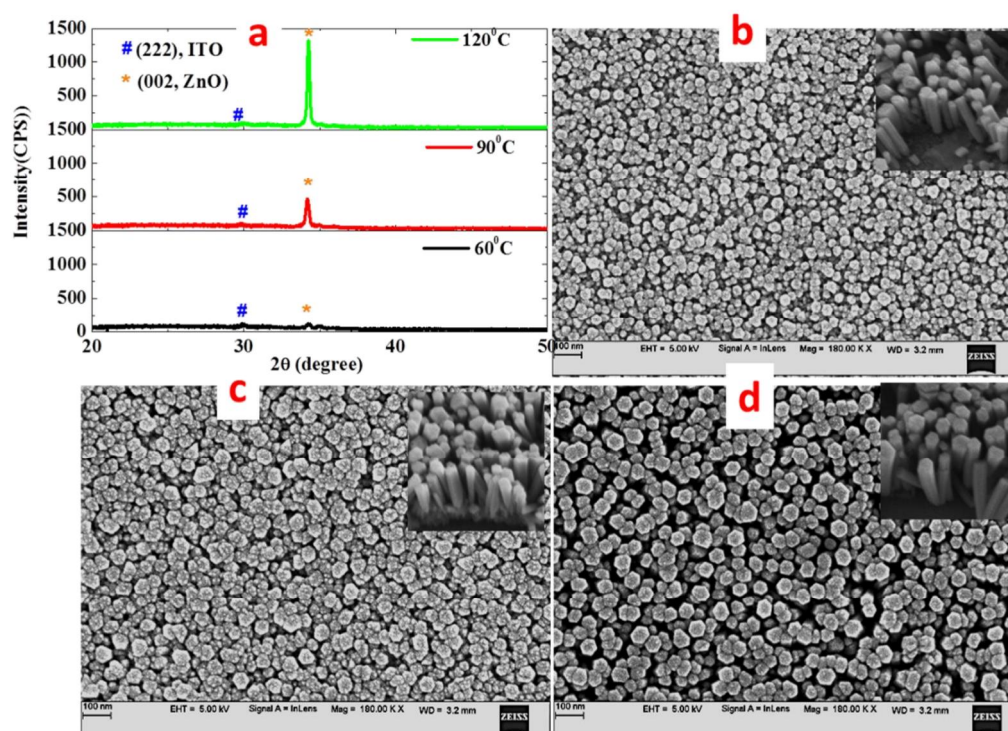


**Figure 6.1(a)** X-ray diffraction pattern of ZNR thin films grown at different temperatures; **(b)** SEM image of ZNR film grown at 60°C, **(c)** at 90°C and **(d)** at 120°C for about one hour (scale is 100 nm); insets show the columnar structures that confirm the vertical growth perpendicular to the plane of ITO substrate.

The SEM images of nanorods grown at different temperatures on ITO substrates are shown in Figure 6.1 (b-d). It shows that all the ZnO nanorods are oriented nearly perpendicular to the substrate plane regardless of growth temperature. This confirms the conclusion drawn above, on the basis of XRD data, that the ZNR films have highly crystalline structure. The top view of SEM images reveals that the nanorods have hexagonal shape, suggesting that the nanorods grew along the (002) direction at various temperatures. However, the diameter, as well as the length of the nanorods, was found to increase with increase in the temperature of the precursor

solution. It is observed that the average diameter of the nanorods increases from 38 nm to 60 nm with increase in the growth temperature from 60<sup>0</sup>C to 120<sup>0</sup>C. It is also observed that the inter nanorod gap increases with the increase in growth temperature. Further, the length of the nanorods is seen to increase by about 30% from ~350 nm to ~480 nm as the growth temperature increases from 60<sup>0</sup>C to 120<sup>0</sup>C. These results correlate well with the estimated crystalline sizes from the XRD spectra. The results are tabulated in Table 6.1.

#### 6.2.4 Optical Transmission spectra

The optical transmission spectra of ZNR films grown at different temperatures are shown in Figure 6.2. It is clearly seen that all the samples show a transmission greater than 80% in the visible region. The plot of  $\alpha^2$  versus  $h\nu$  for ZNR films grown at different temperatures are shown in the inset of Figure 6.2. The optical band gap ( $E_g$ ) values were estimated by extrapolating the straight line portion of the plot to x-axis and were found to be ~3.24 eV for all the samples. These  $E_g$  values are slightly lesser than those obtained for ZnO nanoparticle films (3.28 eV, Chapter 4). This is ascribed to the reduction of extended localized states at CB and VB in highly crystalline ZNR films in comparison with ZnO nanoparticle films [Mathew et al. 2012].

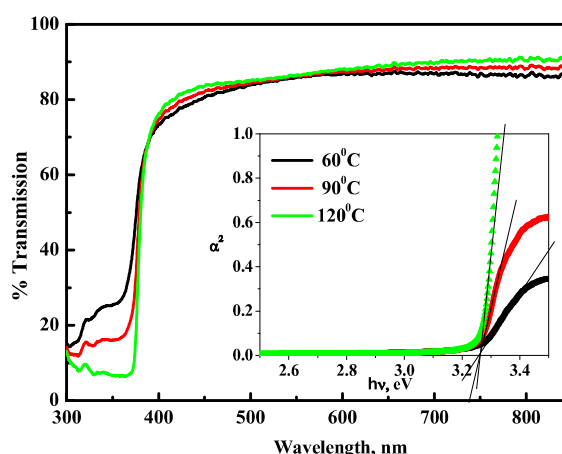


**Figure 6.2** Optical transmission spectra of ZNR films at different growth temperatures. The inset shows Tauc's plots to estimate band gap of ZNR films at the different growth temperature.

## 6.2.5 J-V characteristics

The schematic of the proposed p-n hybrid diode is shown in Figure 6.3(a), and its energy level diagram is shown in Figure 6.3(b). The energy level values of the materials used in the devices have been taken from our previous work and from the reported literature [Sakurai et al. 2011, Kiran et al. 2017a].

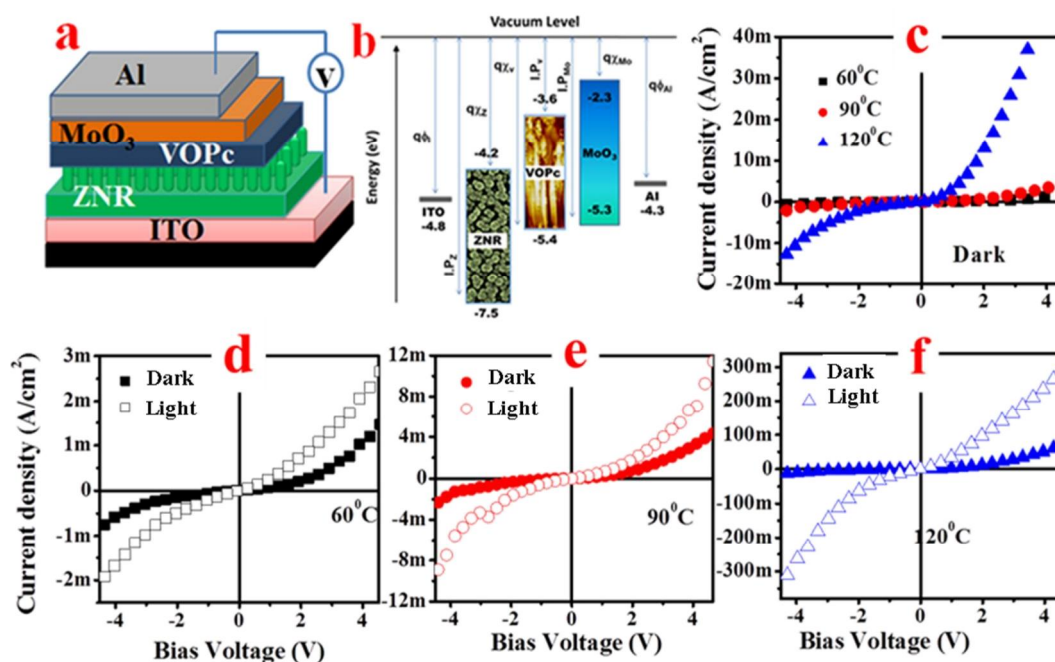


**Figure 6.3(a)** Schematic of fabricated hybrid diode, **(b)** the energy level diagram for various layers in the fabricated device, **(c)** J-V characteristics of devices under dark and **(d-f)** J-V characteristics of the hybrid diodes under dark and illumination at a given ZNR growth temperature

The J-V characteristics of p-n junctions involving ZNR films, grown at various temperatures under dark condition are shown in Figure 6.3(c). All the diodes clearly show rectification behavior and the rectification ratio (RR) increases from 1.79 to 5.40 as the ZNR films growth temperature increases. On fitting the experimental data of J-V curves of ZNR films, grown at different temperatures, to the diode equation, it was found that the value of the ideality factor ( $n$ ) reduces with the increase of growth temperature. It is also found that the  $n$  values are relatively high, ranging from 6.71 to 5.16 compared to that of an ideal diode ( $n=1$ ). However, these

values are found to be lower compared to those for the device fabricated using nanoparticle ZnO thin films (Chapter 5). This may be due to lesser electron-hole recombination in the depletion region of ZNR/VOPc, leading to decrease in the series resistance of the device [Darwish et al. 1996, Mayes et al. 2004, Dey et al. 2015].

From Figure 6.3 (c), it can be seen that the current density of the device is higher for the devices with ZNR films grown at higher temperatures (120<sup>0</sup>C). As mentioned earlier, higher growth temperatures lead to increased ZNR crystallite size (from 31 nm to 50 nm, from XRD data), and also to lowering of the interfacial barrier height from 727 meV to 650meV (estimated using Eq. 4.2 and 4.3). This might be the reason for high current through devices having ZNR films grown at higher temperatures 120<sup>0</sup>C. Correspondingly, the turn-on voltage of the diodes was reduced from 3.84V to 0.56V with increasing ZNR growth temperature (presented in Table 6.1). Further, the current density through the ZNR films (Figure 6.3(c)) is found to be 2 orders higher in magnitude than that for the devices with nanoparticle ZnO films (Figure 5.2(b)). This can be attributed to the higher crystallite size, larger diameter of the nanorods, and to the higher donor-acceptor interfacial area due to the filling of gaps between the nanorods by VOPc (as the gaps observed from Figure (6.1)).

**Table 6.1** Estimated p-n junction parameters from J-V characteristics

T ( <sup>0</sup> C) <sup>a</sup>	Condition	n <sup>b</sup>	I <sub>o</sub> (amp) <sup>c</sup>	V <sub>on</sub> (V) <sup>d</sup>	Φ <sub>B</sub> (meV) <sup>e</sup>	RR <sup>f</sup>	R <sub>ph</sub> (A/W) <sup>g</sup>	
							@4.5V	@ -4.5V
120	Dark	5.16	6.37×10 <sup>-7</sup>	0.56	0.650	5.40	11.56	16.28
	Light	5.71	1.35×10 <sup>-5</sup>	0.06	0.570	1.15		
90	Dark	5.60	5.59×10 <sup>-8</sup>	2.35	0.713	1.95	0.267	0.372
	Light	5.56	2.16×10 <sup>-7</sup>	1.46	0.678	1.27		
60	Dark	6.05	3.23×10 <sup>-8</sup>	3.84	0.727	1.79	0.058	0.061
	Light	6.71	1.65×10 <sup>-7</sup>	2.50	0.685	1.42		

<sup>a</sup> Nanorod growth temperature

<sup>b</sup> diode ideality factor

<sup>c</sup> reverse saturation current

<sup>d</sup> diode turn-on voltage

<sup>e</sup> interfacial barrier height

<sup>f</sup> rectification ratio

<sup>g</sup> photocurrent responsivity

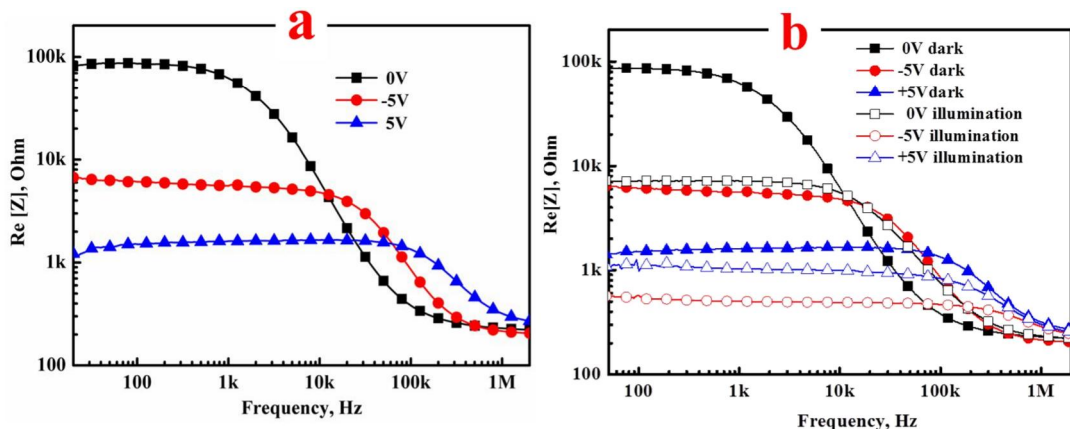
---

Figure 6.3 (d-f) displays the J-V characteristics in dark condition and with illumination for the devices with ZNR films grown at different temperatures. It is evident that all the samples show photoresponse. The charge transfer mechanism is similar to the mechanism explained in Chapter 5 (Figure 5.2). However, the photocurrent and hence the photocurrent responsivity  $R_{ph}$  (for both positive and negative bias voltages) is higher for the devices with ZNR grown at 120<sup>0</sup>C than the other temperatures. From Table 6.1, it is seen that the value of  $R_{ph}$  increased from 0.058 A/W to 11.56 A/W (200 times) under reverse bias and from 0.06 A/W to 16.28 A/W (270 times) under forward bias with the ZNR growth temperature. The  $R_{ph}$  value, for devices having ZNR films grown at 120<sup>0</sup>C, is approximately 25 times and 125 times higher than that for the devices made using ZnO nanoparticle films (Chapter 5) under forward and reverse bias voltages (at 4.5V), respectively. It can be ascribed to the lower electron-hole recombination due to the highly efficient electron transport pathways (provided by nanorods) and, hence, better charge collection at the ZNR/VOPc interface [Gonzalez-Valls and Lira-Cantu 2008].

### 6.2.6 IS measurements

To further investigate the photoresponse and the charge carrier dynamics at the hybrid heterojunctions, IS measurements were carried out for the p-n junction diode made with ZNR grown at 120<sup>0</sup>C. Figure 6.4(a) shows the resistance ( $Re[z]$ ) - frequency plots for the devices in the dark conditions.

From these plots, it is noted that the resistance of the devices reduces with increase in applied bias (both positive and negative). The resistance of the devices at 50 Hz was found to reduce from  $\sim 86k\Omega$  to  $\sim 1.48k\Omega$  in forward bias (0 to 5V) and  $\sim 87k\Omega$  to  $6.2k\Omega$  in reverse bias (0 to -5V) voltages, respectively. The ratio of resistance (absolute value) in the reverse bias to the resistance in the forward bias, which is a measure of the rectification ratio, is found to be  $\sim 4.2$ . Figure 6.4(b) shows the photoresponse of the devices under forward and reverse bias conditions. Upon illumination, it is seen that the bulk resistance of the devices drops remarkably at any given bias voltage. The resistance is found to be reduced from  $87k\Omega$  to  $7.1k\Omega$ ,  $1.5k\Omega$  to  $1k\Omega$  and  $6.2k\Omega$  to  $0.6k\Omega$  for 0V, +5V and -5V, respectively



**Figure 6.4** (a) J-V characteristics of the hybrid diode under dark for ZNR films grown at  $120^{\circ}\text{C}$  and (b) J-V characteristics of the hybrid diode in both dark and under illumination conditions. The plots in different colors represent the data for different bias voltages as indicated in the graphs.

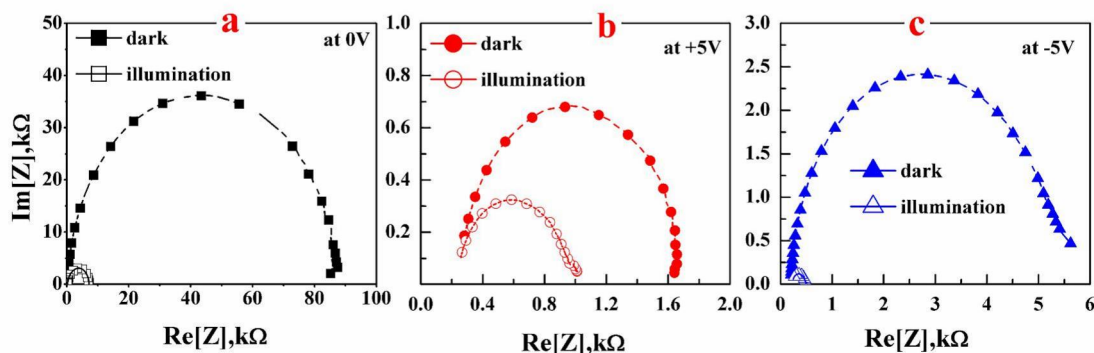


**Figure 6.5** Cole-Cole plots for the devices, made using ZNR, in both dark and illuminated conditions (a) at 0V, (b) at +5V and (c) -5V.

Figure 6.5 shows the Cole-Cole plots for the devices in dark and illuminated conditions at a given bias. For each bias voltage in the dark condition, the Cole-Cole plot displays a single semicircle, which is an indication of the predominance of a single carrier lifetime. In general, at a given bias, two semicircles are expected for a junction involving two materials. Since the bulk resistance of the ZnO film ( $< 200 \Omega$ , Chapter 4) is very small compared to the bulk resistance of VOPc ( $2 \text{ M}\Omega$ , Chapter 3), the Cole-Cole plot corresponding to ZnO film is not observed in the measured range (50Hz to 2MHz). To further analyze these Cole-Cole plots, we employed the equivalent circuit model for our devices, similar to the one shown in Figure 4.7(b) in

Chapter 4. Further, it is also observed that Cole-Cole plots deviate from perfect semicircles at very low frequencies ( $\sim 50$  Hz) in Figure 6.5 (b-c), which may be due to charge accumulation at the metal/organic interface. These charges are either injected due to higher bias voltages and/ or generated upon illumination.

**Table 6.2** Estimated parameters from IS measurements employing equivalent circuit

Parameter	at 0V		at +5V		at -5V	
	Dark	Illuminati on	Dark	Illumination	Dark	Illumination
$R_s(\Omega)^a$	209	201	210	221	161	223
$R_p(\Omega)^b$	87121	7050	1475	745	5266	264
CPE (F) <sup>c</sup>	$2.1 \times 10^{-9}$	$3.0 \times 10^{-9}$	$1.2 \times 10^{-9}$	$2.9 \times 10^{-9}$	$1.9 \times 10^{-9}$	$3.0 \times 10^{-9}$

<sup>a</sup> Series resistance <sup>c</sup>Constant phase element, which analogous to the parallel capacitance  
<sup>b</sup> Parallel resistance

In general, upon illumination, the following two processes are expected to occur : (i) the bulk resistance of the devices decrease due to the high photogenerated charge carrier density, and (ii) the capacitance of the devices increases due to photogenerated charge carriers. We also note that the radius of the semicircle (Cole-Cole plot) for the devices at any bias is found to be reduced for measurements done under illumination. This indicates a reduction in the bulk resistance under illumination. It is also observed that the capacitance of the devices increase under illumination. The values are presented in Table 6.2. Therefore, the high photocurrent and photoresponse for the devices with ZNR grown at  $120^\circ\text{C}$  can be attributed to the improved exciton dissociation at the ZNR/VOPc interface, and to better charge collection facilitated by the vertically aligned nanorods.

### 6.3 CONCLUSION

In this chapter, several hybrid diode devices, having the configuration ITO/ZNR/VOPc/MoO<sub>3</sub>/Al, were investigated for their optoelectronic properties by varying the growth temperature of ZNR films. The interface parameters such as ideality factor ( $n$ ), the Schottky barrier height ( $q\phi_B$ ) and the rectification ratio (RR) of the devices were determined from J-V characteristics. It was observed that the

---

devices with the ZNR films grown at 120°C show higher photocurrent responsivity,  $R_{ph}$ , (16.28 A/W). This value is 25 times higher than the  $R_{ph}$  value obtained for the devices made with ZnO nanoparticle films. This can be attributed to the highly crystalline vertically align nanorods that can provide better pathways for charge transport. Hence, ZNR films annealed at 120°C are suitable for organic-inorganic hybrid optoelectronic device applications.



---

## CHAPTER 7

### SUMMARY AND CONCLUSIONS

#### *Overview*

*Chapter 7 summarizes the work presented in the thesis along with the important conclusions drawn from the study. Scope for further research has been mentioned in the end.*

#### 7.1 SUMMARY

This thesis focused mainly on the investigation of the optoelectronic properties of several new organic-inorganic p-n hybrid diodes made using VOPc and ZnO. These devices were investigated with the motivation of exploiting the advantages of both organic and inorganic materials and to understand the charge carrier dynamics in such hybrid devices.

First, hole transport properties of the p-type organic VOPc thin film was investigated as a function of deposition rate. For this purpose we studied current-density voltage (J-V) characteristics, capacitance-voltage (C-V) characteristics and Impedance spectroscopy (IS). It was observed that the deposition rate of the active layer plays a crucial role in determining the electrical properties of the device. VOPc films deposited at a lower rate (0.1 Å/s) exhibited improved electrical properties compared to the films deposited at higher rates (1 Å/s and 5 Å/s). J-V characteristics indicated that charge transport is described by SCLC mechanism with an exponential distribution of traps. The estimated trap density in the devices fabricated at higher deposition rate was twice that of the device fabricated at lower deposition rates. The values of hole mobility in VOPc films were estimated, to be  $1.5 \times 10^{-7} \text{ cm}^2/\text{V-s}$ ,  $2.1 \times 10^{-8} \text{ cm}^2/\text{V-s}$  and  $1.1 \times 10^{-8} \text{ cm}^2/\text{V-s}$ , respectively, for 0.1 Å/s, 1 Å/s and 5 Å/s deposition rates. The dominant charge transport mechanism was observed to be of hopping type and follows the CBH model.

---

As the next step, electron transport properties ZnO thin films were investigated as a function of annealing temperature using J-V, C-V and IS measurements. ZnO films annealed at 350°C exhibited improved electrical properties over films annealed at other temperatures. This improvement is attributed to increased grain size and reduction in the Schottky barrier height between ITO and ZnO. J-V and IS measurements indicated that the electrical conduction in these devices is dominated by SCLC mechanism with an exponential density of traps. The DOS at Fermi level is found to be  $\sim 10^{17} \text{ eV}^{-1} \text{ cm}^{-3}$  and is almost same for all the devices. A higher electron mobility of  $1.91 \times 10^{-5} \text{ cm}^2 \text{ V}^{-1} \text{ s}^{-1}$  was achieved in the device with ZnO film annealed at 350°C.

Following the above studies, hybrid diodes were fabricated using VOPc and ZnO nanoparticle films. Their electrical properties were investigated (as a function of ZnO annealing temperature) using J-V and IS measurements. It was observed that the diodes with ZnO film annealed at 350°C show high photocurrent responsivity (470mA/W at 660nm) compared to those with ZnO films annealed at other temperatures. IS measurements suggested that the large photocurrent generated is due to the decrease in bulk resistance of the device on account of the creation of electron-hole pairs in the organic active layer when exposed to light. This higher photoresponse can also be attributed to the reduction of interfacial barrier height and efficient exciton dissociation at the VOPc/ZnO interface.

Finally, the optoelectronic properties of hybrid diodes made using VOPc and ZnO nanorods (ZNR) were investigated as a function of nanorod films growth temperature using J-V and IS measurements. It was shown that the hybrid diodes involving ZNR grown at 120°C exhibited improved photoresponse and also had high photocurrent responsivity (16.28 A/W at 660nm) compared to that in the devices with ZNR grown at other temperatures. This value is  $\sim 120$  times the  $R_{\text{ph}}$  value obtained for the devices involving ZnO nanoparticles (annealed at 350 °C).

---

## 7.2 CONCLUSIONS

The important conclusions drawn from the thesis are listed below

1. The thermally evaporated thin films of VOPc exhibited stable molecular polymorphism of Phase II. The films were polycrystalline in nature and the grain size of the films was reduced with the increase in deposition rate. The hole-only devices, with the VOPc active layer, show chemical stability up to 48 hours (current density reduced to 80%) under ambient conditions without any encapsulation. Electrical studies of these devices demonstrated that the films deposited at lower deposition rates showed better electrical properties, i.e. higher current density, electrical conductivity and charge carrier mobility. The underlying conduction mechanism in these devices was hopping type. Therefore, it can be concluded that the VOPc films deposited at lower rates are more suitable for the optoelectronic devices.
2. The sol-gel spin-coated thin films of ZnO, prepared at different annealing temperatures, showed that the size of the nanoparticles increases with increasing temperature. The nanoparticles exhibited a wurtzite hexagonal structure. The films were highly transparent (85% to 95%) to visible light. The electron-only devices with ZnO films annealed at 350<sup>0</sup>C showed better electrical properties (high current density and mobility) due to lowering of the barrier height at ITO/ZnO interface. The underlying conduction mechanism is SCLC with an exponential distribution of traps. Since they possess high optical transparency and high electron mobility, these films (annealed at 350<sup>0</sup>C) would be suitable for optoelectronic device applications.
3. The hybrid photodiodes, fabricated using films of VOPc and ZnO nanoparticles, indicated that devices made with ZnO films annealed at 350<sup>0</sup>C showed high photocurrent and photoresponse. Thus, organic-inorganic hybrid devices could work as efficient photodiodes.

- 
4. The aqueous solution grown ZNR films have shown vertically aligned hexagonal nanorod structures. The diameter and length of the nanorods increased with increase in growth temperatures. The films exhibited optical transparency greater than 80% in the visible region. This enabled higher absorption of visible light by the VOPc layer in the hybrid diode leading to efficient exciton generation. The photocurrent and photoresponse of the ZNR/VOPc photodiodes increased with the increase in ZNR growth temperatures. Thus, the ZNR/VOPc hybrid diodes have better performance than devices made of ZnO/VOPc devices.

### 7.3 SCOPE FOR FUTURE WORK

The investigations of the present research work can be extended future in the following directions.

- The role of annealing temperature on the charge transport in VOPc can be studied. One can establish the temperature dependent morphology–electrical property relation. This may be useful in understanding the charge carrier kinetics for improving the device performance.
- The influence of annealing temperature on the optoelectronic properties of VOPc/ZnO (nanoparticle and/or nanorods) hybrid interface can be studied. This may provide the less defective interface that would help in improving the device performance.
- The optoelectronic can be extended to use bulk heterojunctions forming with ZnO nanoparticles (and/or nanorods) and VOPc. This may lead to the higher exciton dissociation. This process requires precise control over the ratio of the bulk mixture to reduce the donor-acceptor islands that could hamper the charge transport. This bulk heterojunctions may improve the performance of the device.
- In the present thesis, MoO<sub>3</sub> was used as a hole injection material to assist the charge transport. This studies can be extended to use other hole injection layer

---

viz. 2,3,5,6-Tetrafluoro-7,7,8,8-tetracyanoquinodimethane (F4TCNQ), 4,4',4''-Tris[(3-methylphenyl)phenyl amino] triphenylamine (m-MTDATA), Nickel oxide (NiO), copper iodide (CuI) and vanadium oxide ( $V_2O_5$ ). This may improve the performance of the devices.



## APPENDIX

### TEMPERATURE DEPENDENT CONDUCTIVITY

The conductivity-frequency characteristics of VOPc films deposited at 0.1Å/s is shown in Figure A1. In our case, the  $s$  values were observed to decrease from 0.98 to 0.3 with the increasing temperature from 328K to 373K. Therefore, the conduction mechanism operating in these devices can be explained by employing the CBH model. The ac conductivity parameters (estimated using Eqs. 3.14, 3.15 and 3.56) are given in table A1.

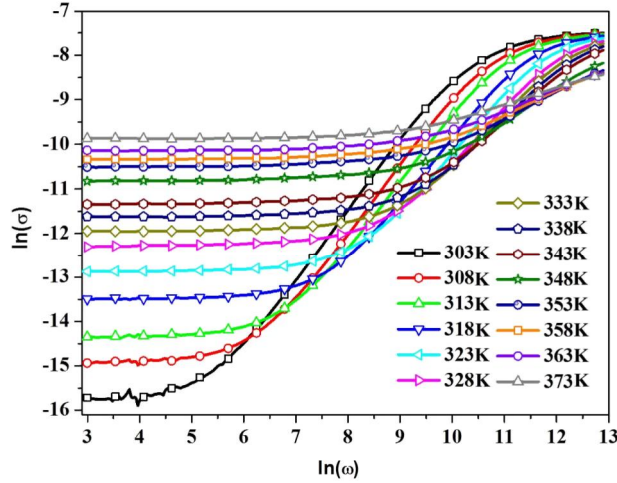


**Figure A1** Conductivity-frequency characteristics of VOPc devices deposited at 0.1 Å/s as a function of temperature

**Table A1** Estimated ac conductivity parameters at 1 kHz

T (K)	$s$	W (eV)	R (nm)	$\sigma_{ac}$ ( $\times 10^{-6}$ S/m)	$N_f$ ( $m^{-3}$ )
328	0.98	12.3	0.13	5.17	$2.0 \times 10^{30}$
333	0.97	8.35	0.19	7.02	$7.4 \times 10^{29}$
338	0.95	4.08	0.39	9.62	$1.0 \times 10^{29}$
343	0.84	1.17	1.36	12.1	$2.7 \times 10^{27}$
348	0.69	0.58	2.75	21.4	$4.3 \times 10^{26}$
353	0.52	0.38	4.18	29.2	$1.4 \times 10^{26}$
358	0.48	0.36	4.41	34.0	$1.3 \times 10^{26}$
363	0.43	0.33	4.81	40.9	$1.1 \times 10^{26}$
373	0.34	0.29	5.46	53.0	$0.8 \times 10^{26}$



---

## REFERENCES

- Abass, A.K., Collins, R.A. and Krier, A. (1993). "The influence of oxygen on the electrical properties of monoclinic lead phthalocyanine." *J. Phys. Chem. Solids*, 54 (3), 375–380.
- Abu-Hilal, A.O., Saleh, A.M. and Gould, R.D. (2005). "Effect of electrode material on AC electrical conductivity of organic zinc phthalocyanine semiconducting thin films." *Mater. Chem. Phys.*, 94 (1), 165–171.
- Ahmad, A. and Collins, R.A. (1991). "Ohmic and Space-Charge-Limited Conduction in Lead Phthalocyanine Thin Films." *Phys. Status Solidi A*, 123 (1), 201–211.
- Ahmad, A. and Collins, R.A. (1992). "The effect of oxygen on the electrical characteristics of triclinic lead phthalocyanine." *Thin Solid Films*, 217 (1–2), 75–82.
- Alam Khan, M. and Farva, U. (2017). "Elucidation of hierarchical metallophthalocyanine buffer layers in bulk heterojunction solar cells." *RSC Adv.*, 7 (19), 11304–11311.
- Al-Hartomy, O.A., Gupta, R.K., Al-Ghamdi, A.A. and Yakuphanoglu, F. (2014). "High performance organic-on-inorganic hybrid photodiodes based on organic semiconductor-graphene oxide blends." *Synth. Met.*, 195 217–221.
- Anjaneyulu, P., Sangeeth, C.S.S. and Menon, R. (2011). "Carrier density-dependent transport in poly(3-methylthiophene): from injection-limited to space-charge-limited current." *J. Phys. Appl. Phys.*, 44 (31), 315101.
- Anthopoulos, T.D. and Shafai, T. (2000). "SCLC measurements in nickel phthalocyanine thin films." *Phys. Status Solidi A*, 181 (2), 569–574.
- Anthopoulos, T.D. and Shafai, T.S. (2003a). "Alternating current conduction properties of thermally evaporated  $\alpha$ -nickel phthalocyanine thin films: Effects of oxygen doping and thermal annealing." *J. Appl. Phys.*, 94 (4), 2426–2433.

---

Anthopoulos, T.D. and Shafai, T.S. (2003b). "Alternating current conduction properties of thermally evaporated  $\alpha$ -nickel phthalocyanine thin films: Effects of oxygen doping and thermal annealing." *J. Appl. Phys.*, *94* (4), 2426–2433.

Antohe, S., Tugulea, L., Gheorghe, V., Ruxandra, V., Caplanus, I. and Ion, L. (1996). "Electrical and photovoltaic properties of ITO/chlorophyll *a*/TPyP/Al p-n junction cells." *Phys. Status Solidi A*, *153* (2), 581–588.

Arquer, F.P.G. de, Armin, A., Meredith, P. and Sargent, E.H. (2017). "Solution-processed semiconductors for next-generation photodetectors." *Nat. Rev. Mater.*, *2* (3), 100.

Azim-Araghi, M.E., Campbell, D., Krier, A. and Collins, R.A. (1996). "Electrical conduction mechanisms in thermally evaporated lead phthalocyanine thin films." *Semicond. Sci. Technol.*, *11* (1), 39.

Azim-Araghi, M.E., Krier, A. and Abass, A.K. (1997). "Electrical behaviour of thermally evaporated chloroaluminium phthalocyanine." *Semicond. Sci. Technol.*, *12* (12), 1625.

Bakulin, A.A., Dimitrov, S.D., Rao, A., Chow, P.C.Y., Nielsen, C.B., Schroeder, B.C., McCulloch, I., Bakker, H.J., Durrant, J.R. and Friend, R.H. (2013). "Charge-Transfer State Dynamics Following Hole and Electron Transfer in Organic Photovoltaic Devices." *J. Phys. Chem. Lett.*, *4* (1), 209–215.

Bao, Z., Lovinger, A.J. and Dodabalapur, A. (1997). "Highly ordered vacuum-deposited thin films of metallophthalocyanines and their applications in field-effect transistors." *Adv. Mater.*, *9* (1), 42–44.

Barea, E.M., Garcia-Belmonte, G., Sommer, M., Hüttner, S., Bolink, H.J. and Thelakkat, M. (2010). "Determination of charge carrier mobility of hole transporting polytriarylamine-based diodes." *Thin Solid Films*, *518* (12), 3351–3354.

---

Barkhalov, B.S. and Vidadi, Y.A. (1977). "Properties of Al(copper phthalocyanine)Ag diode structures with Schottky barriers." *Thin Solid Films*, 40 L5–L8.

Beek, W.J., Wienk, M.M. and Janssen, R.A. (2006). "Hybrid solar cells from regioregular polythiophene and ZnO nanoparticles." *Adv. Funct. Mater.*, 16 (8), 1112–1116.

Bi-Xin, L., Jiang-Shan, C., Yong-Biao, Z. and Dong-Ge, M. (2011). "Frequency-Dependent Electrical Transport Properties of 4, 4', 4"-Tri( N -carbazolyl)-Triphenylamine Investigated by Impedance Spectroscopy." *Chin. Phys. Lett.*, 28 (5), 057201.

Blakesley, J.C., Castro, F.A., Kylberg, W., Dibb, G.F.A., Arantes, C., Valaski, R., Cremona, M., Kim, J.S. and Kim, J.-S. (2014). "Towards reliable charge-mobility benchmark measurements for organic semiconductors." *Org. Electron.*, 15 (6), 1263–1272.

Braik, M., Dridi, C., Ben Ali, M., Ali, A., Abbas, M.N. and Errachid, A. (2015). "Investigation of structural, optical and electrical properties of a new cobalt phthalocyanine thin films with potential applications in perchlorate sensor." *Synth. Met.*, 209 135–142.

Braun, A. and Tcherniac, J. (1907). "Über die Produkte der Einwirkung von Acetanhydrid auf Phthalamid." *Berichte Dtsch. Chem. Ges.*, 40 (2), 2709–2714.

Braun, C.L. (1984). "Electric field assisted dissociation of charge transfer states as a mechanism of photocarrier production." *J. Chem. Phys.*, 80 (9), 4157–4161.

Brückner, W., Moldenhauer, W. and Hinz, D. (1980). "Thermal breakdown in ZnO-varistor ceramics." *Phys. Status Solidi A*, 59 (2), 713–718.

Brütting, W. (2005a). Introduction to the Physics of Organic Semiconductors. In *Physics of Organic Semiconductors*, W. Brütting, ed. (Wiley-VCH Verlag GmbH & Co. KGaA), pp 1–14.

---

Brütting, W. (2005b). Introduction to the Physics of Organic Semiconductors. In *Physics of Organic Semiconductors*, W. Brütting, ed. (Wiley-VCH Verlag GmbH & Co. KGaA), pp 1–14.

Brütting, W., Berleb, S. and Mückl, A.G. (2001). "Device physics of organic light-emitting diodes based on molecular materials." *Org. Electron.*, 2 (1), 1–36.

Byrne, G.T., Linstead, R.P. and Lowe, A.R. (1934). "213. Phthalocyanines. Part II. The preparation of phthalocyanine and some metallic derivatives from o-cyanobenzamide and phthalimide." *J. Chem. Soc. Resumed*, 0 (0), 1017–1022.

Cai, X., Zhang, Y., Qi, D. and Jiang, J. (2009). "Density functional theory study on the semiconducting properties of metal phthalocyanine compounds: effect of axially coordinated ligand." *J. Phys. Chem. A*, 113 (11), 2500–2506.

Can Ömür, B., Can, N. and Altındal, A. (2017). "Conduction and dielectric relaxation studies on substituted iron(II) phthalocyanine thin film." *Mater. Chem. Phys.*, 186 438–445.

Cao, W. and Xue, J. (2014). "Recent progress in organic photovoltaics: device architecture and optical design." *Energy Environ. Sci.*, 7 (7), 2123–2144.

Carotta, M.C., Cervi, A., Natale, V. di, Gherardi, S., Giberti, A., Guidi, V., Puzzovio, D., Vendemiati, B., Martinelli, G., Sacerdoti, M., Calestani, D., Zappettini, A., Zha, M. and Zanotti, L. (2009). "ZnO gas sensors: A comparison between nanoparticles and nanotetrapods-based thick films." *Sens. Actuators B Chem.*, 137 (1), 164–169.

Chen, D., Yao, B., Fan, G., Lv, W., Gao, P. (2013). "Influence of donor-acceptor layer sequence on photoresponsive organic field-effect transistors based on palladium phthalocyanine and C60." *Appl. Phys. Lett.*, 102 (16), 72.

Chung, D.S., Lee, D.H., Yang, C., Hong, K., Park, C.E., Park, J.W. and Kwon, S.-K. (2008). "Origin of high mobility within an amorphous polymeric semiconductor: Space-charge-limited current and trap distribution." *Appl. Phys. Lett.*, 93 (3), 033303.

---

Collins, R.A. and Mohammed, K.A. (1986). "Electrical, structural and gas sensing properties of zinc phthalocyanine thin films." *Thin Solid Films*, 145 (1), 133–145.

Coropceanu, V., Cornil, J., Silva Filho, D.A. da, Olivier, Y., Silbey, R. and Brédas, J.-L. (2007). "Charge Transport in Organic Semiconductors." *Chem. Rev.*, 107 (4), 926–952.

Cullity, B.D. (1956). "Elements Of X Ray Diffraction (Addison-Wesley Publishing Company, Inc.).

Darwish, A.A.A., El-Shazly, E.A.A., Attia, A.A. and El-Rahman, K.A. (2016). "Dark electrical properties and photovoltaic performance of organic/inorganic (SnPcCl<sub>2</sub>)." *J. Mater. Sci. Mater. Electron.*, 27 (8), 8786–8792.

Darwish, S., Riad, A.S. and Soliman, H.S. (1996). "Electrical conductivity and the effect of temperature on photoconduction of n-ZnSe/p-Si rectifying heterojunction cells." *Semicond. Sci. Technol.*, 11 (1), 96.

Dearden, C.A., Walker, M., Beaumont, N., Hancox, I., Unsworth, N.K., Sullivan, P., McConville, C.F. and Jones, T.S. (2014). "High voltage hybrid organic photovoltaics using a zinc oxide acceptor and a subphthalocyanine donor." *Phys. Chem. Chem. Phys. PCCP*, 16 (35), 18926–18932.

Delacote, G.M., Fillard, J.P. and Marco, F.J. (1964). "Electron injection in thin films of copper phthalocyanine." *Solid State Commun.*, 2 (12), 373–376.

Dent, C.E. and Linstead, R.P. (1934). "215. Phthalocyanines. Part IV. Copper phthalocyanines." *J. Chem. Soc. Resumed*, 0 (0), 1027–1031.

Dent, C.E., Linstead, R.P. and Lowe, A.R. (1934). "217. Phthalocyanines. Part VI. The structure of the phthalocyanines." *J. Chem. Soc. Resumed*, 0 (0), 1033–1039.

Dey, A., Layek, A., Roychowdhury, A., Das, M., Datta, J., Middy, S., Das, D. and Ray, P.P. (2015). "Investigation of charge transport properties in less defective nanostructured ZnO based Schottky diode." *RSC Adv.*, 5 (46), 36560–36567.

---

Dhanya, I. and Menon, C.S. (2012). "Surface morphological, structural, electrical and optical properties of annealed vanadyl tetra tert-butyl 2, 3 naphthalocyanine thin films." *Vacuum*, 86 (9), 1289–1295.

Diesbach, H. de and Weid, E. von der (1927). "Quelques sels complexes des o-dinitriles avec le cuivre et la pyridine." *Helv. Chim. Acta*, 10 (1), 886–888.

Djurišić, A.B., Kwong, C.Y., Chui, P.C. and Chan, W.K. (2003). "Indium–tin–oxide surface treatments: Influence on the performance of CuPc/C60 solar cells." *J. Appl. Phys.*, 93 (9), 5472–5479.

Efafi, B., Ghamsari, M.S., Aberoumand, M.A., Ara, M.H.M., Ghamsari, A.H.S. and Rad, H.H. (2014). "Aluminum doped ZnO sol–gel derived nanocrystals: Raman spectroscopy and solid solubility characterization." *Phys. Status Solidi A*, 211 (10), 2426–2430.

Eley, D.D. (1948). "Phthalocyanines as semiconductors." *Nature*, 162 (4125), 819.

Elliott, S.R. (1977). "A theory of ac conduction in chalcogenide glasses." *Philos. Mag.*, 36 (6), 1291–1304.

El-Nahass, M.M., Abd-El-Rahman, K.F. and Darwish, A.A.A. (2007). "Fabrication and electrical characterization of p-NiPc/n-Si heterojunction." *Microelectron. J.*, 38 (1), 91–95.

El-Nahass, M.M., Farid, A.M., Farag, A.A.M. and Ali, H.A.M. (2006). "Carrier transport mechanisms and photovoltaic characteristics of pH 2 Pc/n-Si heterojunctions." *Vacuum*, 81 (1), 8–12.

Esro, M., Vourlias, G., Somerton, C., Milne, W.I. and Adamopoulos, G. (2015). "High-Mobility ZnO Thin Film Transistors Based on Solution-processed Hafnium Oxide Gate Dielectrics." *Adv. Funct. Mater.*, 25 (1), 134–141.

---

Fan, F. and Faulkner, L.R. (1978a). "Photovoltaic effects of metalfree and zinc phthalocyanines. I. Dark electrical properties of rectifying cells." *J. Chem. Phys.*, *69* (7), 3334–3340.

Fan, F. and Faulkner, L.R. (1978b). "Photovoltaic effects of metalfree and zinc phthalocyanines. II. Properties of illuminated thin-film cells." *J. Chem. Phys.*, *69* (7), 3341–3349.

Feron, K., Belcher, W.J., Fell, C.J. and Dastoor, P.C. (2012). "Organic Solar Cells: Understanding the Role of Förster Resonance Energy Transfer." *Int. J. Mol. Sci.*, *13* (12), 17019–17047.

Fujimoto, T., Matsushita, M.M. and Awaga, K. (2013). "Ambipolar carrier injections governed by electrochemical potentials of ionic liquids in electric-double-layer thin-film transistors of lead-and titanyl-phthalocyanine." *J. Phys. Chem. C*, *117* (11), 5552–5557.

Gao, F. and Inganäs, O. (2014). "Charge generation in polymer–fullerene bulk-heterojunction solar cells." *Phys. Chem. Chem. Phys.*, *16* (38), 20291–20304.

Gao, X. and Zhao, Z. (2015). "High mobility organic semiconductors for field-effect transistors." *Sci. China Chem.*, *58* (6), 947–968.

Ghosh, A. and Pan, A. (2000). "Scaling of the conductivity spectra in ionic glasses: dependence on the structure." *Phys. Rev. Lett.*, *84* (10), 2188.

Gonzalez-Valls, I. and Lira-Cantu, M. (2008). "Vertically-aligned nanostructures of ZnO for excitonic solar cells: a review." *Energy Environ. Sci.*, *2* (1), 19–34.

Gould, R.D. (1985). "D.C. electrical measurements on evaporated thin films of copper phthalocyanine." *Thin Solid Films*, *125* (1), 63–69.

Gould, R.D. (1986). "Dependence of the mobility and trap concentration in evaporated copper phthalocyanine thin films on background pressure and evaporation rate." *J. Phys. Appl. Phys.*, *19* (9), 1785.

---

Gould, R.D. (1996a). "Structure and electrical conduction properties of phthalocyanine thin films." *Coord. Chem. Rev.*, 156 237–274.

Gould, R.D. (1996b). "Structure and electrical conduction properties of phthalocyanine thin films." *Coord. Chem. Rev.*, 156 237–274.

Gould, R.D. and Blyth, R.I.R. (1990). "Conductivity and absorption measurements in nickel phthalocyanine thin films." *Phys. Status Solidi A*, 120 (1), .

Gould, R.D. and Hassan, A.K. (1990). "High field electronic conduction processes in copper phthalocyanine thin films using lead and gold electrode combinations." *Thin Solid Films*, 193 895–904.

Gould, R.D. and Rahman, M.S. (1981). "Power-law currents in some ZnO-Sn composite materials." *J. Phys. Appl. Phys.*, 14 (1), 79.

Greiner, M.T., Chai, L., Helander, M.G., Tang, W.-M. and Lu, Z.-H. (2013a). "Metal/Metal-Oxide Interfaces: How Metal Contacts Affect the Work Function and Band Structure of MoO<sub>3</sub>." *Adv. Funct. Mater.*, 23 (2), 215–226.

Greiner, M.T., Chai, L., Helander, M.G., Tang, W.-M. and Lu, Z.-H. (2013b). "Metal/metal-oxide interfaces: how metal contacts affect the work function and band structure of MoO<sub>3</sub>." *Adv. Funct. Mater.*, 23 (2), 215–226.

Griffiths, C.H., Walker, M.S. and Goldstein, P. (1976). "Polymorphism in Vanadyl Phthalocyanine." *Mol. Cryst. Liq. Cryst.*, 33 (1–2), 149–170.

Gu, W., Hu, Y., Zhu, Z., Liu, N., Zhang, J. and Wang, J. (2013). "Preparing highly ordered copper phthalocyanine thin-film by controlling the thickness of the modified layer and its application in organic transistors." *Solid-State Electron.*, 89 101–104.

Guerrero, A., Marchesi, L.F., Boix, P.P., Ruiz-Raga, S., Ripolles-Sanchis, T., Garcia-Belmonte, G. and Bisquert, J. (2012). "How the Charge-Neutrality Level of Interface States Controls Energy Level Alignment in Cathode Contacts of Organic Bulk-Heterojunction Solar Cells." *ACS Nano*, 6 (4), 3453–3460.

---

Gupta, R.K., Yakuphanoglu, F., Ghosh, K. and Kahol, P.K. (2011a). "Fabrication and characterization of p–n junctions based on ZnO and CuPc." *Microelectron. Eng.*, 88 (10), 3067–3069.

Gupta, R.K., Yakuphanoglu, F., Ghosh, K. and Kahol, P.K. (2011b). "Fabrication and characterization of p–n junctions based on ZnO and CuPc." *Microelectron. Eng.*, 88 (10), 3067–3069.

Habas, S.E., Platt, H.A.S., Hest, M.F.A.M. van and Ginley, D.S. (2010). "Low-Cost Inorganic Solar Cells: From Ink To Printed Device." *Chem. Rev.*, 110 (11), 6571–6594.

Hassan, A.K. and Gould, R.D. (1989). "The effects of exposure to oxygen and annealing on the conductivity of copper phthalocyanine thin films." *J. Phys. Condens. Matter*, 1 (37), 6679.

Hassan, A.K. and Gould, R.D. (1990). "Asymmetric electrical conductivity in oxygen-doped thin films of copper phthalocyanine, using gold and aluminium electrodes." *Int. J. Electron. Theor. Exp.*, 69 (1), 11–17.

Hassan, A.K. and Gould, R.D. (1992). "Space-charge-limited conductivity and trapping mode diagnosis in thin films of nickel phthalocyanine." *Int. J. Electron.*, 73 (5), 1047–1049.

Heilmeyer, G.H. and Warfield, G. (1963). "Investigation of Bulk Currents in Metal-Free Phthalocyanine Crystals." *J. Chem. Phys.*, 38 (1), 163–168.

Henni, A., Merrouche, A., Telli, L. and Karar, A. (2016). "Studies on the structural, morphological, optical and electrical properties of Al-doped ZnO nanorods prepared by electrochemical deposition." *J. Electroanal. Chem.*, 763 149–154.

Hooper, P.D., Newton, M.I., McHale, G. and Willis, M.R. (1997). "Electrical properties of nickel phthalocyanine (NiPc) sandwich devices incorporating a tetracyanoquinodimethane (TCNQ) layer." *Semicond. Sci. Technol.*, 12 (4), 455.

---

Hu, Y., Yin, J., Kadali, C. and Ju, X.-H. (2016). "Theoretical Investigation on Charge Transfer Properties of 1,3,5-Tripyrrolebenzene (TPB) and its Derivatives with Electron-withdrawing Substituents." *Croat. Chem. Acta*, 89.

Hussain, A., Akhter, P., Bhatti, A.S., Shah, A.A. and Bilal, S. (2010). "Dominant conduction mechanism and the effects of device temperature on electrical characteristics of Al/ZnPc/n-Si structures." *Vacuum*, 84 (7), 975–979.

Ishii, H., Sugiyama, K., Ito, E. and Seki, K. (1999). "Energy Level Alignment and Interfacial Electronic Structures at Organic/Metal and Organic/Organic Interfaces." *Adv. Mater.*, 11 (8), 605–625.

Jarosz, G. (2010). "On small signal capacitance spectra of organic diode formed by ITO–palladium phthalocyanine–Al sandwich system." *Thin Solid Films*, 518 (14), 4015–4018.

J. Bolink, H., Brine, H., Coronado, E. and Sessolo, M. (2010). "Hybrid organic-inorganic light emitting diodes: effect of the metal oxide." *J. Mater. Chem.*, 20 (20), 4047–4049.

Jin, F., Chu, B., Li, W., Su, Z., Yan, X., Wang, J., Li, R., Zhao, B., Zhang, T., Gao, Y., Lee, C.S., Wu, H., Hou, F., Lin, T. and Song, Q. (2014). "Highly efficient organic tandem solar cell based on SubPc:C70 bulk heterojunction." *Org. Electron.*, 15 (12), 3756–3760.

Jin, M.-J., Jo, J. and Yoo, J.-W. (2015). "Impedance spectroscopy analysis on the effects of TiO<sub>2</sub> interfacial atomic layers in ZnO nanorod polymer solar cells: Effects of interfacial charge extraction on diffusion and recombination." *ResearchGate*, 19.

J. Ramadan, A., A. Rochford, L., Moffat, J., Mulcahy, C., P. Ryan, M., S. Jones, T. and Heutz, S. (2016). "The morphology and structure of vanadyl phthalocyanine thin films on lithium niobate single crystals." *J. Mater. Chem. C*, 4 (2), 348–351.

Kalia, S., Mahajan, A., Neerja, Sharma, A.K., Kumar, S., Bedi, R.K., Shekhawat, M.S., Bhardwaj, S. and Suthar, B. (2016). "Dielectric studies of boron sub

---

phthalocyanine chloride thin films by admittance spectroscopic techniques." *AIP Conf. Proc.*, 1728 (1), 020277.

Kärber, E., Raadik, T., Dedova, T., Krustok, J., Mere, A., Mikli, V. and Krunks, M. (2011). "Photoluminescence of spray pyrolysis deposited ZnO nanorods." *Nanoscale Res. Lett.*, 6 359.

Kerp, H.R. and Van Faassen, E.E. (2000). "Effects of oxygen on exciton transport in zinc phthalocyanine layers." *Chem. Phys. Lett.*, 332 (1), 5–12.

Kettle, J., Chang, S.-W. and Horie, M. (2015). "Fabrication and characterisation of hybrid photodiodes based on PCPDTBT–ZnO active layers." *Microelectron. Eng.*, 146 105–108.

Khan, S.M., Sayyad, M.H. and Karimov, K.S. (2011). "Investigation of temperature-dependent electrical properties of p-VOPc/n-si heterojunction under dark conditions." *Ionics*, 17 (4), 307–313.

Kidowaki, H., Oku, T. and Akiyama, T. (2012). "Fabrication and characterization of CuO/ZnO solar cells." *J. Phys. Conf. Ser.*, 352 (1), 012022.

Kim, J. and Yim, S. (2011). "Influence of surface morphology evolution of SubPc layers on the performance of SubPc/C60 organic photovoltaic cells." *Appl. Phys. Lett.*, 99 (19), 193303.

Kippelen, B. and Brédas, J.-L. (2009). "Organic photovoltaics." *Energy Environ. Sci.*, 2 (3), 251–261.

Kiran, M.R., Ulla, H., Fernandes, J.M., Satyanarayan, M.N. and Umesh., G. (2015a). "Electrical Characterization of Hybrid Hetero Interface using n-ZnO and p-CuPc." *Mater. Today Proc.*, 2 (4), 1230–1233.

Kiran, M.R., Ulla, H., Krishnamanohara, Satyanarayan, M.N. and Umesh, G. (2015b). "Investigation of charge transport in Vanadyl-phthalocyanine with molybdenum

---

trioxide as a buffer layer: Impedance spectroscopic analysis." *Synth. Met.*, 210, Part B 208–213.

Kiran, M.R., Ulla, H., Satyanarayan, M.N. and Umesh, G. (2017). "Effect of deposition rate on the charge transport in Vanadyl-phthalocyanine thin films." *Synth. Met.*, 224 63–71.

Kiran, M.R., Ulla, H., Satyanarayan, M.N., Umesh, G. and others (2015c). "Investigation of charge transport in Vanadyl-phthalocyanine with molybdenum trioxide as a buffer layer: Impedance spectroscopic analysis." *Synth. Met.*, 210 208–213.

Köhler, A. and Bässler, H. (2015). The Electronic Structure of Organic Semiconductors. In *Electronic Processes in Organic Semiconductors*, (Wiley-VCH Verlag GmbH & Co. KGaA), pp 1–86.

Kovacik, P., Assender, H.E. and Watt, A.A.R. (2013). "Morphology control in co-evaporated bulk heterojunction solar cells." *Sol. Energy Mater. Sol. Cells*, 117 22–28.

Kroger, M., Hamwi, S., Meyer, J., Riedl, T., Kowalsky, W. and Kahn, A. (2009). "Role of the deep-lying electronic states of MoO<sub>3</sub> in the enhancement of hole-injection in organic thin films." *Appl. Phys. Lett.*, 95 (12), 123301.

Kumar and Pankaj (2017). "Organic solar cells: device physics, processing, degradation, and prevention (CRC Press, Taylor & Francis Group).

Kumar, R., Khare, N., Kumar, V., Bhalla, G.L., Srivastava, R., Chauhan, G. and Kamalasanan, M.N. (2009). "Fabrication and current–voltage characteristics of ZnO/ $\alpha$ -NPD based inorganic–organic hybrid structure." *Semicond. Sci. Technol.*, 24 (4), 045020.

Lee, C.-T., Yu, Q.-X., Tang, B.-T., Lee, H.-Y. and Hwang, F.-T. (2001). "Investigation of indium tin oxide/zinc oxide multilayer ohmic contacts to n-type GaN isotype conjunction." *Appl. Phys. Lett.*, 78 (22), 3412–3414.

---

Lee, K.H., Park, C.H., Lee, K., Ha, T., Kim, J.H., Yun, J., Lee, G.-H. and Im, S. (2011). "Semi-transparent organic/inorganic hybrid photo-detector using pentacene/ZnO diode connected to pentacene transistor." *Org. Electron.*, *12* (7), 1103–1107.

Lee, S.-H., Han, S.-H., Jung, H.S., Shin, H., Lee, J., Noh, J.-H., Lee, S., Cho, I.-S., Lee, J.-K., Kim, J. and Shin, H. (2010). "Al-Doped ZnO Thin Film: A New Transparent Conducting Layer for ZnO Nanowire-Based Dye-Sensitized Solar Cells." *J. Phys. Chem. C*, *114* (15), 7185–7189.

Levinson, L.M., Castleberry, D.E. and Becker, C.A. (1982). "ZnO varistors for liquid crystal displays." *J. Appl. Phys.*, *53* (5), 3859–3864.

Li, L., Tang, Q., Li, H., Yang, X., Hu, W., Song, Y., Shuai, Z., Xu, W., Liu, Y. and Zhu, D. (2007). "An Ultra Closely  $\pi$ -Stacked Organic Semiconductor for High Performance Field-Effect Transistors." *Adv. Mater.*, *19* (18), 2613–2617.

Linstead, R.P. (1934). "212. Phthalocyanines. Part I. A new type of synthetic colouring matters." *J. Chem. Soc. Resumed*, *0* (0), 1016–1017.

Linstead, R.P. and Lowe, A.R. (1934a). "214. Phthalocyanines. Part III. Preliminary experiments on the preparation of phthalocyanines from phthalonitrile." *J. Chem. Soc. Resumed*, *0* (0), 1022–1027.

Linstead, R.P. and Lowe, A.R. (1934b). "216. Phthalocyanines. Part V. The molecular weight of magnesium phthalocyanine." *J. Chem. Soc. Resumed*, *0* (0), 1031–1033.

Liu, Y., Liu, A., Hu, Z., Liu, W. and Qiao, F. (2012). "Impedance spectroscopy studies on CuPc/n-Si hybrid solar cell." *J. Phys. Chem. Solids*, *73* (5), 626–629.

Loutfy, R.O. and Sharp, J.H. (1979). "Photovoltaic properties of metal-free phthalocyanines. I. Al/H<sub>2</sub>Pc Schottky barrier solar cells." *J. Chem. Phys.*, *71* (3), 1211–1217.

---

M, P. and H.E, S. (1999). "Electronic processes in organic crystals and polymers (OUP).

Ma, W., Yu, J., Yuan, Z. and Jiang, Y. (2011). "Photodiode Based on ZnO Nanorod/CuPc Hybrid." *Integr. Ferroelectr.*, 128 (1), 149–154.

Macdonald, J.R. (1992). "Impedance spectroscopy." *Ann. Biomed. Eng.*, 20 (3), 289–305.

Mali, S.S., Kim, H., Kim, J.H., Patil, P.S. and Kook Hong, C. (2014). "Synthesis and characterization of planar heterojunction hybrid polymer solar cells based on copper phthalocyanine (CuPc) and titanium dioxide." *Ceram. Int.*, 40 (1, Part A), 643–649.

Mansour, S.O., Louati, B. and Guidara, K. (2015). "AC conductivity and dielectric behavior of high-temperature form of copper silver phosphate." *Ionics*, 21 (7), 1973–1982.

Martens, H.C.F., Brom, H.B. and Blom, P.W.M. (1999). "Frequency-dependent electrical response of holes in poly (p-phenylene vinylene)." *Phys. Rev. B*, 60 (12), R8489.

Martens, H.C.F., Huijberts, J.N. and Blom, P.W.M. (2000). "Simultaneous measurement of electron and hole mobilities in polymer light-emitting diodes." *Appl. Phys. Lett.*, 77 (12), 1852–1854.

Mathew, J.P., Varghese, G. and Mathew, J. (2012). "Effect of post-thermal annealing on the structural and optical properties of ZnO thin films prepared from a polymer precursor." *Chin. Phys. B*, 21 (7), 078104.

Mayes, K., Yasan, A., McClintock, R., Shiell, D., Darvish, S.R., Kung, P. and Razeghi, M. (2004). "High-power 280 nm AlGaIn light-emitting diodes based on an asymmetric single-quantum well." *Appl. Phys. Lett.*, 84 (7), 1046–1048.

McHale, G., Newton, M.I., Hooper, P.D. and Willis, M.R. (1996). "Nickel phthalocyanine photovoltaic devices." *Opt. Mater.*, 6 (1–2), 89–92.

---

Menke, S.M. and Holmes, R.J. (2014). "Exciton diffusion in organic photovoltaic cells." *Energy Environ. Sci.*, 7 (2), 499–512.

Middya, S., Layek, A., Dey, A., Datta, J., Das, M., Banerjee, C. and Ray, P.P. (2014). "Role of zinc oxide nanomorphology on Schottky diode properties." *Chem. Phys. Lett.*, 610 39–44.

Mikhnenko, O.V., Blom, P.W.M. and Nguyen, T.-Q. (2015). "Exciton diffusion in organic semiconductors." *Energy Environ. Sci.*, 8 (7), 1867–1888.

Moliton, A. and Nunzi, J.-M. (2006). "How to model the behaviour of organic photovoltaic cells." *Polym. Int.*, 55 (6), 583–600.

Murtaza, I., Karimov, K.S., Sayyad, M.H. and Qazi, I. (2012). Optoelectronic properties of vanadyl Phthalocyanine based organic-inorganic hybrid devices. In *Applied Mechanics and Materials*, (Trans Tech Publ), pp 3255–3260.

Murtaza, I., Qazi, I., Karimov, K.S. and Sayyad, M.H. (2011). "Impedance spectroscopic studies of an organic semiconductor device incorporating a thin film of highly doped ZnPc with MoO<sub>3</sub>." *Phys. B Condens. Matter*, 406 (6–7), 1238–1241.

Nath, D., Dey, P., Deb, D., Rakshit, J.K. and Roy, J.N. (2017). "Fabrication and characterization of organic semiconductor based photodetector for optical communication." *CSI Trans. ICT*, 5 (2), 149–160.

Nowy, S., Ren, W., Wagner, J., Weber, J.A. and Brütting, W. (2009). Impedance spectroscopy of organic hetero-layer OLEDs as a probe for charge carrier injection and device degradation. p 74150G–74150G–12.

Ohta, H., Kambayashi, T., Hirano, M., Hoshi, H., Ishikawa, K., Takezoe, H. and Hosono, H. (2003). "Application of a Transparent Conductive Substrate with an Atomically Flat and Stepped Surface to Lateral Growth of an Organic Molecule: Vanadyl Phthalocyanine." *Adv. Mater.*, 15 (15), 1258–1262.

---

Ong, B.S., Li, C., Li, Y., Wu, Y. and Loutfy, R. (2007). "Stable, Solution-Processed, High-Mobility ZnO Thin-Film Transistors." *J. Am. Chem. Soc.*, 129 (10), 2750–2751.

Ostroverkhova, O. (2016). "Organic Optoelectronic Materials: Mechanisms and Applications." *Chem. Rev.*, 116 (22), 13279–13412.

Ouyang, M., Bai, R., Yang, L., Chen, Q., Han, Y., Wang, M., Yang and Chen, H. (2008). "High Photoconductive Vertically Oriented TiO<sub>2</sub> Nanotube Arrays and Their Composites with Copper Phthalocyanine." *J. Phys. Chem. C*, 112 (7), 2343–2348.

Pan, F., Tian, H., Qian, X., Huang, L., Geng, Y. and Yan, D. (2011). "High performance vanadyl phthalocyanine thin-film transistors based on fluorobenzene end-capped quaterthiophene as the inducing layer." *Org. Electron.*, 12 (8), 1358–1363.

Pan, Y., Liao, X., Wu, Y., Chen, L., Zhao, Y., Shen, Y., Li, F., Shen, S. and Huang, D. (1998a). "Steady-state photovoltaic and electroreflective spectra in Al/vanadyl phthalocyanine (VOPc, in phase II)/indium–tin–oxide (ITO) sandwich cell." *Thin Solid Films*, 324 (1–2), 209–213.

Pan, Y.L., Wu, Y.J., Chen, L.B., Zhao, Y.Y., Shen, Y.H., Li, F.M., Shen, S.Y. and Huang, D.H. (1998b). "Structure and spectroscopic characterization of polycrystalline vanadyl phthalocyanine (VOPc) films fabricated by vacuum deposition." *Appl. Phys. Mater. Sci. Process.*, 66 (5), 569–573.

Pankove, J.I. and Physics (2010). "Optical Processes in Semiconductors (Dover Publications).

Patil, S.L., Chougule, M.A., Pawar, S.G., Raut, B.T., Sen, S. and Patil, V.B. (2011). "New process for synthesis of ZnO thin films: Microstructural, optical and electrical characterization." *J. Alloys Compd.*, 509 (41), 10055–10061.

Pickett, A., Mohapatra, A., Laudari, A., Khanra, S., Ram, T., Patil, S. and Guha, S. (2017). "Hybrid ZnO-organic semiconductor interfaces in photodetectors: A

---

comparison of two near-infrared donor-acceptor copolymers." *Org. Electron.*, *45* 115–123.

Popielarski, P., Bala, W., Paprocki, K., Mosinska, L., Kowalska, M., Szybowicz, M. and Makowiecki, J. (2013). "Admittance spectroscopy of CuPC-Si and CoPC-Si heterostructures." *Electrochimica Acta*, *104* 496–504.

Rajesh, K.R. and Menon, C.S. (2005). "Electrical and optical properties of vacuum deposited ZnPc and CoPc thin films and application of variable range hopping model."

Rajesh, K.R. and Menon, C.S. (2014). Polymeric gated organic field effect transistor using magnesium phthalocyanine. In SPIE Organic Photonics+ Electronics, (International Society for Optics and Photonics), pp 918515–918515.

Ramar, M., Tyagi, P., Suman, C.K. and Srivastava, R. (2014). "Enhanced carrier transport in tris(8-hydroxyquinolate) aluminum by titanyl phthalocyanine doping." *RSC Adv.*, *4* (93), 51256–51261.

Ramar, M., Yadav, V., Srivastava, R. and Suman, C.K. (2015). "Effect of titanyl phthalocyanine doping on opto-electrical properties of Alq3 thin films." *J. Mater. Sci. Mater. Electron.*, *26* (9), 7165–7173.

Rand, B.P., Genoe, J., Heremans, P. and Poortmans, J. (2007). "Solar cells utilizing small molecular weight organic semiconductors." *Prog. Photovolt. Res. Appl.*, *15* (8), 659–676.

Rasool, K., Rafiq, M.A., Ahmad, M., Imran, Z., Batool, S.S., Nazir, A., Durrani, Z. a. K. and Hasan, M.M. (2015). "Charge injection and trapping in TiO<sub>2</sub> nanoparticles decorated silicon nanowires arrays." *Appl. Phys. Lett.*, *106* (7), 073101.

Ray, A.K., Tracey, S.M. and Hodgson, S.N.B. (2001). "Photoelectric Measurements on Chloroaluminium Phthalocyanine/Titanium Oxide Heterojunctions." *J. Sol-Gel Sci. Technol.*, *22* (1–2), 15–22.

---

Reddy, V.S., Das, S., Ray, S.K. and Dhar, A. (2007). "Studies on conduction mechanisms of pentacene based diodes using impedance spectroscopy." *J. Phys. Appl. Phys.*, 40 (24), 7687.

Reis, F.T., Mencaraglia, D., Saad, S.O., Seguy, I., Oukachmih, M., Jolinet, P. and Destruel, P. (2004). "Electrical characterization of ITO/CuPc/Al diodes using temperature dependent capacitance spectroscopy and I–V measurements." *J. Non-Cryst. Solids*, 338 599–602.

Riad, A.S. (1999). "Influence of dioxygen and annealing process on the transport properties of nickel phthalocyanine Schottky-barrier devices." *Phys. B Condens. Matter*, 270 (1), 148–156.

Riad, S. (2000). "Dark and photoelectric conversion properties of p-MgPc/n-Si (Organic/Inorganic) heterojunction cells." *Thin Solid Films*, 370 (1), 253–257.

Rouis, A., Dridi, C., Dumazet-Bonnamour, I., Davenas, J. and Ben Ouada, H. (2007). "Transport mechanism and trap distribution in ITO/azo-calix[4]arene derivative/Al diode structure." *Phys. B Condens. Matter*, 399 (2), 109–115.

Roy, M.S., Balraju, P., Deol, Y.S., Mishra, R.K., Choudhary, V.S. and Sharma, G.D. (2008). "Charge transportation and photo generation process in polythiophene functionalized with tin (II) phthalocyanine (SnPc-PT) thin film." *Sol. Energy Mater. Sol. Cells*, 92 (11), 1516–1525.

Şahin, M., Durmuş, H. and Kaplan, R. (2006). "Current–voltage analysis of a-Si:H Schottky diodes." *Appl. Surf. Sci.*, 252 (18), 6269–6274.

Sakurai, T., Ohashi, T., Kitazume, H., Kubota, M., Suemasu, T. and Akimoto, K. (2011). "Structural control of organic solar cells based on nonplanar metallophthalocyanine/C60 heterojunctions using organic buffer layers." *Org. Electron.*, 12 (6), 966–973.

---

Saleh, A.M., Gould, R.D. and Hassan, A.K. (1993). "Dependence of AC electrical parameters on frequency and temperature in zinc phthalocyanine thin films." *Phys. Status Solidi A*, 139 (2), 379–389.

Serbenta, A., Kozlov, O.V., Portale, G., Loosdrecht, P.H.M. van and Pshenichnikov, M.S. (2016). "Bulk heterojunction morphology of polymer:fullerene blends revealed by ultrafast spectroscopy." *Sci. Rep.*, 6 36236.

Sessolo, M. and Bolink, H.J. (2011). "Hybrid Organic–Inorganic Light-Emitting Diodes." *Adv. Mater.*, 23 (16), 1829–1845.

Shafai, T.S. and Anthopoulos, T.D. (2001). "Junction properties of nickel phthalocyanine thin film devices utilising indium injecting electrodes." *Thin Solid Films*, 398–399 361–367.

Shafai, T.S. and Gould, R.D. (1990). "Transport properties in lead phthalocyanine thin films for use in FET structures." *Int. J. Electron. Theor. Exp.*, 69 (1), 3–9.

Shafai, T.S. and Gould, R.D. (1992a). "Electrical characteristics of lead phthalocyanine thin films using aluminium Schottky barriers and gold ohmic contacts." *Int. J. Electron.*, 73 (5), 1043–1045.

Shafai, T.S. and Gould, R.D. (1992b). "Observations of Schottky and Poole-Frenkel emission in lead phthalocyanine thin films using aluminium injecting electrodes." *Int. J. Electron.*, 73 (2), 307–313.

Shah, M., Sayyad, M.H. and Karimov, K.S. (2011). "Electrical characterization of the organic semiconductor Ag/CuPc/Au Schottky diode." *J. Semicond.*, 32 (4), 044001.

Sharma, A., Kumar, P., Singh, B., Chaudhuri, S.R. and Ghosh, S. (2011). "Capacitance-voltage characteristics of organic Schottky diode with and without deep traps." *Appl. Phys. Lett.*, 99 (2), 023301.

---

Sharma, A., Watkins, S.E., Andersson, G. and Lewis, D.A. (2014). "Effect of Annealing Temperature of ZnO on the Energy Level Alignment in Inverted Organic Photovoltaics (OPVs)." *Energy Technol.*, 2 (5), 462–468.

Sharma, G.D. (1995a). "A.c. electrical properties of Au/CIAIPc/Au device." *J. Mater. Sci. Mater. Electron.*, 6 (3), 149–153.

Sharma, G.D. (1995b). "Electrical and photoelectrical properties of Schottky barrier devices using the chloro aluminium phthalocyanines." *Synth. Met.*, 74 (3), 227–234.

Sharma, G.D., Kumar, R., Sharma, S.K. and Roy, M.S. (2006). "Charge generation and photovoltaic properties of hybrid solar cells based on ZnO and copper phthalocyanines (CuPc)." *Sol. Energy Mater. Sol. Cells*, 90 (7), 933–943.

Sharma, G.D., Sangodkar, S.G. and Roy, M.S. (1996). "Influence of iodine on the electrical and photoelectrical properties of zinc phthalocyanine thin film devices." *Mater. Sci. Eng. B*, 41 (2), 222–227.

Signerski, R., Jarosz, G. and Kościelska, B. (2009). "On photovoltaic effect in hybrid heterojunction formed from palladium phthalocyanine and titanium dioxide layers." *J. Non-Cryst. Solids*, 355 (24), 1405–1407.

Signerski, R. and Kościelska, B. (2005). "Photovoltaic properties of a sandwich cell consisting of bromophosphorus phthalocyanine and titanium dioxide layers." *Opt. Mater.*, 27 (9), 1480–1483.

Singh, B. and Ghosh, S. (2013). "Zinc oxide and metal phthalocyanine based hybrid P-N junction diodes." *Appl. Phys. Lett.*, 103 (13), 133301.

Singh, B. and Ghosh, S. (2015). "Highly Conducting Gallium-Doped ZnO Thin Film as Transparent Schottky Contact for Organic- Semiconductor-Based Schottky Diodes." *J. Electron. Mater.*, 1–7.

---

Song, D., Zhu, F., Yu, B., Huang, L., Geng, Y. and Yan, D. (2008). "Tin (IV) phthalocyanine oxide: An air-stable semiconductor with high electron mobility." *Appl. Phys. Lett.*, 92 (14), 143303.

Spahr, H., Reinker, J., Bülow, T., Nanova, D., Johannes, H.-H. and Kowalsky, W. (2013). "Regimes of leakage current in ALD-processed Al<sub>2</sub>O<sub>3</sub> thin-film layers." *J. Phys. Appl. Phys.*, 46 (15), 155302.

Spanggaard, H. and Krebs, F.C. (2004). "A brief history of the development of organic and polymeric photovoltaics." *Sol. Energy Mater. Sol. Cells*, 83 (2), 125–146.

Stallinga, P. (2009). "Electrical characterization of organic electronic materials and devices (Chichester, U.K. : John Wiley & Sons,).

Suman, C.K., Yang, J. and Lee, C. (2010). "Temperature dependent transport properties in molybdenum oxide doped  $\alpha$ -NPD." *Mater. Sci. Eng. B*, 166 (2), 147–151.

Suman, C.K., Yun, J., Kim, S., Lee, S.-D. and Lee, C. (2009). "AC impedance spectroscopic studies of transport properties in metal oxide doped  $\alpha$ -NPD." *Curr. Appl. Phys.*, 9 (5), 978–984.

Sun, Y., Seo, J.H., Takacs, C.J., Seifert, J. and Heeger, A.J. (2011). "Inverted Polymer Solar Cells Integrated with a Low-Temperature-Annealed Sol-Gel-Derived ZnO Film as an Electron Transport Layer." *Adv. Mater.*, 23 (14), 1679–1683.

Sussman, A. (1967a). "Electrical properties of copper phthalocyanine thin films as influenced by the ambient." *J. Appl. Phys.*, 38 (7), 2748–2752.

Sussman, A. (1967b). "Space-Charge-Limited Currents in Copper Phthalocyanine Thin Films." *J. Appl. Phys.*, 38 (7), 2738–2748.

Sutarlie, L. and Yang, K.-L. (2008). "Colorimetric responses of transparent polymers doped with metal phthalocyanine for detecting vaporous amines." *Sens. Actuators B Chem.*, 134 (2), 1000–1004.

---

Tang, B.-T., Yu, Q.-X., Lee, H.-Y. and Lee, C.-T. (2001). "Ohmic performance of ZnO and ITO/ZnO contacted with n-type GaN layer." *Mater. Sci. Eng. B*, 82 (1), 259–261.

Tang, C.W. (1986). "Two-layer organic photovoltaic cell." *Appl. Phys. Lett.*, 48 (2), 183–185.

Thejo Kalyani, N. and Dhoble, S.J. (2015). "Novel materials for fabrication and encapsulation of OLEDs." *Renew. Sustain. Energy Rev.*, 44 319–347.

Tracey, S.M., Hodgson, S.N.B. and Ray, A.K. (1998). "Sol-Gel Derived TiO<sub>2</sub>/Lead Phthalocyanine Photovoltaic Cells." *J. Sol-Gel Sci. Technol.*, 13 (1–3), 219–222.

Tress (auth.), W. (2014). "Organic Solar Cells: Theory, Experiment, and Device Simulation (Springer International Publishing).

Tripathi, D.C., Tripathi, A.K. and Mohapatra, Y.N. (2011). "Mobility determination using frequency dependence of imaginary part of impedance (Im Z) for organic and polymeric thin films." *Appl. Phys. Lett.*, 98 (3), 033304.

Tsang, S.W., So, S.K. and Xu, J.B. (2006a). "Application of admittance spectroscopy to evaluate carrier mobility in organic charge transport materials." *J. Appl. Phys.*, 99 (1), 013706.

Tsang, S.W., Tse, S.C., Tong, K.L. and So, S.K. (2006b). "PEDOT:PSS polymeric conducting anode for admittance spectroscopy." *Org. Electron.*, 7 (6), 474–479.

Tsuzuki, T., Hirota, N., Noma, N. and Shirota, Y. (1996). "Photoelectrical conversion of pn heterojunction devices using thin films of titanyl phthalocyanine and a perylene pigment." *Thin Solid Films*, 273 (1–2), 177–180.

Tverdova, N.V., Girichev, G.V., Krasnov, A.V., Pimenov, O.A. and Koifman, O.I. (2013). "The molecular structure, bonding, and energetics of oxovanadium phthalocyanine: an experimental and computational study." *Struct. Chem.*, 24 (3), 883–890.

---

Wacławek, W. and Ząbkowska-Wacławek, M. (1987). "The influence of iodine on the electrical properties of lead phthalocyanine." *Thin Solid Films*, 146 (1), 1–6.

Wahab, F., Sayyad, M.H., Tahir, M., Khan, D.N., Aziz, F., Shahid, M., Munawar, M.A., Chaudry, J.A. and Khan, G. (2014). "Electrical characterization of cobalt phthalocyanine/n-Si heterojunction." *Synth. Met.*, 198 175–180.

Wang, H., Fukuda, T., Ishikawa, N. and Matsuo, Y. (2014a). "Solvent-dependent morphology of thermally converted copper phthalocyanine for solution-processed small molecule organic photovoltaic devices." *Org. Electron.*, 15 (1), 139–143.

Wang, H., Zhou, Y., Roy, V.A.L., Yan, D., Zhang, J. and Lee, C.-S. (2014b). "Polymorphism and electronic properties of vanadyl-phthalocyanine films." *Org. Electron.*, 15 (7), 1586–1591.

Wang, H., Zhu, F., Yang, J., Geng, Y. and Yan, D. (2007). "Weak Epitaxy Growth Affording High-Mobility Thin Films of Disk-Like Organic Semiconductors." *Adv. Mater.*, 19 (16), 2168–2171.

Wang, J.-C., Weng, W.-T., Tsai, M.-Y., Lee, M.-K., Horng, S.-F., Perng, T.-P., Kei, C.-C., Yu, C.-C. and Meng, H.-F. (2010). "Highly efficient flexible inverted organic solar cells using atomic layer deposited ZnO as electron selective layer." *J. Mater. Chem.*, 20 (5), 862–866.

Wang, T., Kafle, T.R., Kattel, B. and Chan, W.-L. (2017). "A Multidimensional View of Charge Transfer Excitons at Organic Donor–Acceptor Interfaces." *J. Am. Chem. Soc.*, 139 (11), 4098–4106.

Williams, G., Suttly, S., Klenkler, R. and Aziz, H. (2014). "Renewed interest in metal phthalocyanine donors for small molecule organic solar cells." *Sol. Energy Mater. Sol. Cells*, 124 217–226.

Wright, M. and Uddin, A. (2012). "Organic—inorganic hybrid solar cells: A comparative review." *Sol. Energy Mater. Sol. Cells*, 107 87–111.

---

Xia, A.D., Fu, S.J., Pan, H.B., Zhang, X.Y., Xu, Z., Liu, Q. and Yuan, R.K. (1995). "Characteristics of heterojunction diode of C60/chloroindium phthalocyanine." *Solid State Commun.*, 95 (10), 713–716.

Yamamoto, N., Tonomura, S. and Tsubomura, H. (1981). "Hydrogen sensitive Schottky barriers in metal-copper phthalocyanine junctions and their photovoltaic effect." *J. Appl. Phys.*, 52 (9), 5705–5709.

Yapi, A.S., Toumi, L., Lare, Y., Soto, G.M., Cattin, L., Toubal, K., Djafri, A., Morsli, M., Khelil, A., Valle, M.A.D. and Bernède, J.-C. (2010). "On the influence of the exciton-blocking layer on the organic multilayer cells properties." *Eur. Phys. J. Appl. Phys.*, 50 (3), 30403.

Yasuda, T. and Tsutsui, T. (2006). "n-Channel organic field-effect transistors based on boron-subphthalocyanine." *Mol. Cryst. Liq. Cryst.*, 462 (1), 3–9.

Yip, H.-L. and Jen, A.K.-Y. (2012). "Recent advances in solution-processed interfacial materials for efficient and stable polymer solar cells." *Energy Environ. Sci.*, 5 (3), 5994–6011.

Yonehara, H. and Pac, C. (1996). "Photoelectrical properties of double-layer organic solar cells using C60 and phthalocyanines." *Thin Solid Films*, 278 (1), 108–113.

Yoon, S.M., Lou, S.J., Loser, S., Smith, J., Chen, L.X., Facchetti, A. and Marks, T. (2012). "Fluorinated Copper Phthalocyanine Nanowires for Enhancing Interfacial Electron Transport in Organic Solar Cells." *Nano Lett.*, 12 (12), 6315–6321.

Yuan, Z. (2014a). "A photodiode with high rectification ratio and low turn-on voltage based on ZnO nanoparticles and SubPc planar heterojunction." *Phys. E Low-Dimens. Syst. Nanostructures*, 56 160–164.

Yuan, Z. (2014b). "A photodiode with high rectification ratio and low turn-on voltage based on ZnO nanoparticles and SubPc planar heterojunction." *Phys. E Low-Dimens. Syst. Nanostructures*, 56 (Supplement C), 160–164.

---

Yuan, Z., Fu, M. and Ren, Y. (2014). "Optoelectronic Properties of ZnO Nanoparticle/Pentacene Heterojunction Photodiode." *J. Electron. Mater.*, 43 (9), 3270–3275.

Yuan, Z., Yu, J., Wang, N. and Jiang, Y. (2012). "A hybrid photodiode with planar heterojunction structure consisting of ZnO nanoparticles and CuPc thin film." *Curr. Appl. Phys.*, 12 (5), 1278–1282.

Zeyada, H.M., El-Nahass, M.M., El-Menyawy, E.M. and El-Sawah, A.S. (2015). "Electrical and photovoltaic characteristics of indium phthalocyanine chloride/p-Si solar cell." *Synth. Met.*, 207 46–53.

Zeyada, H.M., Makhlof, M.M., El-Shabaan, M.M. and Zeyada, M.H. (2016). "Electrical transport mechanisms and photovoltaic characteristics of Au/neutral red/p-Si/Al heterojunction solar cell." *Microelectron. Eng.*, 157 35–41.

Zhang, S., Li, L. and Kumar, A. (2008). "Materials Characterization Techniques (CRC Press).

Zhao, D.W., Sun, X.W., Jiang, C.Y., Kyaw, A.K.K., Lo, G.Q. and Kwong, D.L. (2008). "Efficient tandem organic solar cells with an Al/MoO<sub>3</sub> intermediate layer." *Appl. Phys. Lett.*, 93 (8), 83305.

Zhu, L., Tang, H., Harima, Y., Kunugi, Y., Yamashita, K., Ohshita, J. and Kunai, A. (2001). "A relationship between driving voltage and the highest occupied molecular orbital level of hole-transporting metallophthalocyanine layer for organic electroluminescence devices." *Thin Solid Films*, 396 (1), 214–219.

Ziolo, R.F., Griffiths, C.H. and Troup, J.M. (1980). "Crystal structure of vanadyl phthalocyanine, phase II." *J. Chem. Soc. Dalton Trans.*, 0 (11), 2300–2302.



---

## LIST OF PUBLICATIONS

### Papers Published in International Journals

1. **M. Raveendra Kiran**, Hidayath Ulla, M. N. Satyanarayan and G. Umesh, "Optoelectronic properties of hybrid diodes based on Vanadyl phthalocyanine and Zinc oxide thin films," **Superlattices and Microstructures** (2017)112,654-664.
2. **M. Raveendra Kiran**, Hidayath Ulla, M.N. Satyanarayan, G. Umesh, "Effect of deposition rate on the charge transport in Vanadyl-phthalocyanine thin films " **Synthetic Metals** (2017)224, 63-71.
3. **M. Raveendra Kiran**, Hidayath Ulla, Krishnamanohara, M. N. Satyanarayan, G. Umesh. "Investigation of charge transport in Vanadyl-phthalocyanine with molybdenum trioxide as a buffer layer: Impedance spectroscopic analysis " **Synthetic Metals** (2015) 210, 208-213.
4. **M. Raveendra Kiran**, Hidayath Ulla, M. N. Satyanarayan and G. Umesh, "Optoelectronic properties of hybrid diodes based on Vanadyl phthalocyanine and vertically aligned Zinc oxide Nanorods (under preparation).

### International Conference Proceedings

1. **M. Raveendra Kiran**, Hidayath Ulla, Jean M. Fernandes, M.N. Satyanarayan, G. Umesh, " Electrical Characterization of Hybrid Hetero Interface using n-ZnO and p-CuPc." **Materials Today: Proceedings** (2015) 2, 1230 – 1233.

### Papers Presented at Conferences

1. M. Raveendra Kiran, Hidayath Ulla, MN Satyanarayan, G. Umesh, "Studies on Charge Transport of Metal (Copper and Vanadium Oxide) Phthalocyanines Using Imaginary Impedance (-Im Z) Measurements" International photovoltaic solar energy conference (IPSEC-2015) Department of Physics, Savitribai Phule Pune University, Pune, India, June 1-2, 2015.
2. M. Raveendra Kiran, Hidayath Ulla, MN Satyanarayan, G. Umesh. "Investigation of Impedance Spectroscopy of Inorganic/Organic Hybrid p-n Junction Based on ZnO and CuPc". 3rd National conference on condensed

---

matter physics and applications (CMPA 2015), Manipal Institute of Technology, Manipal, India, March 27-28, 2015.

3. M. Raveendra Kiran, Hidayath Ulla, Jean Maria Fernandes, MN Satyanarayan, G. Umesh “*Electrical Characterization of Hybrid Hetero Interface using n-ZnO and p-CuPc*.” 4th International Conference on Materials Processing and Characterization (ICMPC), GRIET, Hyderabad, India, 14-15, March 2015.

## Brief Profile

---

### **MANEPALLI RAVEENDRA KIRAN**

Research Scholar	Email : <a href="mailto:kiran.phy85@gmail.com">kiran.phy85@gmail.com</a>
PH # 104, Optoelectronics Laboratory(OEL)	Mobile:+91 9071987538
Department of Physics	Date of Birth : 15 June 1985
National Institute of Technology Karnataka	Nationality : Indian
Surathkal	Religion : Hindu
Mangalore-575025, India.	Languages: English, Telugu

### **QUALIFICATION**

- **Ph.D. in Physics (Thesis submitted, December 2017)** , National Institute of Technology Karnataka, Surathkal,
- **M.Sc. (Physics)** Andhra University, Visakhapatnam (2007)
- **B.Sc. (Mathematics, Physics, Chemistry)** Andhra University, Visakhapatnam (2005)

### **PUBLICATIONS IN PEER-REVIEWED JOURNALS**

1. M. Raveendra Kiran, Hidayath Ulla, M. N. Satyanarayan and G. Umesh, "Optoelectronic properties of hybrid diodes based on Vanadyl phthalocyanine and Zinc oxide thin films." Superlattices and Microstructures (2017)112,654-664
2. Hidayath Ulla, M. Raveendra Kiran, B. Garudachari, T.N. Ahipa, Kartick Tarafder, Airody Vasudeva Adhikari, G. Umesh and M.N. Satyanarayan, "Blue-emitting 1,8-naphthalimides with electron transport properties for organic light emitting diode applications." Journal of Molecular Structure (2017)1143, 344-354
3. M. Raveendra Kiran, Hidayath Ulla, M.N. Satyanarayan, G. Umesh, "Effect of deposition rate on the charge transport in Vanadyl-phthalocyanine thin films." Synthetic Metals, 224 (2017), 63-71.
4. M. Raveendra Kiran, Hidayath Ulla, MN Satyanarayan, G. Umesh. "Investigation of charge transport in Vanadyl-phthalocyanine with molybdenum trioxide as a buffer layer: Impedance spectroscopic analysis."

## Brief Profile

---

Synthetic Metals 210 (2015), 208-213

5. Swetha Chidirala, Hidayath Ulla, Anusha Valaboju, M. Raveendra Kiran, Maneesha Esther Mohanty, M. Nagarajan Satyanarayan, Govindarao Umesh, Kotamarthi Bhanuprakash, Vaidya Jayathirtha Rao, “Pyrene-Oxadiazoles for Organic Light Emitting Diodes: Triplet to Singlet Energy Transfer and Role of Hole-injection/Hole-blocking Materials.” Journal of organic chemistry 81 (2016), pp 603–614.
6. Jean Maria Fernandes, M. Raveendra Kiran, Hidayath Ulla, M.N. Satyanarayan, G. Umesh, “Investigation of hole transport in  $\alpha$ -NPD using impedance spectroscopy with F4TCNQ as a hole-injection layer.” Superlattices and Microstructures, 83 (2015), 766–775.
7. Hidayath Ulla, M. Raveendra Kiran, B Garudachari, MN Satyanarayan, G Umesh, AM Isloor, “Blue-emitting halogen–phenoxy substituted 1, 8-naphthalimides for potential organic light emitting diode applications.” Optical materials 37 (2014) 311-321.
8. Jean Maria Fernandes, M. Raveendra Kiran, Hidayath Ulla, M.N. Satyanarayan, G. Umesh, “Investigation of hole injection in  $\alpha$ -NPD using impedance spectroscopy with F4TCNQ as hole-injection layer: Initial studies.” Superlattices and Microstructures 74 (2014), 385-393.
9. A. Subrahmanyam, A. Rajakumar, Md. Rakibuddin, T. Paul Ramesh, M. Raveendra Kiran, D. Shankaria and K. Chandrasekhar, “Efficacy of titanium doped-indium tin oxide (Ti/TiO<sub>2</sub>-ITO) films in rapid oxygen generation under photocatalysis and their suitability for bio-medical application.” Physical chemistry chemical physics 16(2014), 24790-24799.
10. M. Raveendra Kiran, Hidayath Ulla, Jean M. Fernandes, M.N. Satyanarayan, G. Umesh, “Electrical Characterization of Hybrid Hetero Interface using n-ZnO and p-CuPc.” Materials Today: Proceedings 2 (2015) 1230 – 1233.

## Brief Profile

---

### **RESEARCH EXPERIENCE**

**Project Officer** -Project Title: Preparation and characterization of ITO, TiO<sub>2</sub> thin films for Photocatalysis and biomedical applications (March 2010 to July 2012)

**Principle investigator:** Prof. A. Subrahmanyam

**Place:** Semiconductor Laboratory, Indian Institute of Technology Madras, India.

### **TEACHING EXPERIENCE**

**Teaching Assistant**-National Institute of Technology Karnataka, Surathkal

- Engineering physics laboratory course for B.Tech students (August 2012-July 2017)
- Physics laboratory courses for M.Sc. Students (August 2012-July 2017)
- Project guiding for M.Sc. Students (August 2013-July 2017)

**Assistant professor** - Prasiddha College of Engineering and Technology, Amalapuram (July 2009-February 2010)

- Engineering physics theory and Laboratory experiments for B.Tech students

**Lecturer**-The Amalapuram Junior and Degree College, Amalapuram

- Theory Course and Laboratory experiments for B.Sc and Pre- University students

### **RESEARCH SKILLS**

- Metal and oxide thin film deposition by Thermal evaporation unit (PVD), Sol-gel spin coating and DC magnetron sputtering techniques
- Spectrophotometry (UV-Vis)
- Photoluminescence spectroscopy
- Structural characterization (XRD, AFM and FESEM)
- Electrical measurements (Hall effect, Photoconductivity and Impedance spectroscopy)
- Photocatalysis and photovoltaic characterization